AD-A050 648 GENERAL MOTORS CORP INDIANAPOLIS IND DETROIT DIESEL --ETC F/G 21/5
THE EFFECT OF ROTOR-STATOR AXIAL SPACING ON THE TIME-VARIANT AE--ETC(U)
DEC 77 S FLEETER, R L JAY, W A BENNETT F49620-77-C-0024
UNCLASSIFIED DDA-EDR-9379 AFOSR-TR-78-0165 NL

1 OF 2
AD A050648

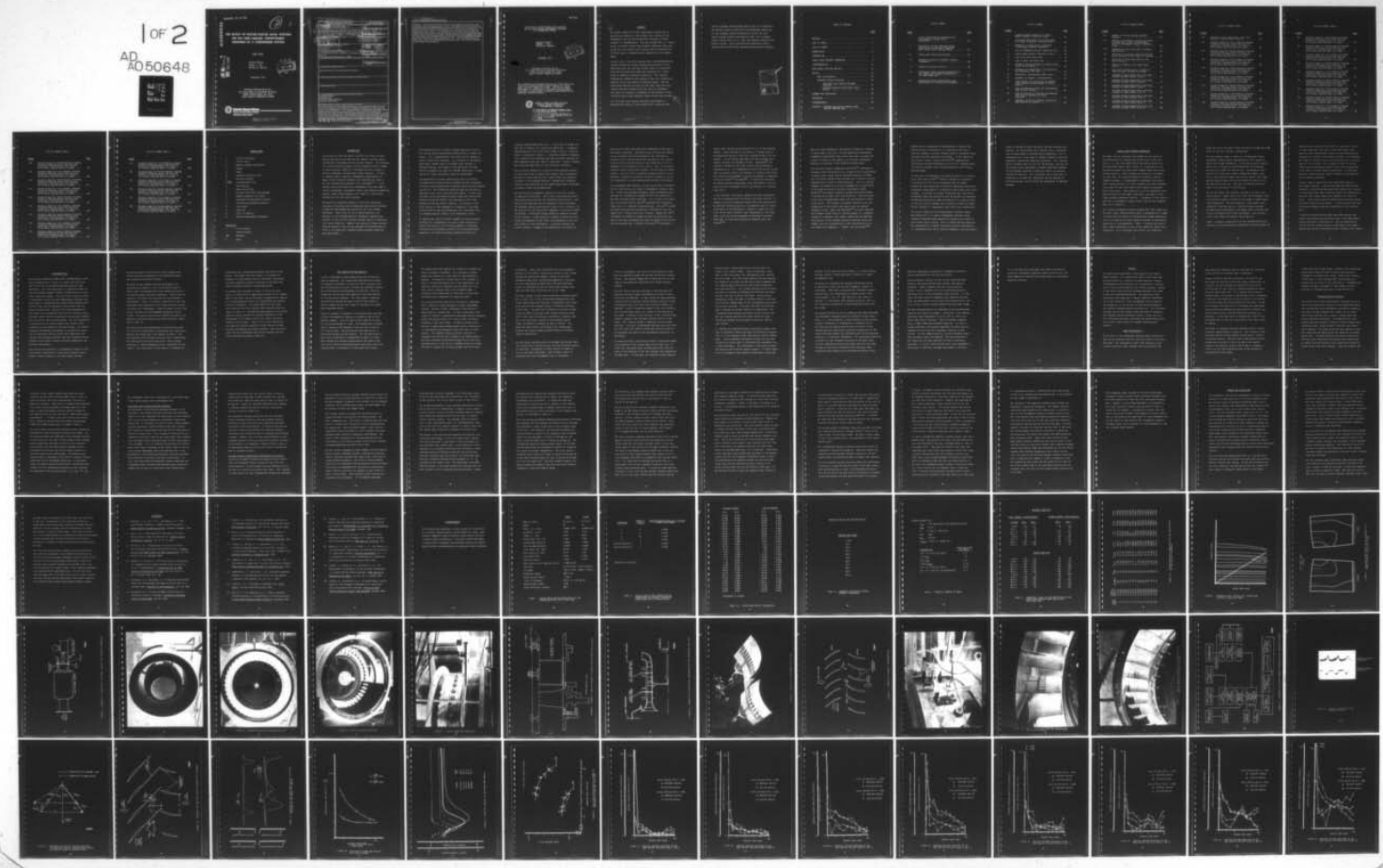

(2)

THE EFFECT OF ROTOR-STATOR AXIAL SPACING ON THE TIME-VARIANT AERODYNAMIC RESPONSE OF A COMPRESSOR STATOR

EDR 9379

Sanford Fleeter
Robert L. Jay
William A. Bennett

December 1977

Research Sponsored by the
Air Force Office of Scientific Research
(AFSC) United States Air Force
under Contract F49620-77-C-0024

Detroit Diesel Allison
Division of General Motors Corporation
Indianapolis, Indiana 46206

UNCLASSIFIED

SECURITY CLASSIFICATION OF THIS PAGE (When Data Entered)

REPORT DOCUMENTATION PAGE

READ INSTRUCTIONS BEFORE COMPLETING FORM

1. REPORT NUMBER: AFOSR-TR-78-0165
2. GOVT ACCESSION NO.
3. RECIPIENT'S CATALOG NUMBER

4. TITLE (and Subtitle): THE EFFECT OF ROTOR-STATOR AXIAL SPACING ON THE TIME-VARIANT AERODYNAMIC RESPONSE OF A COMPRESSOR STATOR.

5. TYPE OF REPORT & PERIOD COVERED: FINAL rept. 1 Nov 76 - 31 Oct 77

6. PERFORMING ORG. REPORT NUMBER: DDA-EDR-9379

7. AUTHOR(s): SANFORD FLEETER, ROBERT L. JAY, WILLIAM A. BENNETT

8. CONTRACT OR GRANT NUMBER(s): F49620-77-C-0024

9. PERFORMING ORGANIZATION NAME AND ADDRESS:
DETROIT DIESEL ALLISON
PO BOX 894
INDIANAPOLIS, IN 46206

10. PROGRAM ELEMENT, PROJECT, TASK AREA & WORK UNIT NUMBERS: 2307/A4, 61102F, A4

11. CONTROLLING OFFICE NAME AND ADDRESS:
AIR FORCE OFFICE OF SCIENTIFIC RESEARCH/NA
BLDG 410
BOLLING AIR FORCE BASE, D C 20332

12. REPORT DATE: Dec 77
13. NUMBER OF PAGES: 158 (161 p.)

14. MONITORING AGENCY NAME & ADDRESS (if different from Controlling Office)

15. SECURITY CLASS. (of this report): UNCLASSIFIED

15a. DECLASSIFICATION/DOWNGRADING SCHEDULE

16. DISTRIBUTION STATEMENT (of this Report)

Approved for public release; distribution unlimited.

17. DISTRIBUTION STATEMENT (of the abstract entered in Block 20, if different from Report)

18. SUPPLEMENTARY NOTES

19. KEY WORDS (Continue on reverse side if necessary and identify by block number)
TURBOMACHINERY
COMPRESSORS
UNSTEADY AERODYNAMICS
FORCED VIBRATIONS

20. ABSTRACT (Continue on reverse side if necessary and identify by block number)

The overall objective of this experimental program was to quantify the effects of rotor-stator axial spacing on the fundamental time-variant aerodynamics relevant to forced response in turbomachinery. This was accomplished in a large-scale, low-speed, single-stage research compressor which permitted two rotor-stator axial spacing ratios representative of those found in advanced design compressors to be investigated. At each value of the axial spacing ratio, the aerodynamically induced fluctuating surface pressure distributions on the downstream vane row, with the primary source of excitation being the upstream rotor wakes, were measured over a wide range of compressor operating

DD FORM 1 JAN 73 1473 EDITION OF 1 NOV 65 IS OBSOLETE

UNCLASSIFIED 019200

SECURITY CLASSIFICATION OF THIS PAGE (When Data Entered)

conditions. The velocity fluctuations created by the passage of the rotor blades were measured in the non-rotating coordinate system. Data obtained described the variation of the rotor wake with both loading and axial distance from the rotor as parameters. This data also served as a reference in the analysis of the resulting time-variant pressure signals on the vane surfaces. The individual vane surface data were investigated to determine the effect of rotor-stator axial spacing on the overall unsteady pressure magnitude as well as to determine the dynamic pressure coefficient and aerodynamic phase lag for the unsteady pressure differential across the vane. These unsteady pressure differential data, with incidence angles ranging from $+\frac{1}{2}^{o}$ to $-12\frac{1}{2}^{o}$ and reduced frequency from 6.795 to 20.20, were correlated with predictions from a state-of-the-art flat plate cascade transverse gust analysis.

EDR 9379

THE EFFECT OF ROTOR-STATOR AXIAL SPACING ON THE TIME-VARIANT AERODYNAMIC RESPONSE OF A COMPRESSOR STATOR

SANFORD FLEETER
ROBERT L. JAY
WILLIAM A. BENNETT

DECEMBER 1977

Research Sponsored by the
Air Force Office of Scientific Research
(AFSC) United States Air Force
Under Contract F49620-77-C-0024

DETROIT DIESEL ALLISON DIVISION
GENERAL MOTORW CORPORATION
INDIANAPOLIS, INDIANA

ABSTRACT

The overall objective of this experimental program was to quantify the effects of rotor-stator axial spacing on the fundamental time-variant aerodynamics relevant to forced response in turbomachinery. This was accomplished in a large-scale, low-speed, single-stage research compressor which permitted two rotor-stator axial spacing ratios representative of those found in advanced design compressors to be investigated.

At each value of the axial spacing ratio, the aerodynamically induced fluctuating surface pressure distributions on the downstream vane row, with the primary source of excitation being the upstream rotor wakes, were measured over a wide range of compressor operating conditions. The velocity fluctuations created by the passage of the rotor blades were measured in the non-rotating coordinate system. Data obtained described the variation of the rotor wake with both loading and axial distance from the rotor as parameters. This data also served as a reference in the analysis of the resulting time-variant pressure signals on the vane surfaces.

The individual vane surface data were investigated to determine the effect of rotor-stator axial spacing on the

overall unsteady pressure magnitude as well as to determine the dynamic pressure coefficient and aerodynamic phase lag for the unsteady pressure differential across the vane. These unsteady pressure differential data, with incidence angles ranging from + $\frac{1}{2}°$ to -$12\frac{1}{2}°$ and reduced frequency from 6.795 to 20.20, were correlated with predictions from a state-of-the-art flat plate cascade transverse gust analysis.

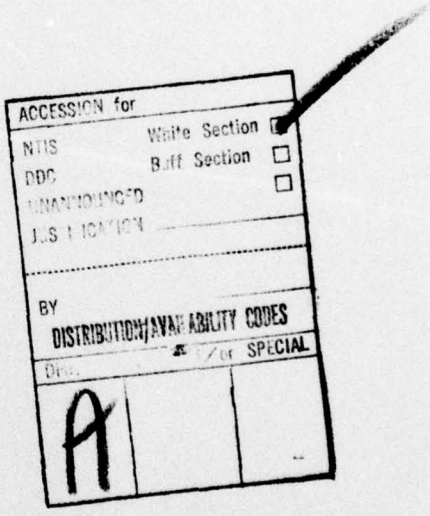

TABLE OF CONTENTS

LIST OF TABLES

LIST OF FIGURES

LIST OF FIGURES (CONT.)

LIST OF FIGURES (CONT.)

LIST OF FIGURES (CONT.)

LIST OF FIGURES (CONT.)

LIST OF FIGURES (CONT.)

NOMENCLATURE

b	Airfoil semi-chord
C	Airfoil chord
C_p	Dynamic pressure coefficient
L	Length
R	Radius
R_c	Compressor pressure ratio
V	Absolute velocity
$W\sqrt{\theta}/\delta$	Corrected mass flow
S	Vane spacing
T	Blade pass period
X	Distance from rotor trailing edge
k	Reduced frequency ($k = \omega b/V$)
u	Longitudinal perturbation velocity
v	Transverse perturbation velocity
β	Inlet angle
ϕ	Phase lag
ρ	Inlet air density
ω	Blade passing angular frequency

Subscripts

1	First harmonic
2	Second harmonic
ABS	Absolute
R	Rotor

INTRODUCTION

The failure of rotor and stator airfoils as a result of aerodynamic excitations has been and yet remains a serious design consideration throughout the gas turbine industry. The discovery of a forced response problem, and the subsequent need to affect a viable solution, results in increased unit cost, delays in delivery schedules, and decreased flight readiness. As early as 1955 the need to develop a fundamental understanding of these "forced response" problems was recognized and noted in the open literature by Whitmore, Lull, and Adams[1]. In the ensuing time period significant advancements have been made in solution techniques, aerodynamic theory, and computing capability. However, today forced response still ranks as a significant problem area for gas turbine engines.

The ability to accurately predict a priori the structural resonances of turbine engine blading has been greatly enhanced through the development and application of finite element techniques. Thus, prior to rig or engine operation, the designer is now provided detailed information regarding the location of the critical resonant response regions of operation for a given blade row. However, the severity of these resonant response regions to the various upstream or downstream excitations is not known until complete engine envelope conditions have been tested.

The identification of a highly stressed resonance of an airfoil during testing necessitates modifications to reduce the stress. For a component test, the stress can be reduced by simply avoiding the resonance. For an engine in the development phase, schemes such as increased axial spacing, redesigned blading, and changes in the excitation are used. Similar procedures are used for problems identified in flight engines as longer operational times are established.

One method which has been successfully used to alleviate aerodynamically forced response problems involves increasing the axial spacing between the excitation source and the responding airfoil. This method has generally been applied when an upstream airfoil row is the excitation source. In this case the wakes can be the mechanism which create the time-variant pressures along the chord of the downstream airfoil row, thereby driving the airfoil response. An increase in the axial spacing is then regarded as a reduction in the wake velocity deficit and, correspondingly, as a decreased level of unsteady pressure loading on the responding airfoil.

To identify the type of analysis needed for forced response problems and, consequently, the type of data necessary to assess that analysis, the following example is presented. Following the performance evaluation of an advanced design compressor, the routine teardown inspection of the unit

revealed cracked blades and vanes. In four rows of blades and two rows of stators, tip cracks were identified. A frequency-speed diagram for one of the rotor blades in which a crack was noted is presented in Figure 1. Along the excitation frequency line (created by the upstream vane row) the blade resonance at which maximum stress was noted is identified. Figure 2 presents the calculated mode shape for the particular resonance.

Thus, from this example of a typical forced response problem, it can be seen that an appropriate analysis and, consequently the data to assess that analysis, must reflect the chordwise variation in the unsteady pressure. Without this chordwise variation, the excitation of the complex mode shape illustrated in Figure 2 could not be determined.

The time-variant aerodynamic response on an airfoil surface is comprised of two parts. One is due to the upstream disturbance being swept past the non-responding fixed airfoils. The second arises when the airfoil responds to this disturbance. The unsteady pressure distribution on the airfoil surfaces, i.e. the driving force for the airfoil response, is the sum of these two effects. Analytically these effects are modeled by means of two analyses. A gust analysis is used to predict the time-variant aerodynamics of the fixed, non-responding airfoils to each harmonic of the disturbance. An analysis wherein the airfoil cascade is assumed to be harmonically oscillating is

then used to predict the additional aerodynamic effect due to the blades responding. Superpositioning of these two effects can be performed only with knowledge of the amplitude of response of the blading because the magnitude of the pressure field resulting from the motion of the responding airfoil is dependent on the amplitude of the motion. Thus, an iterative solution containing the gust analysis, the oscillating airfoil analysis, and the airfoil structural dynamics analysis as key elements is necessary to predict the total response of an airfoil subjected to an upstream generated periodic disturbance.

The aerodynamic gust analysis, as well as the case of harmonic airfoil oscillations, are areas of fundamental research interest. Linearized unsteady aerodynamic small perturbation gust analyses for isolated and cascaded airfoils are appearing in the open literature with regularity. For a single, zero thickness, flat plate airfoil, Sears[2] predicted the fluctuating forces due to a sinusoidal transverse gust. Horlock[3] treated the generalized gust by considering a longitudinal gust and combining his results with those of Sears. Naumann and Yeh[4] considered the effects of camber by partially accounting for some of the coupling between the angle of attack of the airfoil and the unsteady flow. Goldstein and Atassi[5] developed a

second order analysis which accounts for all of the coupling effects. These analyses are currently of limited value to turbomachinery design in that only isolated airfoils are considered. Of more direct application are the unsteady aerodynamic analyses for cascaded airfoils. Whitehead[6] considered a cascade of flat plate airfoils moving through a transverse gust in an incompressible flow field as well as the case of harmonic airfoil oscillations in a uniform flow field. This analysis was extended to include the effects of compressibility by Fleeter[7] and Smith[8]. It should be noted that the above analyses by Whitehead, Smith and Fleeter, also consider the case of harmonic airfoil oscillations in a uniform flow field.

In the transonic flow regime, emphasis has been placed upon the case of harmonically oscillating flat plate airfoils, although it should be noted that these flat plate analyses can be modified relatively easily to include the case of a transverse gust, as per Reference 9. Recently a number of solutions to the basic inviscid, small perturbation, flat plate model involving various mathematical techniques have been developed, as noted and discussed by Chadwick, Bell and Platzer[10].

There are many mathematical and physical assumptions inherent in these models, yet only a limited quantity of appropriate fundamental experimental data exists with which to assess the range of validity of the models or to indicate refinements necessary to develop a valid predictive design model.

For the case of gusts, Commerford and Carta[11] simulated an unsteady inlet flow direction on a single airfoil by generating a Karman vortex street from an upstream transverse cylinder. The flow field created by the cylinder has a vertical velocity component which varied in both directions. This is a serious drawback for extension to airfoil cascades as it would result in the velocity direction varying from blade to blade. Ostdiek[12] developed a subsonic cascade wind tunnel capable of generating variable inlet flow direction. The wind tunnel inlet, which included guide vanes, was oscillated by a motor driven crank. This system is currently limited to very low frequencies of oscillation and, hence, very low reduced frequency values. Bruce and Henderson[13] directly measured the unsteady normal force and pitching moment on a chordwise element of a subsonic rotor blade, rather than the detailed distribution of the unsteady pressure difference across the blades, due to a circumferential inlet flow distortion in a low speed axial compressor. Fleeter, Jay and Bennett[14]

determined the incompressible aerodynamically induced fluctuating pressure distribution in a stationary vane row of realistic geometry, with the primary source of excitation being the wakes from the upstream rotor blades. In the supersonic flow regime, Fleeter, Novick and Riffel[9], measured the fluctuating pressure distribution on an airfoil cascade resulting from an unsteady inlet flow generated by an oscillating upstream wedge.

For the case of harmonically oscillating airfoils in a uniform inlet flow field, Carta[15] tested a cascade of torsionally oscillating airfoils at low frequencies and low speeds. Fleeter has been extensively involved in obtaining time-variant aerodynamic measurements in harmonically oscillating rectilinear cascades. References 16 through 18 describe the time-variant aerodynamic data and correlation with the analysis of Reference 19 obtained from torsion mode oscillations of a single airfoil, a classical airfoil cascade, and a multiple circular arc (MCA) airfoil cascade in a supersonic inlet flow field, respectively.

The overall objective of the experimental research program described herein is to obtain fundamental unsteady forced response aerodynamic data necessary to quantify the effect of rotor-stator axial spacing. This is accomplished by measuring the aerodynamically induced fluctuating pressure distribution in a downstream vane row of realistic geometry, with the primary

source of excitation being the wakes from the upstream rotor blading. Two rotor-stator axial spacing ratios, representative of those found in advanced design compressors, are investigated over a wide range of reduced frequency values and compressor steady-state operating conditions. This research effort furnishes data not only for the designer, but also for the analyst whose requirements include a detailed breakdown of the unsteady pressures on both the suction and pressure surfaces of the vane. This individual vane surface data is necessary to validate the assumptions and the adequacy of existing analyses, and to direct the development of advanced analyses.

SINGLE-STAGE RESEARCH COMPRESSOR

The wakes from the upstream rotor blades are the source of the aerodynamically induced time-variant vane surface pressures, i.e., the rotor wakes define the forcing function to the downstream stator vanes. Hence, it is desirable to experimentally model the significant features which define this forcing function. These include the variation of incidence, the wave form, the velocity (pressure) variation, and the reduced frequency. To meaningfully investigate rotor-stator axial spacing effects, it is also necessary to have representative values for the rotor-stator axial spacing to upstream axial chord ratio. These features can all be simulated in the Detroit Diesel Allison (DDA) large-scale, low-speed, single-stage research compressor facility. A schematic of the overall facility is presented in Figure 3 and a view of the assembled test rig in Figure 4.

This research compressor features blading (42 rotor blades and 40 stator vanes, NACA 65 Series) that is aerodynamically loaded to levels that are typical of advanced multi-stage compressors and is also physically large enough to provide for substantial quantities of instrumentation. Table I presents the airfoil mean section properties as well as the compressor design point conditions. As is indicated, the airfoils are relatively

large; the rotor and stator chords are equal to 4.589 and 5.089 inches (11.66 and 12.93 cm), respectively.

The rotor blades, shown in Figure 5, are designed to have aerodynamic loading levels representative of aft stages of modern multi-stage compressors. At the design point, approximately 27° of turning is accomplished near the blade hub, diminishing to about 13° near the tip. The geometric characteristics of the rotor blades include high camber, with fairly large deviation angle near the hub region, and a maximum thickness-to-chord ratio which varies from nearly 7% at the hub to 4% at the tip. The rotor solidity varies from about 1.6 at the hub to 1.3 at the tip.

The 40 vane stator row, Figure 6, results in an axial exit flow direction. Again, the airfoil loss and aerodynamic loading levels are typical of those of aft stages of modern multi-stage compressors. The vane features a large camber angle variation in the hub region, a radially constant maximum thickness-chord distribution, and design point incidence that varies from about zero to minus one degree. Vane solidity varies from 1.68 at the hub to 1.35 at the tip.

Table II presents a description of four advanced design compressors in which excitations created by an upstream blade row

caused serious concern for the life of a particular airfoil. For each compressor, the ratio of the rotor-stator axial spacing to the upstream axial chord has been determined and averaged with respect to the number of stages. As indicated, the range of interest for this axial spacing ratio is on the order of 0.15 to 0.49. Also included in Table II are the nominal and the decreased value for this ratio investigated in the above described research compressor. As indicated, these two values span the range of interest of advanced compressor design experience.

Figure 7 shows a view of the rotor and stator spacing in the nominal position. Figure 8 indicates the modifications necessary to achieve the decreased rotor-stator axial spacing. A casing spacer was used to move the stator row forward such that the rotor-stator spacing was reduced to the desired value. A thin spacing shim was then used to precisely locate the rotor relative to the stator. A forward spacer was used to minimize leakage along the forward face of the rotating disk.

It should be noted that the above described research compressor and blading were previously used in the experimental program described in Reference 14. The rig configuration for the current program features a stationary inner endwall whereas the previous investigation had a rotating inner endwall.

INSTRUMENTATION

The research compressor steady-state instrumentation, indicated schematically in Figure 9, permits the inlet and exit flow fields to be defined and the compressor map determined. The inlet temperature is measured by means of four thermocouples equally spaced circumferentially in the large stagnation chamber. The rotor inlet velocity profile is determined from the pressure measurements obtained from three equally circumferentially spaced eleven-element total pressure rakes and the average of four hub and four tip static pressure taps. The exit flow field downstream of the stator row is determined from six total pressure rakes, uniformly spaced across an equivalent vane passage, together with hub and tip static pressure taps. The exit temperature is measured with an eleven element rake located circumferentially at the center of the vane passage. The overall compressor aerodynamic performance is evaluated by examining the stagnation tank and stator exit temperature and pressure measurements, with the flow rate computed from the stagnation tank static pressure and total temperature and pressure measurements.

The time-variant quantities of fundamental interest in this experimental investigation include the fluctuating aerodynamic forcing function — the rotor wakes, and the

resulting chordwise distributions of the complex time-variant pressure distribution on the downstream stator vane pressure and suction surfaces.

The blade surface dynamic pressure measurements are accomplished by means of a pair of the NACA Series 65 stator vanes instrumented with flush mounted Kulite thin-line design dynamic pressure transducers. These vanes are located in the stator row such that one flow passage is instrumented. Table III presents a tabulation of the vane coordinates describing the airfoil shape along the stream-line which was instrumented. Figure 10 shows a view of the airfoil surfaces with the embedded transducers clearly visible. The suction and pressure surface transducers are mounted at identical percent vane chord locations, identified in Table IV.

The time-variant wake measurements are obtained by means of a cross-wire probe which is calibrated and linearized to 200 feet per second and $\pm$ 25° angular variation. The mean absolute exit flow angle from the rotor is determined by rotating the cross-wire probe until a zero voltage difference is obtained between the two linearized hot-wire signals. This mean angle is then used as a reference for

calculating the instantaneous absolute and relative flow angles. The output from each channel is corrected for tangential cooling effects and the individual fluctuating velocity components parallel and normal to the mean flow angle calculated from the corrected quantities.

As schematically depicted in Figure 11, the cross-wire probe is located axially immediately upstream of the leading edge of the stator row at mid-stator circumferential spacing in a passage adjacent to the one instrumented with dynamic pressure transducers. The probe holders for the cross-wire probe and also for a dynamic total pressure probe are shown in Figure 12. The machined pads mounted on the casing exterior surface provide for angular references for the measurement of air angles and also for radial and axial location of the probes. Figure 13 is a view looking aft and shows the relative locations of the cross-wire probe and the instrumented vane suction surface. The cross-wire probe and the instrumented vane suction surface with the rotor installed are seen in Figure 14.

DATA ACQUISITION AND ANALYSIS

In this investigation, both steady-state and time-variant data are acquired. The steady-state data define the points of compressor operation, in terms of overall pressure ratio and corrected mass flow rate, at which the unsteady velocity and surface pressure measurements are obtained. Both the steady and time-variant data acquisition are controlled by an on-line digital computer. The rotor speed is manually controlled by varying the power to the DC drive motor; a digital readout of the rotor speed is provided via a tachometer generated signal.

Figure 15 presents a schematic of the steady-state and time-variant instrumentation modules as related to the on-line digital computer. Only one mode of data acquisition operation can be performed at a time. The steady-state corrected data is output on the teletype at the rig site as well as on a line printer. The time-variant data acquisition is controlled through the CRT terminal. On-line monitoring of this time-variant data is accomplished by means of a dual beam storage oscilloscope synchronized to the speed of the rotor by an optically generated square wave pulse, while the unsteady data is presented on a high speed line printer.

The steady-state data acquisition follows the standard compressor evaluation procedure. At a selected corrected speed, the compressor is stabilized for approximately 5 minutes. Following this period, the on-line computer is used to initiate the acquisition of the temperatures and pressures necessary to generate the corrected mass flow rate, overall pressure ratio, and corrected speed. A scanning of the reduced data is then made to assure data uniformity and to ascertain the operating point.

The time-variant data acquisition and analysis technique used is based on a data averaging or signal enhancement concept. The key to such a technique is the ability to sample data at a preset time. For this investigation the signal of interest is generated at the blade passing frequency. Hence, the logical choice for a time or data initiation reference is the rotor shaft. An optical encoder which delivers a square wave voltage signal having a duration of 1.5 microseconds was mounted on the rotor shaft for this purpose. The computer analog-to-digital converter is triggered from the positive voltage at the leading edge of the pulse, thereby initiating the acquisition of the time unsteady data at a rate of up to 100,000 points per second. The data is sampled for N blade passages and over M rotor

revolutions. These rotor revolutions are not consecutive because a finite time is required to operate on the N blade passage data before the computer returns to the pulse acceptance mode which initiated the gathering of the data. For this experimental program, 80 to 100 digitized data points are obtained for each of three blade passages averaged over 400 rotor revolutions (N = 3, M = 400).

The basic concept of this time-variant data averaging technique is used in an on-line analog mode throughout the test. A dual beam storage oscilloscope is triggered by the encoder pulse and the time unsteady signals of interest preserved on the scope. For each rotor revolution one series of wave forms are added to the wave forms already existing on the face of the scope from previous revolutions, thereby yielding a time consistent overlay of the unsteady signals. Figure 16 presents an example of such an overlay. The upper and lower signals correspond to the leading edge pressure and suction surface dynamic pressure transducer signals respectively.

At each steady operating point an averaged time-variant data set, consisting of the two hot-wire and the 22 Kulite signals, are obtained. Photographs of these signals are made on-line as previously described. Each of these signals is digitized and Fourier decomposed into its harmonics.

In this investigation only the first two harmonics of the data are examined through the entirety of the data analysis process. The reduced frequencies of these data are in the range of turbomachinery experience with forced response problems.

From the Fourier analyses performed on the data both the magnitude and phase angles referenced to the data initiation pulse are obtained. To then relate the wake generated velocity profiles with the surface dynamic pressures on the instrumented vanes, the rotor exit velocity triangles are examined. Figure 17 shows the change in the rotor relative exit velocity which occurs as a result of the presence of the blade. A deficit in the velocity in this relative frame creates a change in the absolute velocity vector as indicated. This velocity change is measured via the crossed hot-wires. From this instantaneous absolute angle and velocity, the rotor exit relative angle and velocity as well as the magnitude and phase of the perturbation quantities are determined.

As noted previously, the hot-wire probe is positioned immediately upstream of the leading edge of the stator row. To relate the time based events as measured by this hot-wire probe to the pressures on the vane surfaces, the assumptions are made that: (1) the wakes are identical at the hot-wire

and the stator leading edge planes; (2) the wakes are fixed in the relative frame. Figure 18 presents a schematic of the rotor wakes, the instrumented vanes, and the hot-wire probe. The rotor blade spacing, the vane spacing, the length of the probe, and the axial spacing between the vane leading edge plane and the probe holder centerline are known quantities. At a steady operating point the hot-wire data is analyzed to determine the absolute flow angle and the rotor exit relative flow angle. Using the two assumptions noted, the wake is located relative to the hot-wires and the leading edges of the instrumented vane suction and pressure surfaces. From this, the times at which the wake is present at various locations is determined. The incremented times between occurrences at the hot-wire and the vane leading edge plane are then related to phase differences between the perturbation velocities and the vane surface.

To simplify the experiment-theory correlation process, the data is adjusted in phase such that the transverse perturbation is at zero degrees at the vane suction surface leading edge. From the geometry indicated in Figure 18, the time at which this would occur is calculated and transposed into a phase difference. This difference is then used to adjust the pressure data from the suction surface. A similar operation is performed on the pressure surface data so that the

surfaces of the vanes are time related; i.e., time relating the data results in data equivalent to that for a single instrumented vane.

Following this procedure the pressure differences across an equivalent single vane at each transducer location is calculated. These data, along with the individual surface pressure data, are normalized with respect to the inlet flow parameter: $(\rho \cdot V^2 \cdot \frac{v}{V})$ where ρ is the inlet air density, V is the stator inlet absolute velocity, and v is the transverse perturbation velocity measured by the cross-wire probe.

Any potential phase lag errors created by the above described time adjustment procedure would be constant for each transducer, i.e., the difference in phase between any two surface pressure transducers is unaffected by a potential error. The only area of concern would be the correlation of the reduced data with appropriate analytical predictions for the phase difference between the transverse gust and the measured response of a particular transducer. This experiment-prediction correlation of the chordwise variation of the phase angle could be compared by aligning the phase angle for the leading edge (2.47% chord) transducers with the phase angle predicted by the prediction to eliminate the effect of any

potential measurement inaccuracies, although it should be clearly noted that this was not done herein.

Several potential sources of error can be identified with regard to the above outlined data analysis and reduction procedure. Table V presents the most likely potential sources of error together with the corresponding possible resulting errors in the aerodynamic phase lag data. As indicated, the most critical parameters with regard to accurate phase lag measurements are the axial and circumferential locations of the cross-wire probe together with the probe length.

The data presented herein are subjected to the forementioned reduction and analysis procedure. Variations in the leading edge phase angle adjustment of up to $\pm$ 25° are felt to be within experimental accuracy. Table VI presents repeated data for 100% loaded and unloaded conditions. For the unloaded conditions, the pressure magnitude and phase data are compared for the first four transducer locations on each surface. For the loaded condition, various transducer magnitude and phase angles are compared. The data presented in this table have not been adjusted for time as previously described. As can be noted from the data, close agreement in phase angle is obtained, although some scatter is present.

It is felt that with reasonable care taken to establish a particular aerodynamic condition, phase variations of $\pm$ 15° would adequately represent the scatter band at a particular measuring location.

RESULTS

Two studies were undertaken in the course of this experimental program: (1) a qualitative study of the rotor wake velocity profile as a function of both compressor loading and downstream axial distance; (2) a quantitative investigation of the resulting time-variant surface pressures induced on the stator vanes by these upstream generated rotor wakes as they are convected downstream. The objective of the qualitative wake study was to obtain a physical understanding of the variations of this aerodynamic forcing function and thereby aid in the analysis of the resulting measured vane surface unsteady pressure distributions. The individual unsteady vane surface pressure data were used to determine the unsteady pressure difference across a single vane and this difference data then correlated with appropriate predictions from a state-of-the-art cascade transverse gust analysis.

Wake Investigation

The velocity is the fundamental quantity used to define the wake and was measured with the cross-wire probe as previously described. This measurement, made in the absolute or non-rotating reference frame, together with the absolute flow

angle and rotor speed were used to calculate the velocities in the relative or rotating frame of reference.

Figures 19 and 20 show the variations in the profile and the centerline velocity of the rotor wake, respectively, as a function of axial distance as measured from the rotor trailing edge for two values of loading (compression ratio) along the 100% speed line. At a constant axial distance from the rotor, an increase in the pressure ratio (a decrease in the mass flow rate) can be seen to result in an increase in both the width and velocity deficit of the wake. As the axial distance from the rotor is increased, the wake decays and the difference between the wake centerline velocity, U_c, (the minimum velocity) and the freestream velocity, U_e, decreases. At the high level of loading this trend is very pronounced, but is much less significant at the lower level of loading.

The effect of loading on the wake velocity profile is more completely demonstrated in Figure 21. The increase in both the width and the velocity deficit of the wake is vividly illustrated therein. The shift seen in the position of the minimum wake velocity is felt to be due to the angular change of the absolute velocity vector and to a change in location of the wake separation point on the surfaces of the generating rotor blades.

In this qualitative wake study, a dynamic (time-based) data acquisition system was used to acquire data generally relegated to a steady-state system. Rather than indexing a probe over a single passage width, the passages were rotated past the probe in this application. Dependent upon computer storage, any number of rotor blades could be assessed for averaged quantities in wake definition.

Unsteady Surface Pressures

The primary goal of this experimental investigation was to obtain the time-variant pressures on the downstream stator vane surfaces due to the aerodynamic excitation created by the wakes from the upstream rotor blades for two rotor-stator axial spacings over a range of steady-state compressor operating conditions. To accomplish this goal dynamic data were obtained at each of sixteen steady-state operating points: eight at each of the two rotor-stator axial spacings. The eight points for each spacing include four along both the 100% and the 70% compressor corrected speed lines. On-stand monitoring was used to assure that the data points obtained at the second axial spacing were at similar flow and pressure ratio conditions as those obtained at the first axial spacing. Figure 22 presents the

locations of the sixteen steady-state operating points along the 70% and 100% corrected speed lines in terms of overall pressure ratio and corrected mass flow rate for both axial spacings. Data points 1 through 8 were obtained at an axial spacing measured at mid-span equal to 0.719 inches (1.826 centimeters) and data points 9 through 16 were obtained with an axial spacing of 1.304 inches (3.312 centermeters). In terms of the ratio of the rotor-stator axial spacing to the upstream axial chord, these become 0.2374 and 0.4305 respectively, as noted in Table II.

The time-variant pressure data acquired in this program are presented for ease of discussion using three formats: (1) the measured dimensional magnitude of the unsteady pressure on each surface of the vane; (2) the dimensionless unsteady pressure magnitude and phase relation on the individual vane surfaces; (3) the dimensionless unsteady pressure differential across the vane and its phase relation to a transverse gust at the leading edge. The dimensionless pressure data is presented in the form of a dynamic pressure coefficient and an aerodynamic phase lag. As previously noted, the dynamic pressure coefficient is normalized with respect to inlet steady-state properties of the flow and the magnitude of the transverse gust: $C_p = p/\rho \cdot V^2 \cdot \frac{v}{V}$.

The aerodynamic phase lag is referenced to a transverse gust at the leading edge of the instrumented vane.

Individual Vane Surface Unsteady Pressures

The magnitudes of the measured unsteady pressures on the individual vane surfaces obtained along the 100% corrected speed line of the compressor for both values of axial spacing ratio at equivalent loadings are presented in Figures 23 through 26. As indicated, the overall level of the unsteady pressure magnitude on both surfaces of the vane increase with loading at approximately the same rate for each value of the axial spacing ratio. This increase is particularly pronounced for the small value of the rotor-stator axial spacing ratio (0.2374), being less significant for the large spacing ratio (0.4305). It is of interest to note that this difference in the rate of increase of the overall level of the surface pressure magnitudes with axial spacing ratio is not manifested in the resulting differential pressure magnitude data determined from these individual surface data. In fact, the dimensionless differential pressure magnitude and aerodynamic phase lag data show extremely good correlation between the two sets of rotor-stator axial spacing data.

Along the 70% speed line, the overall levels of the unsteady pressure magnitude on both surfaces also increase with loading at about the same rate, as seen in Figures 27 through 30. However no noticable difference with loading is apparent between the data for the two rotor-stator spacings along this speed line.

The fundamental measured quantities are the individual surface unsteady pressures, with the unsteady pressure differential data across the vane calculated from these individual surface measurements. As state-of-the-art cascade gust analyses only predict this unsteady pressure difference, this difference data is presented and discussed in depth. However, the first and second harmonics of the unsteady pressure on the vane pressure and suction surfaces are presented in the Appendix in tabular form to serve as an experimental baseline which can be used in the development of advanced analyses.

Unsteady Pressure Differential Data-Theory Correlation

Figures 31 through 62 present the dynamic pressure coefficient and aerodynamic phase lag data for the first and second harmonics of the unsteady pressure difference across the vane as a function of percent vane chord. Also included in these figures are the incompressible predictions obtained

from the state-of-the-art cascade transverse gust analysis of Reference 7 for the flow conditions as specified in Table VII. The key parameters included in this analysis are the reduced frequency, the interblade phase angle, the Mach number, and the cascade solidity and stagger angle.

This cascade analysis considers the two-dimensional, unsteady flow past a rectilinear flat plate cascade. The basic assumptions are: the fluid is a perfect gas; the flow field is irrotational; and the thin airfoil approximations are appropriate. The flow model assumes a basic uniform compressible flow field past an airfoil cascade, with small unsteady normal velocity fluctuations superimposed. The source of the fluctuations is located upstream with the oscillations in the velocity normal to the airfoil surfaces convected downstream with the uniform flow.

The thin airfoil assumptions taken together with the approximation of small unsteady, harmonic, compressible perturbations on the basic uniform flow leads to the linearized unsteady potential equation. The airfoil surface boundary conditions are determined from the upstream velocity fluctuations which are mathematically equivalent to prescribing normal relative velocities (or upwash) on each of the airfoils in the cascade. Three possible normal velocity perturbations are considered: (1) an imposed sinusoidal

transverse gust velocity imbedded in the freestream, appropriate for the experiment described herein; (2) translation of the airfoils; (3) torsion about an axis of the airfoil.

The chordwise dependence of the unsteady perturbation pressure across the airfoil is determined in integral form by obtaining the solution to the linearized unsteady potential equation with appropriate boundary conditions by means of complex Fourier transform theory. The unsteady pressure differential is then calculated by means of a straightforward inversion of the resulting integral equation in matrix form, with the leading edge singularity accounted for analytically.

The effects on the time-variant pressure distributions associated with the changes in the rotor-stator axial spacing ratio were discussed in some detail in the presentation of the individual vane surface data. As the objective of this subsection is to present and discuss the correlation of the unsteady pressure differential data with the predictions from the transverse gust and analysis, the difference data have been nondimensionalized by the parameter $\rho \cdot V^2 \cdot \frac{v}{V}$ evaluated at the stator inlet. The differences associated with the changes in the rotor-stator axial spacing ratio are thus inherent in this nondimensionalizing parameter. Hence,

the dimensionless time-variant pressure differential data for the two axial spacing ratios should, and indeed do, superimpose upon one another. It should be noted that significant variations with axial spacing in the nondimensionalizing parameter begin to become significant only at the highest pressure ratios attainable in the research compressor, as indicated in Table VII.

The first and second harmonic dimensionless pressure difference data together with the appropriate predictions are arranged and presented in terms of the value of the incidence angle on the vane. The relatively low incidence unsteady pressure differential results on the compressor 100% corrected speed line are presented in Figures 31 through 34, and those on the 70% speed line in Figures 35 through 46. The intermediate negative incidence angle results on the 100% and 70% speed lines are presented in Figures 47 through 52 and Figures 53 and 54, respectively. The large negative incidence angle results are found in Figures 55 through 58 on the 100% corrected speed line and in Figures 59 through 62 on the 70% speed line. The axial reduced frequency for these unsteady data based on the first and second harmonic frequencies range from 6.795 to 20.20.

The relatively low incidence angle dynamic pressure coefficient data generally exhibit very good correlation with the predictions over the entire vane chord, as seen in Figures 31 through 46.

The low incidence first harmonic (reduced frequencies from 8.885 to 10.100) dynamic pressure coefficient data and theory decrease in the chordwise direction, although the data attains a finite, albeit non-zero, value at the vane trailing edge transducer location (97.0% of the chord). Also, at the 10% vane chord, this first harmonic data generally appears to be too low, to varying degrees, with respect to its neighboring data and also the prediction.

The second harmonic (reduced frequencies from 17.77 to 20.20) dynamic pressure coefficient data and prediction also decrease along the vane chord, but both attain a value very nearly equal to zero at the trailing edge transducer location. The value of the dynamic pressure coefficient at the 10% vane chord for this second harmonic data appears to be in good agreement with both its neighboring data and the prediction. This would tend to preclude the possibility of a measurement error at this chordwise location in the first harmonic data discussed above. It should be noted that the finiteness of this trailing edge dynamic pressure coefficient data and also its value reflect upon the validity and the

application of the Kutta condition for unsteady flows to these high reduced frequency values. It should be emphasized that this data was normalized with respect to a vane inlet velocity and density parameter. Hence, an increase or decrease in C_p implies a corresponding change in the magnitude of the measured unsteady pressure.

The aerodynamic phase lag data for the relatively low incidence angles generally correlates with the prediction, although the data appears to be offset in level on the order of 60° as compared to the prediction. The first harmonic phase lag data is smooth over the front half of the vane, correlating with the predictions, but almost always demonstrates a significant negative jump in value at the 50% vane chord transducer location. Aft of this location, this first harmonic data sometimes increases to the general level attained over the front half of the vane, for example Figure 33, and other times remains at the decreased level, as in Figure 39. Examination of the individual vane surface data presented in the Appendix reveals that the first harmonic differential data is generally dominated by the pressure surface over the front 40% of the vane, and by either the pressure surface or the suction surface data over the aft portion of the vane. At the 50% chord location, where the negative jump in phase of

the differential pressure is noted, the pressure and suction surface fluctuating pressures are often equal. Whether the phase jump is maintained over the aft portion of the vane appears to correlate with the cases when the suction surface data is dominant. Similarly, the cases where the phase lag jump increases over the aft portion of the vane correlates with the pressure surface data being dominant. It should be noted that the variation along the chord of the individual pressure and suction surface data is smooth.

The second harmonic aerodynamic phase lag generally correlates well with the predictions, although offset in level on the order of 60°, as previously noted. The jump in phase noted for the first harmonic data is not exhibited in this second harmonic data.

The intermediate negative incidence angle data results are presented in Figures 47 through 54. Deviation between the prediction and the dynamic pressure coefficient and aerodynamic phase lag data herein begin to become very apparent.

The first harmonic dynamic pressure coefficient data-theory correlation is good over the front 60% of the vane surface, with both decreasing in value in the chordwise direction. Over the aft 40% of the vane chord, the prediction continues to decrease whereas the data generally begins to increase

in value. Analogous to the relatively low incidence angle results previously discussed, the 10% chord data appears to be somewhat decreased in value when compared to the neighboring data and to the prediction. However, the magnitude of this apparent decrease is much smaller than for the low incidence angle results. The second harmonic data-theory correlation is quite good over the entire vane, with both decreasing in value along the chord. As per the low incidence angle results previously discussed, the value of the trailing edge dynamic pressure coefficient data is finite, approaching a zero value for the second harmonic (reduced frequencies ranging from 14.536 to 15.114) and a non-zero value for the first harmonic (reduced frequencies from 7.268 to 7.557).

For these intermediate negative incidence angles, this aerodynamic phase lag generally correlates with the predictions over the front 50% of the vane, although offset in level on the order of 75°. Over the aft portion of the vane, and sometimes over some of the front portion as well, this phase lag data (particularly the first harmonic results) indicates that a wave related phenomena is becoming significant. This is evidenced by the fact that over these portions of the vane, the aerodynamic phase lag data is seen to increase in a linear fashion as, for example, seen in Figure 47. Such a linearly increasing phase lag means that an event occurring at one location on the vane occurs at a later time

at a downstream location. Relating this time and distance results in an apparent wake convected speed, as is discussed at some length in Reference 14.

The relatively large negative incidence angle results are presented in Figures 55 through 62. The dynamic pressure coefficient data-prediction for these points is similar to that for the intermediate negative incidence angle points. The first harmonic data and prediction generally decrease in value over the front half of the vane, with the prediction continuing to decrease to the vane trailing edge. The data, however, increases in value over the rear half of the chord. The second harmonic data-theory correlation is generally quite good over the entire vane chord, with both decreasing with increasing chord. Again, the value of the trailing edge dynamic pressure coefficient data (97.0% chord) is non-zero but finite for the first harmonic data (reduced frequency values from 6.795 to 9.86) and approaches zero for the second harmonic data (reduces frequencies from 13.59 to 19.72). Also, the value of the 10% chord dynamic pressure coefficient data is substantially reduced in value as compared to both the neighboring data points and the prediction not only for the first harmonic data as was previously noted for the low incidence data, but also for the second harmonic data for the first time.

The aerodynamic phase lag data at the vane leading edge transducer location (2.94% chord) correlates extremely well with the prediction for both the first and second harmonic data. However, a wave related phenomena, as evidenced by the linear increase in phase along the chord as seen in Figure 55, for example, is now generally present over the entire vane chord for these large negative incidence angles. This is contrasted to the appearance of a wave phenomena over the aft portion of the vane for the intermediate negative incidence angle, and no evidence of a wave phenomena for the low incidence angle results.

SUMMARY AND CONCLUSIONS

The fundamental time-variant aerodynamics relevant to forced response of a downstream vane of realistic geometry, with the primary source of excitation being the wakes from upstream rotor blades, were experimentally determined for two representative values of the rotor-stator axial spacing ratio. The vane incidence angle ranged from $+\frac{1}{2}°$ to $-12\frac{1}{2}$ and the reduced frequency from 6.795 to 20.20. The dynamic data provided qualitative information describing the rotor wake velocity as a function of both compressor loading and downstream axial distance as well as a quantitative description of the resulting time-variant pressures induced by these wakes on the surfaces of the downstream stator vanes. This vane pressure and suction surface unsteady data was used to determine the unsteady pressure difference across a single vane and this difference data correlated with appropriate predictions from a state-of-the-art cascade transverse gust analysis.

The rotor wake data demonstrated that at a constant axial distance from the rotor blades, the wake width and velocity deficit increase with loading. As the axial distance from the rotor increases, the wake decays much more rapidly for high values of compressor loading than for low values.

The overall levels of the time-variant pressure on the vane pressure and suction surfaces were found to increase with loading at approximately the same rate for each value of the rotor-stator axial spacing ratio. On the 100% speed line, this increase in overall level was particularly pronounced for the small value of the spacing ratio. No overall differences with spacing ratio were apparent on the 70% speed line. Thus, from this data it would appear that increasing the rotor-stator axial spacing is not a universal method to be used to alleviate forced response problems, a result in agreement with experience.

The correlation of the dynamic data describing the unsteady pressure difference across the vane with the flat plate cascade transverse gust analysis was generally good for low incidence angles, becoming less acceptable as the incidence became increasingly negative. This decreased correlation was seen to be due to the appearance of a wave related phenomena coming into existence on the vane as the incidence angle was decreased.

The low incidence angle aerodynamic phase lag data always correlated with the prediction over the front 40% of the vane. However, at 50% of the chord, a significant negative jump in phase was generally noted. Over the rear half of the vane, the phase lag data sometimes remained at this level

and other times increased to the level found over the front of the vane. Examination of the individual surface unsteady data revealed that these results correlated with the domination of the unsteady pressure differential by either the pressure or suction surface data. This type of correlation clearly demonstrates the necessity for acquiring individual surface unsteady data and then calculating the pressure difference as opposed to measuring this pressure differential directly.

The first and second harmonic dynamic pressure coefficient data generally decreases in the chordwise direction and is finite at the trailing edge transducer location (97.0% chord). The value of this trailing edge coefficient for the first harmonic data (reduced frequencies from 6.795 to 10.1) was non-zero whereas the second harmonic value (reduced frequencies from 13.59 to 20.20) approached zero. The fact that this trailing edge value is finite, as well as its value, reflects upon the validity and the application of the Kutta condition for unsteady flows at these high reduced frequency values.

REFERENCES

1. Whitmore, J. M., Lull, W. R., and Adams, M. D., "How Sound Affects Vibration in Modern Aircraft Engines", General Motors Engineering Journal, November-December, 1955.

2. Sears, W. R., "Some Aspects of Non-Stationary Airfoil Theory and Its Practical Application", Journal of the Aeronautical Sciences, Vol. 8, No. 3, 1941.

3. Horlock, J. H., "Fluctuating Lift Forces on Airfoils Moving Through Transverse and Chordwise Gusts", Transactions of the ASME, Journal of Basic Engineering, Vol. 90, Series D, No. 4, December 1968.

4. Naumann, H. and Yeh, H., "Lift and Pressure Fluctuations of a Cambered Airfoil Under Periodic Gusts and Applications in Turbomachinery", Transactions of the ASME, Journal of Engineering for Power, Vol. 95, Series A, No. 1, January 1973, pp. 1-10.

5. Goldstein, M. E. and Atassi, H., "A Complete Second-Order Theory for the Unsteady Flow About an Airfoil Due to a Periodic Gust", Journal of Fluid Mechanics, Vol. 74, 1976.

6. Whitehead, D. S., "Force and Moment Coefficients for Vibrating Airfoils in Cascade", Aeronautical Research Council R and M 3254, February 1960.

7. Fleeter, S., "Fluctuating Lift and Moment Coefficients for Cascaded Airfoils in a Nonuniform Compressible Flow", AIAA Journal of Aircraft, Vol. 10, No. 2, February 1973.

8. Smith, S. N., "Discrete Frequency Sound Generation in Axial Flow Turbomachines", University of Cambridge, Department of Engineering Report CUED/A-Turbo/TR 29, 1971.

9. Fleeter, S., Novick, A. S., and Riffel, R. E., "The Unsteady Aerodynamic Response of an Airfoil Cascade to a Time-Variant Supersonic Inlet Flow Field", AGARD-CP-177, Unsteady Phenomena in Turbomachinery, 1975.

10. Chadwick, W. R., Bell, J. K., and Platzer, M. F., "On the Analysis of Supersonic Flow Past Oscillating Cascades", AGARD-CP-177, Unsteady Phenomena in Turbomachinery, 1975.

11. Commerford, G. L. and Carta, F. O., "Unsteady Aerodynamic Response of a Two-Dimensional Airfoil at High Reduced Frequency," AIAA Journal, Vol. 12, No. 1, 1974.

12. Ostdiek, F. R., "A Cascade in Unsteady Flow", Ph.D. Thesis, The Ohio State University, 1975.

13. Bruce, E. P. and Henderson, R. E., "Axial Flow Rotor Unsteady Response to Circumferential Inflow Distortions", Project SQUID Technical Report PSU-13-P, September 1975.

14. Fleeter, S., Jay, R. L. and Bennett, W. A., "Compressor Stator Time-Variant Aerodynamic Response to Compressor Rotor Wakes", DDA EDR 9005, Air Force Office of Scientific Research Report TF-77-0066, November 1976.

15. Carta, F. O. and St. Hilaire, A. O., "Experimentally Determined Stability Parameters of a Subsonic Cascade Oscillating Near Stall", ASME Paper No. 77-GT-47, 1977.

16. Novick, A. S., Jay, R. L., Sinnet, G. T., and Fleeter, S., "An Experimental Investigation of Unsteady Airfoil Motion in a Supersonic Stream", Unsteady Aerodynamics, Vol. I & II, Edited by R. B. Kinney, Proceedings of a Symposium held at the University of Arizona, March 1975.

17. Fleeter, S., Novick, A. S., and Riffel, R. E., "An Experimental Investigation of the Unsteady Aerodynamics in a Controlled Oscillating Cascade", ASME Journal of Engineering for Power, Vol. 99, No. 1, January 1977.

18. Fleeter, S., and Riffel, R. E., "An Experimental Investigation of the Unsteady A rodynamics of a Controlled Oscillating MCA Airfoil Cascade", Office of Naval Research Technical Report, DDA EDR 9028, December 1976.

ACKNOWLEDGMENT

This research was sponsored, in part, by the Air Force Office of Scientific Research (AFSC), United States Air Force, under Contract F49620-77-C-0024 to Detroit Diesel Allison Division of General Motors Corporation. The Unites States Government is authorized to reproduce and distribute reprints for governmental purposes notwithstanding any copyright notation thereon.

	ROTOR	STATOR
Type of Airfoil	65 Series	65 Series
Number	42	40
Chord, C-in. (Cm.)	4.589(11.66)	5.089(12.93)
Solidity, σ = C/S	1.435	1.516
Camber, ϕ - Deg.	20.42	48.57
Aspect Ratio, AR = S/C	1.046	0.943
Leading Edge Radius/C	0.0044	0.0049
Trailing Edge Radius/C	0.0028	0.0030
Inlet Angle, β_1 - Deg.	59.38	37.84
Exit Angle, β_2 - Deg.	42.41	0.00
Loss Coefficient	0.043	0.056
Diffusion Factor	0.449	0.410
Rotor-Stator Axial Spacing-in.(Cm.)	1.485(3.772)	
Flow Rate	31.02 lb/sec. (14.07 Kg/Sec)	
Tip Speed	183.5 ft/sec. (5593.1 Cm/Sec)	
Rotational Speed	876.3 rpm	
Stage Pressure Ratio	1.0125	
Inlet Tip Diameter	48.01 in. (121.95 Cm)	
Hub/Tip Radius Ratio	0.80	
Stage Efficiency, Percent	88.1	

TABLE I. AIRFOIL MEAN SECTION CHARACTERISTICS AND COMPRESSOR DESIGN POINT CONDITIONS

COMPRESSOR	NUMBER OF STAGES	AVERAGE ROTOR-STATOR AXIAL SPACING* / ROTOR AXIAL CHORD
A	11	0.4909
B	6	0.4619
C	10	0.3318
D	5	0.1534
Research Build #1	1	0.2374
Research Build #2	1	0.4305

*Measured at mid-span.

TABLE II. DESCRIPTION OF FOUR ADVANCED DESIGN COMPRESSORS AND RESEARCH COMPRESSOR ROTOR-STATOR AXIAL SPACING RATIOS

PRESSURE SURFACE		SUCTION SURFACE	
X/C*	Y/C*	X/C*	Y/C*
- 45.04	8.102	55.01	8.184
- 44.08	8.550	54.82	7.895
- 42.30	8.182	53.68	7.324
- 40.45	7.701	47.96	4.655
- 38.01	7.029	43.41	2.749
- 35.95	6.465	37.76	0.656
- 33.77	5.889	33.28	- 0.784
- 30.90	5.166	28.85	- 2.018
- 28.48	4.594	23.40	- 3.272
- 25.94	4.038	19.12	- 4.052
- 22.60	3.368	14.91	- 4.641
- 19.81	2.863	9.79	- 5.125
- 16.15	2.274	5.81	- 5.317
- 13.10	1.847	.98	- 5.341
- 9.93	1.460	- 2.75	- 5.197
- 5.61	1.045	- 6.35	- 4.926
- 2.37	0.778	- 10.67	- 4.417
1.17	0.576	- 13.98	- 3.893
5.77	0.432	- 17.16	- 3.278
9.58	0.413	- 20.93	- 2.401
14.50	0.525	- 23.79	- 1.631
18.57	0.739	- 27.18	- 0.595
22.75	1.077	- 29.74	0.273
28.12	1.698	- 32.16	1.171
32.53	2.376	- 34.99	2.323
37.04	3.232	- 37.11	3.258
42.80	4.594	- 39.10	4.205
47.47	5.940	- 41.39	5.402
53.39	7.984	- 43.06	6.382
54.58	8.446	- 44.57	7.442

*Expressed in percent

TABLE III. STATOR MEAN PROFILE COORDINATES

PRESSURE SURFACE AND SUCTION SURFACE

PERCENT VANE CHORD
2.94
10.0
20.0
30.0
40.0
50.0
60.0
70.0
80.0
90.0
97.0

TABLE IV. CHORDWISE LOCATION OF DYNAMIC PRESSURE TRANSDUCERS

NOMINAL QUANTITIES:

V_{ABS} = 122 feet/second (37.18 meters/second)

β_{ABS} = 37.5°

R = 21.6 in. (54.9 cm.)

RPM = 876

β_{REL} = 43.20°

L_{PROBE} = 0.317 in. (0.805 cm.)

PERTURBATION	RESULTING PHASE LAG ERROR
$\pm$ 0.1 in. (.25 cm.) Radial	$\pm$ 1°
$\pm$ 2° β_{ABS}	0°
$\pm$ 5% V_{ABS}	$\pm$ 2°
$\pm$ 10% L_{PROBE}	$\pm$ 4.5°
$\pm$ 0.1 in. (.25 cm.) Axial	$\pm$ 10°
$\pm$ 0.1 in. (.25 cm.) Circumferential	$\pm$ 11°

TABLE V. POTENTIAL SOURCES OF ERROR

UNLOADED CONDITION

% CHORD	FIRST HARMONIC PHASE(DEGREES) RUN 1	FIRST HARMONIC PHASE(DEGREES) RUN 2	SECOND HARMONIC PHASE(DEGREES) RUN 1	SECOND HARMONIC PHASE(DEGREES) RUN 2
2.94 P	- 210	- 211	- 94	- 105
10.0 P	- 17	- 25	- 2	- 10
20.0 P	- 176	- 175	- 213	- 218
30.0 P	- 269	- 272	- 63	- 65
2.94 S	33	27	- 176	- 184
10.0 S	25	8	- 124	- 135
20.0 S	- 242	- 244	- 159	- 170
30.0 S	- 271	- 278	- 23	- 23

LOADED CONDITION

2.94 P	- 223	- 224	- 84	- 86
20.0 P	- 228	- 229	- 99	- 98
40.0 P	- 224	- 225	- 157	- 159
60.0 P	- 230	- 231	- 182	- 188
80.0 P	- 231	- 233	- 204	- 200
97.0 P	- 233	- 233	- 186	- 211
2.94 S	- 10	- 8	- 265	- 268
20.0 S	- 260	- 259	38	51
40.0 S	- 225	- 229	- 125	- 316
60.0 S	- 236	- 237	- 176	- 175
80.0 S	- 234	- 235	- 193	- 189
97.0 S	62	55	- 184	- 192

TABLE VI. AERODYNAMIC PHASE LAG DATA REPEATABILITY FOR LOADED AND UNLOADED CONDITIONS ON THE 100% SPEED LINE

DATA POINT	AXIAL SPACING RATIO	% SPEED	β_{ABS}	$K_{1\,AX}$	$K_{2\,AX}$	$v/V)_1$	$u/V)_1$	$v/V)_2$	$u/V)_2$
1	0.2374	100	25	6.80	13.60	.02911	.02113	.03232	.01835
2	0.2374	100	28	7.56	15.12	.0300	.01912	.03294	.01692
3	0.2374	100	33	8.88	17.76	.1117	.07526	.09862	.04184
4	0.2374	100	36	9.86	19.72	.03316	.0239	.03566	.01976
5	0.2374	70	25	6.90	13.80	.03358	.02299	.03523	.01760
6	0.2374	70	28	7.54	15.08	.1156	.080	.0999	.04368
7	0.2374	70	33	9.12	18.24	.06788	.0381	.06720	.02108
8	0.2374	70	38	10.1	20.2	.06830	.03049	.06941	.01907
9	0.4305	100	25	6.95	13.90	.03148	.01973	.03203	.01583
10	0.4305	100	28	7.27	14.54	.03306	.01845	.03452	.01556
11	0.4305	100	33	8.96	17.92	.07811	.02499	.06258	.01813
12	0.4305	100	36	10.05	20.10	.10798	.01652	.07397	.00754
13	0.4305	70	25	6.95	13.90	.03388	.02602	.03622	.01863
14	0.4305	70	28	7.40	14.80	.03630	.02360	.03826	.01891
15	0.4305	70	33	8.91	17.82	.07803	.03156	.06462	.02419
16	0.4305	70	36	9.82	19.64	.12118	.02614	.08612	.01381

TABLE VII. STEADY-STATE DATA IDENTIFICATION AND DESCRIPTION OF TIME-VARIANT PARAMETERS

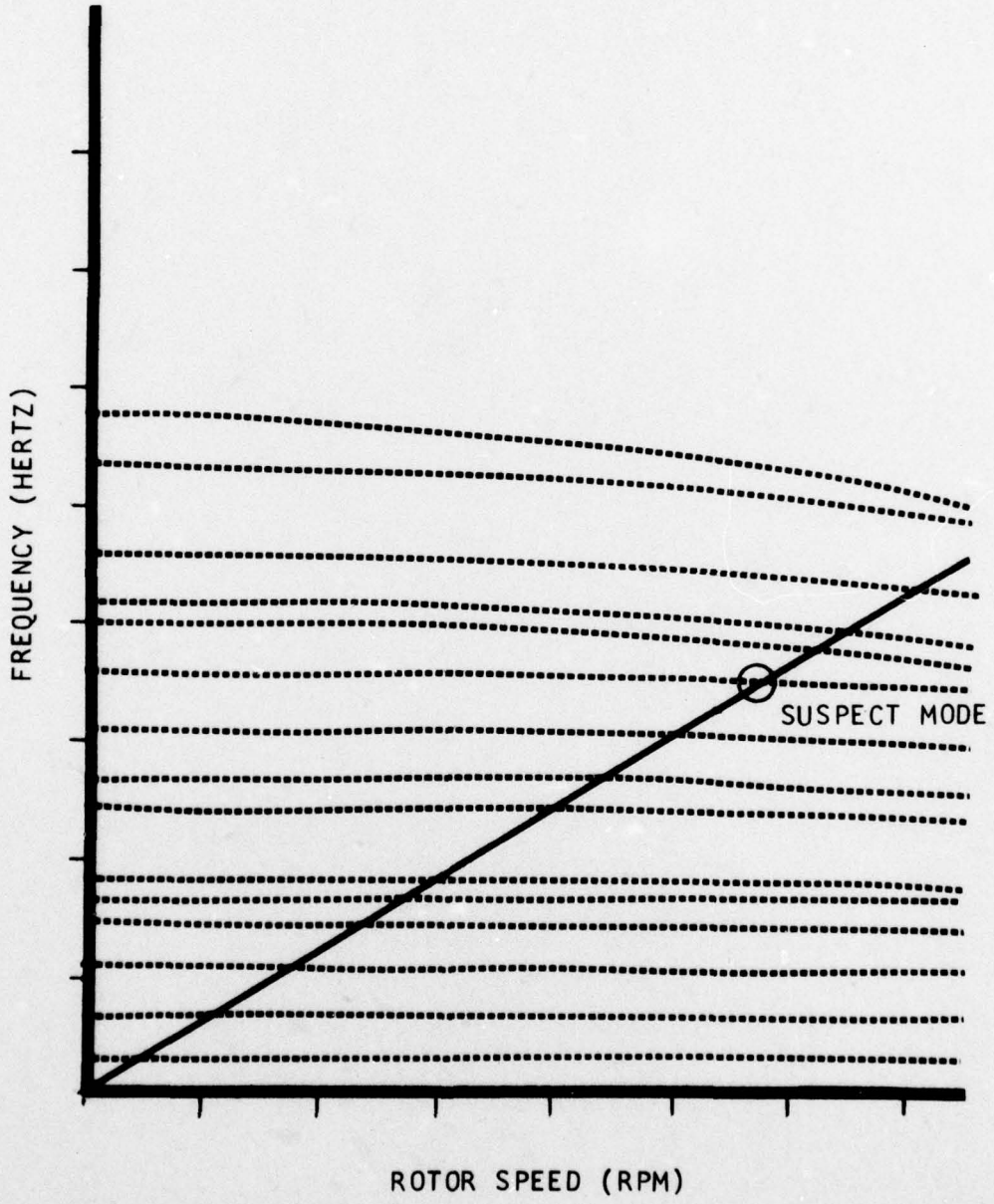

FIGURE 1. FREQUENCY-SPEED DIAGRAM FOR A ROTOR BLADE IN WHICH A CRACK WAS FOUND

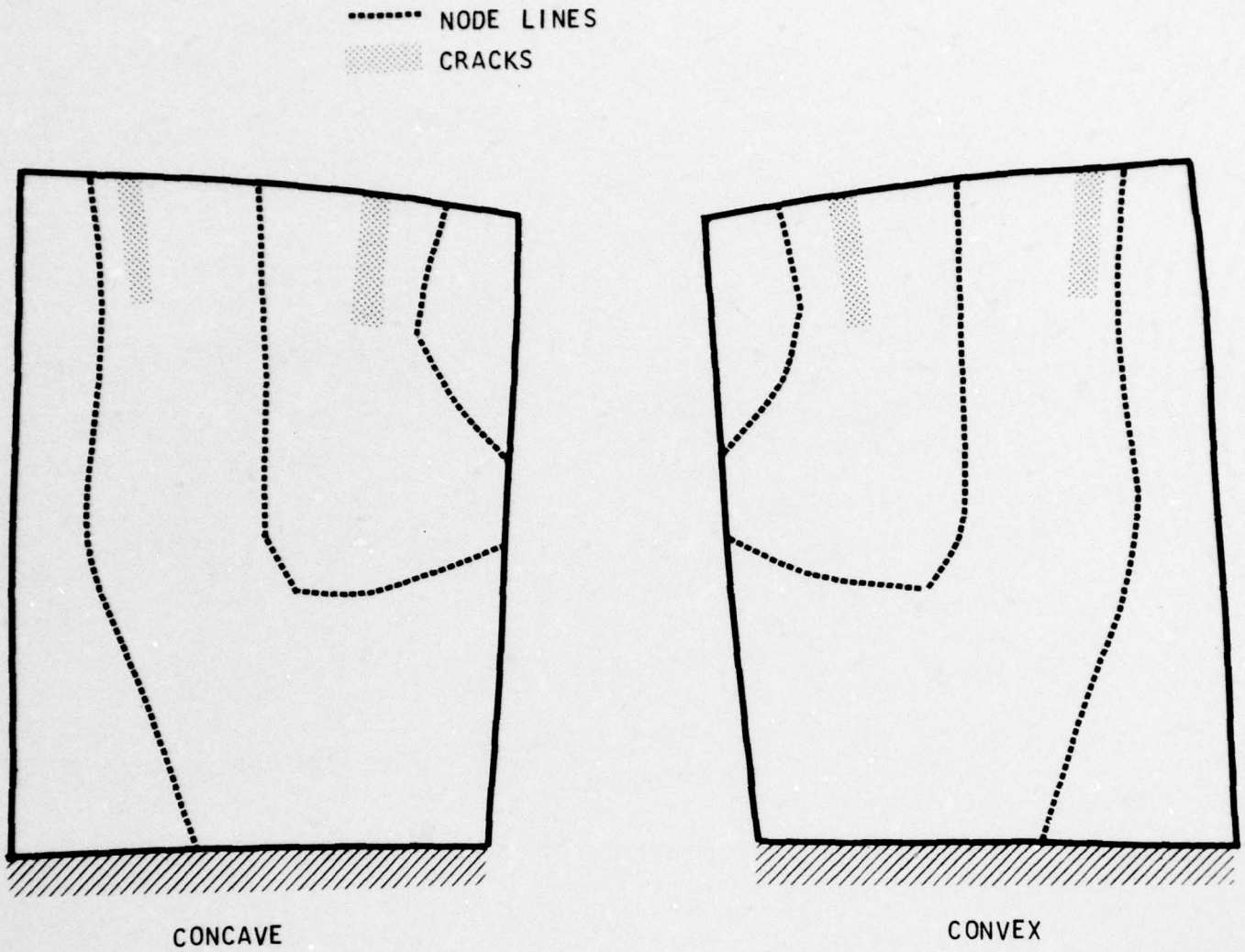

FIGURE 2. CALCULATED MODE SHAPE FOR THE RESONANCE OF A ROTOR IN WHICH A CRACK WAS FOUND

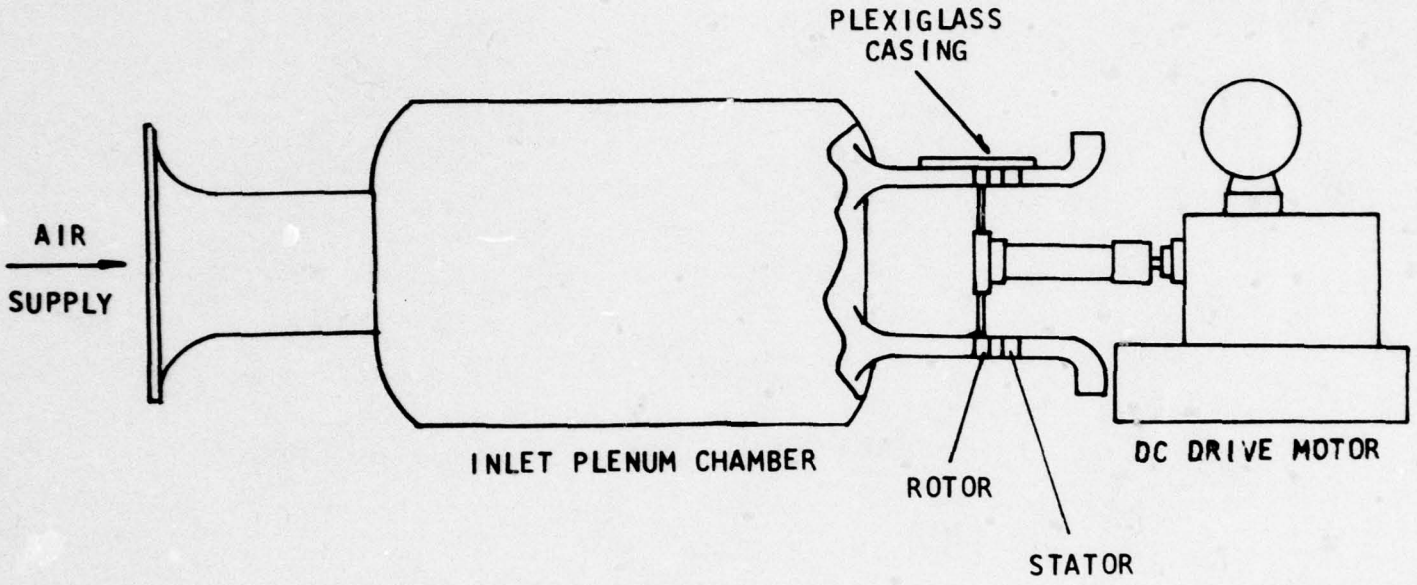

FIGURE 3. SCHEMATIC OF LARGE-SCALE, LOW-SPEED, SINGLE-STAGE RESEARCH COMPRESSOR

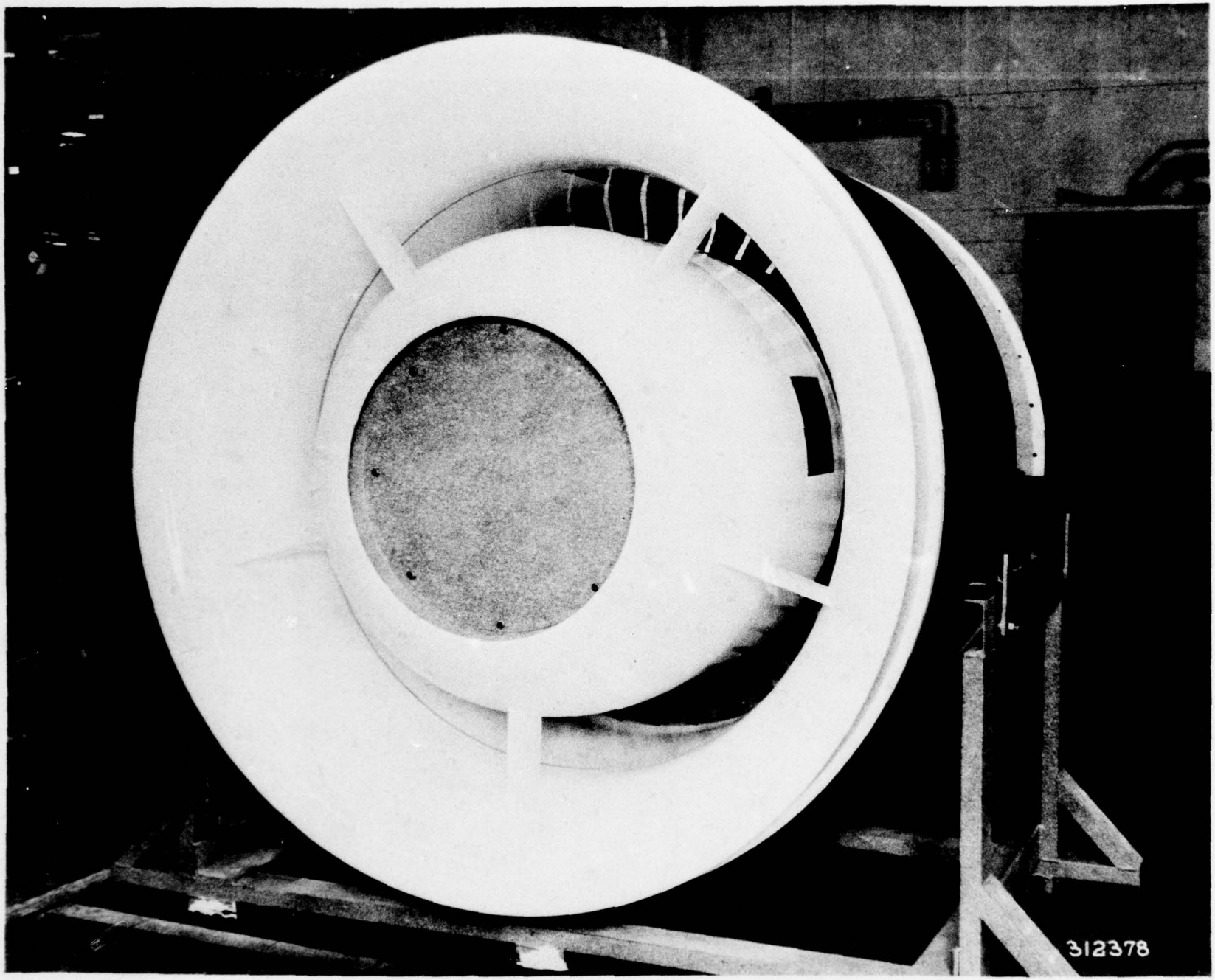

FIGURE 4. VIEW OF ASSEMBLED RESEARCH COMPRESSOR RIG

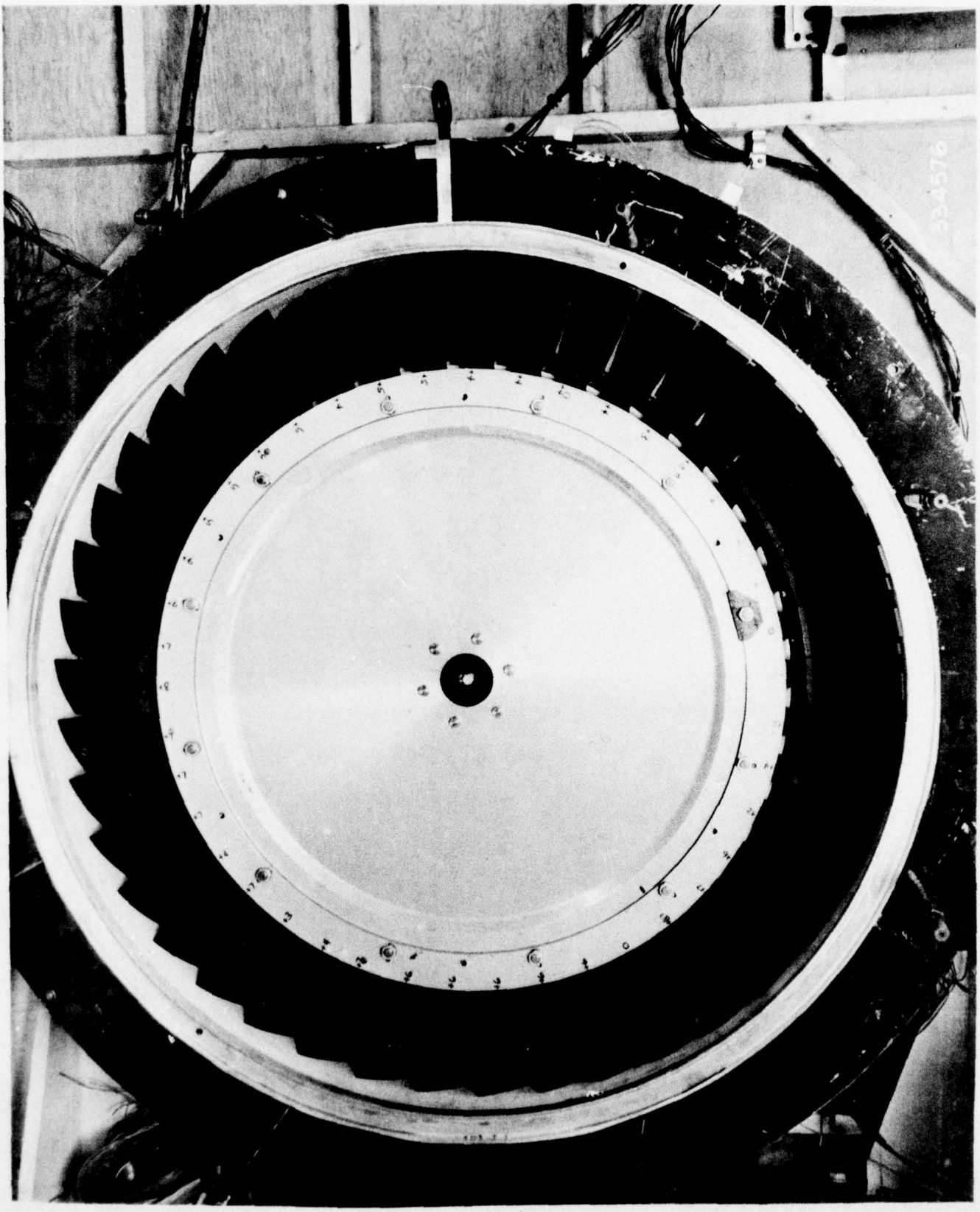

FIGURE 5. SINGLE-STAGE RESEARCH COMPRESSOR ROTOR

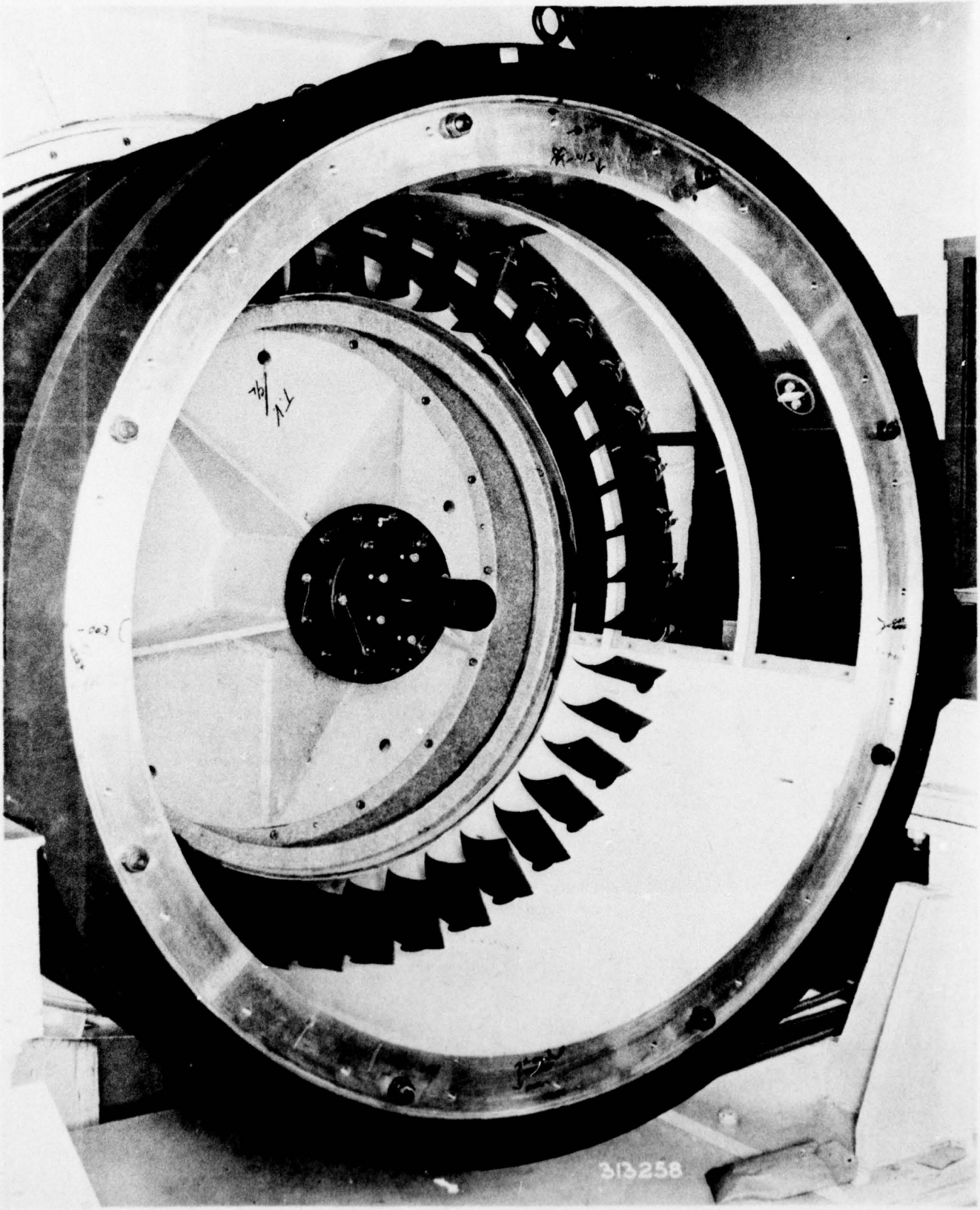

FIGURE 6. VIEW OF 40 VANE STATOR ROW

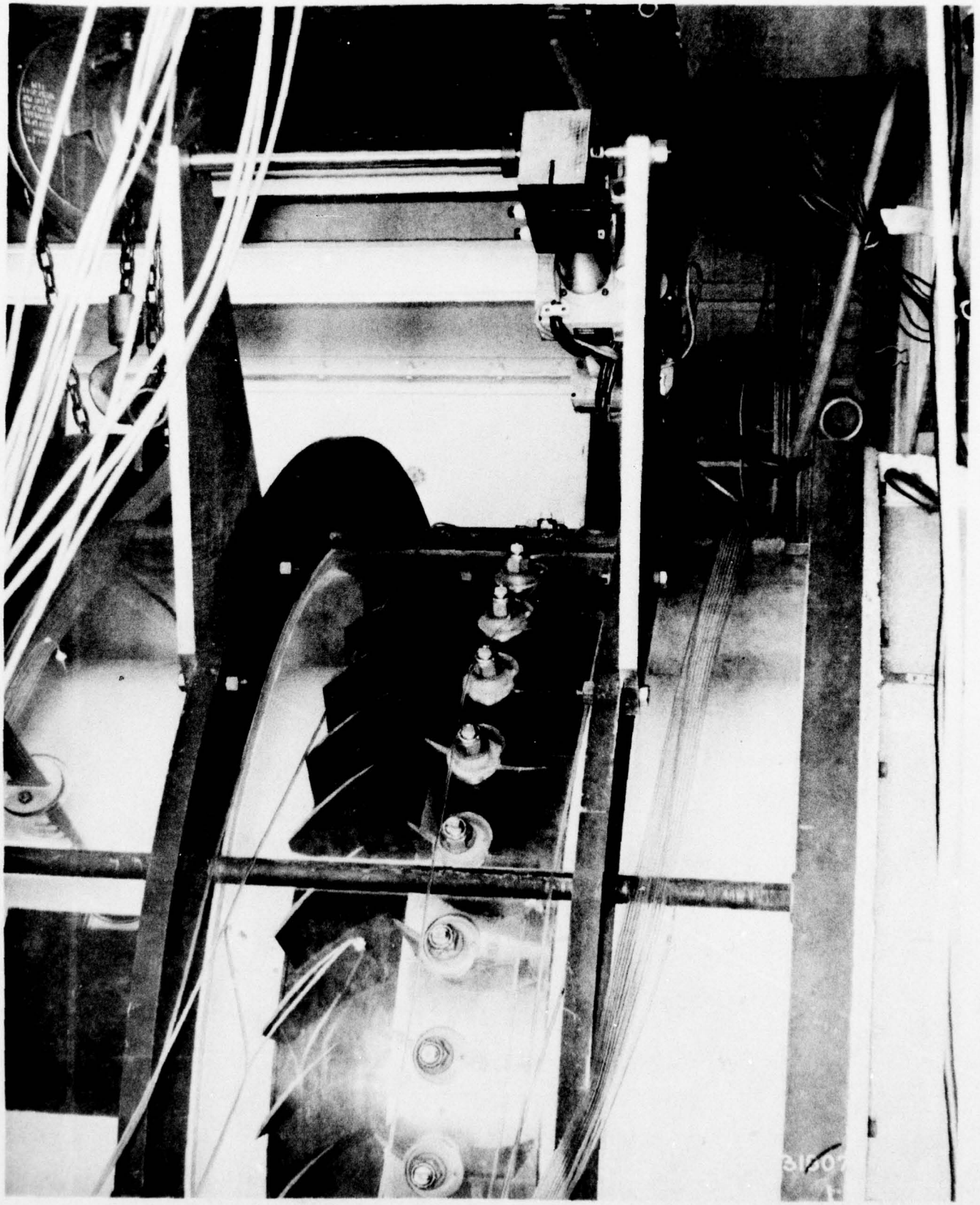

FIGURE 7. VIEW OF ROTOR AND STATOR ROW

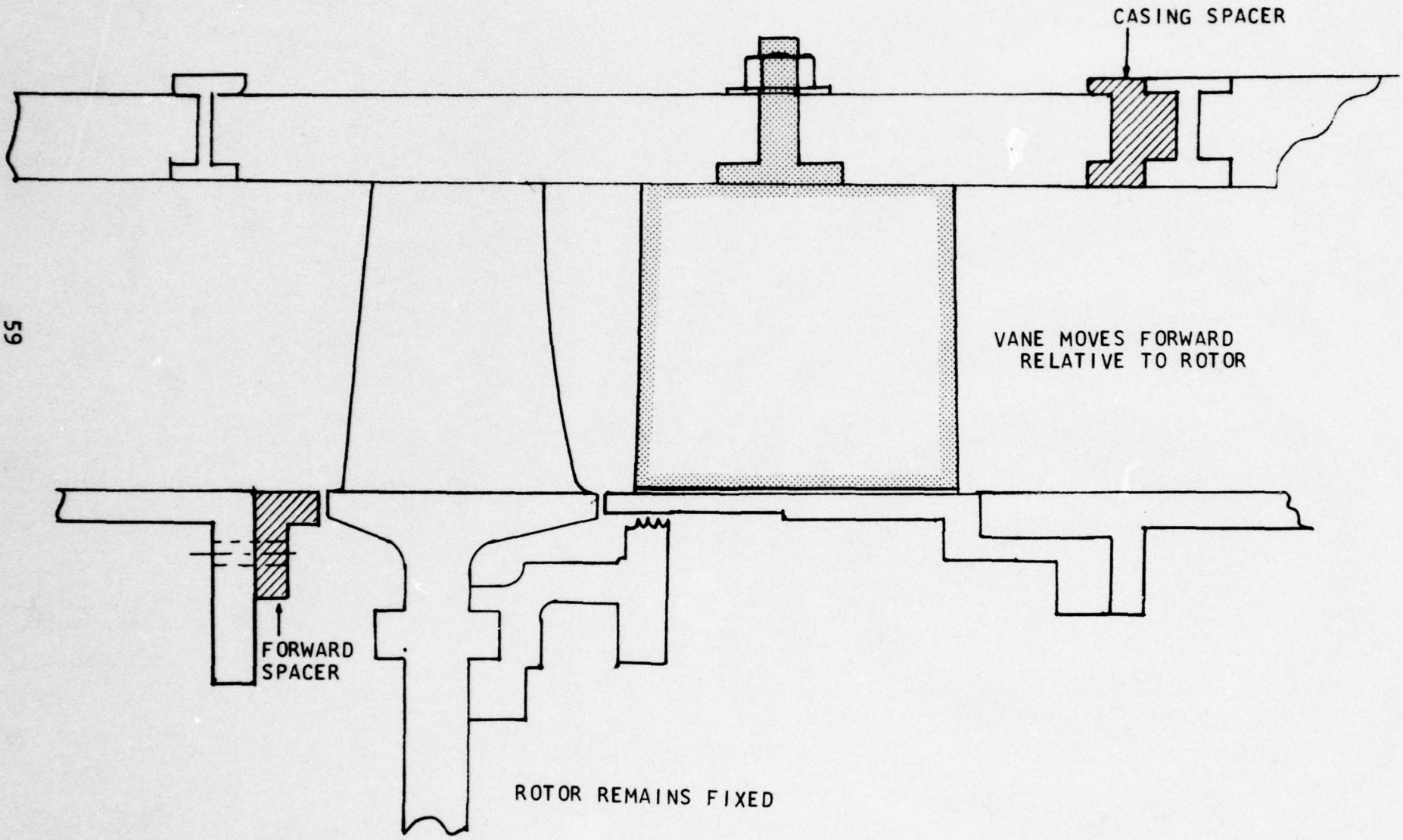

FIGURE 8. SCHEMATIC SHOWING HARDWARE TO REDUCE ROTOR-STATOR AXIAL SPACING

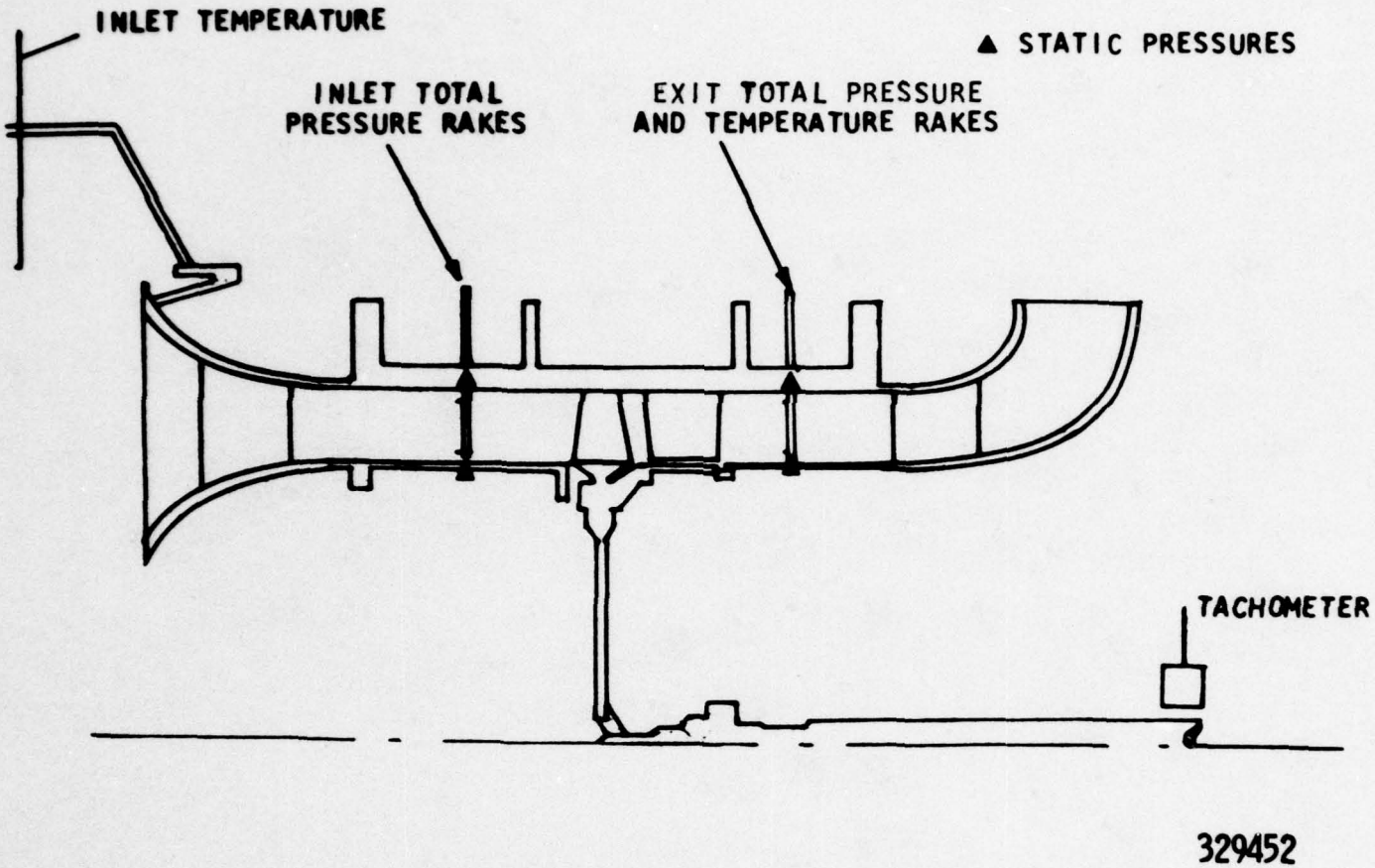

FIGURE 9. SCHEMATIC OF STEADY-STATE INSTRUMENTATION AND COMPRESSOR FLOW PATH

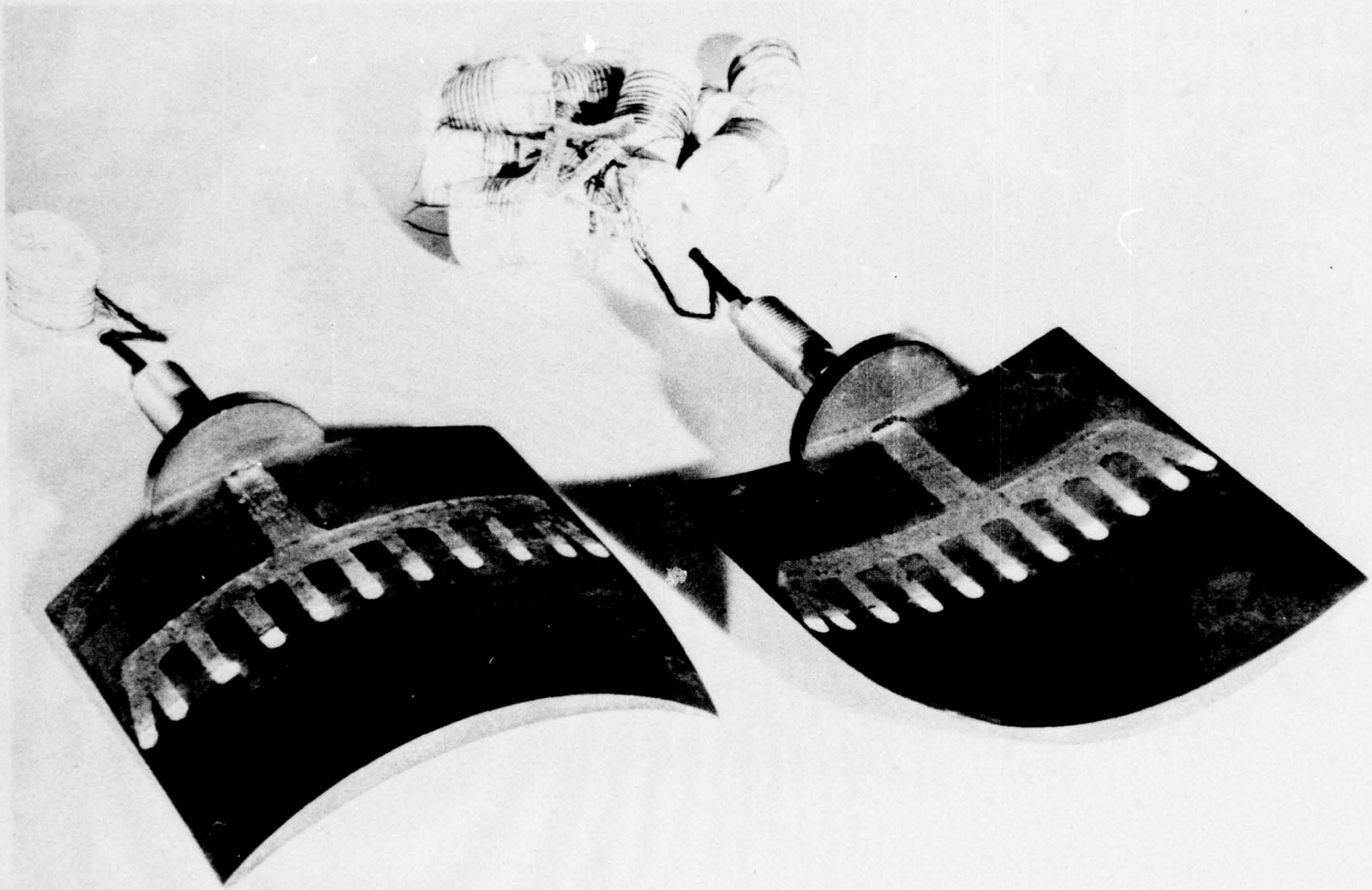

FIGURE 10. DYNAMICALLY INSTRUMENTED STATOR VANES

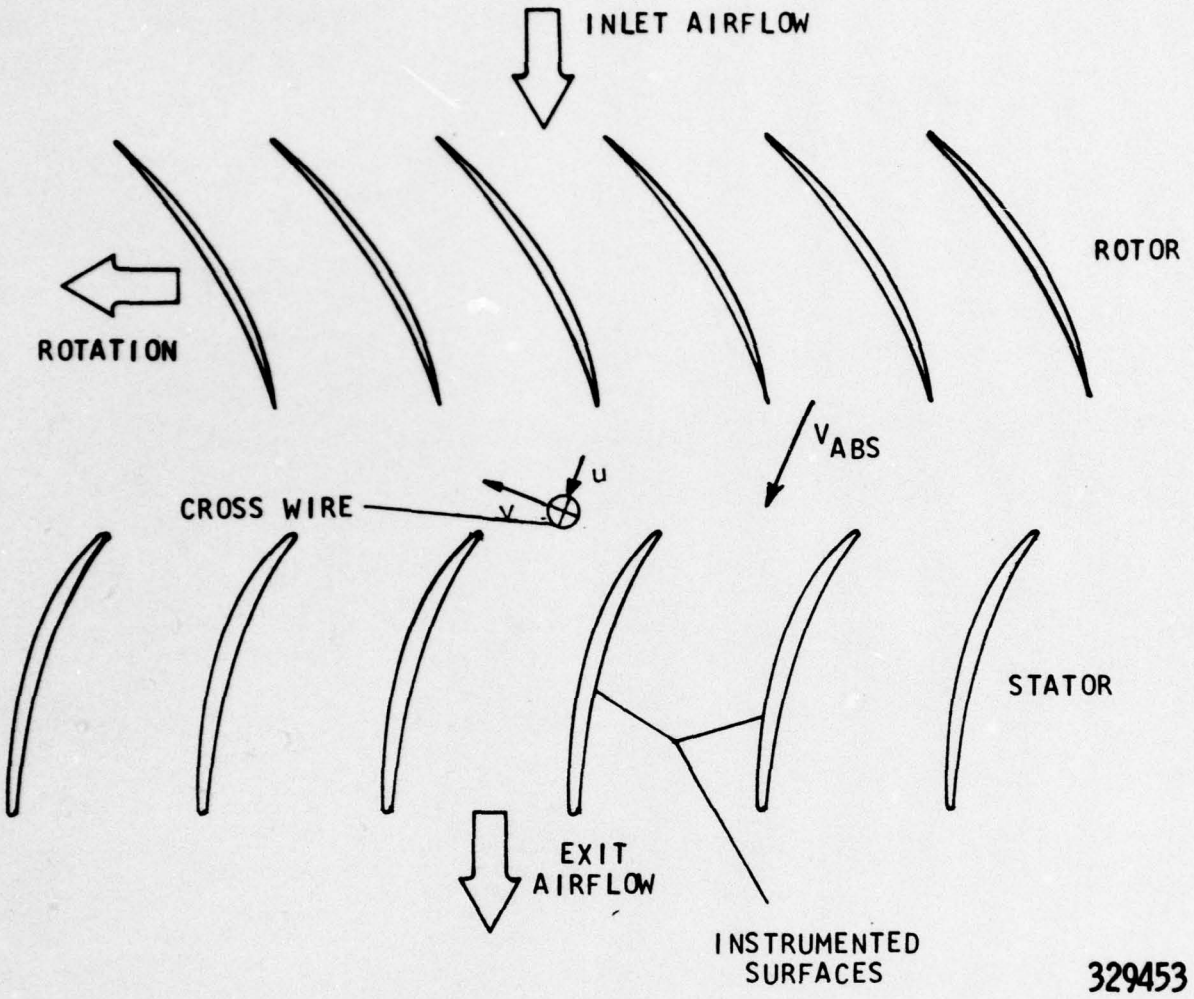

FIGURE 11. SCHEMATIC OF DYNAMIC INSTRUMENTATION

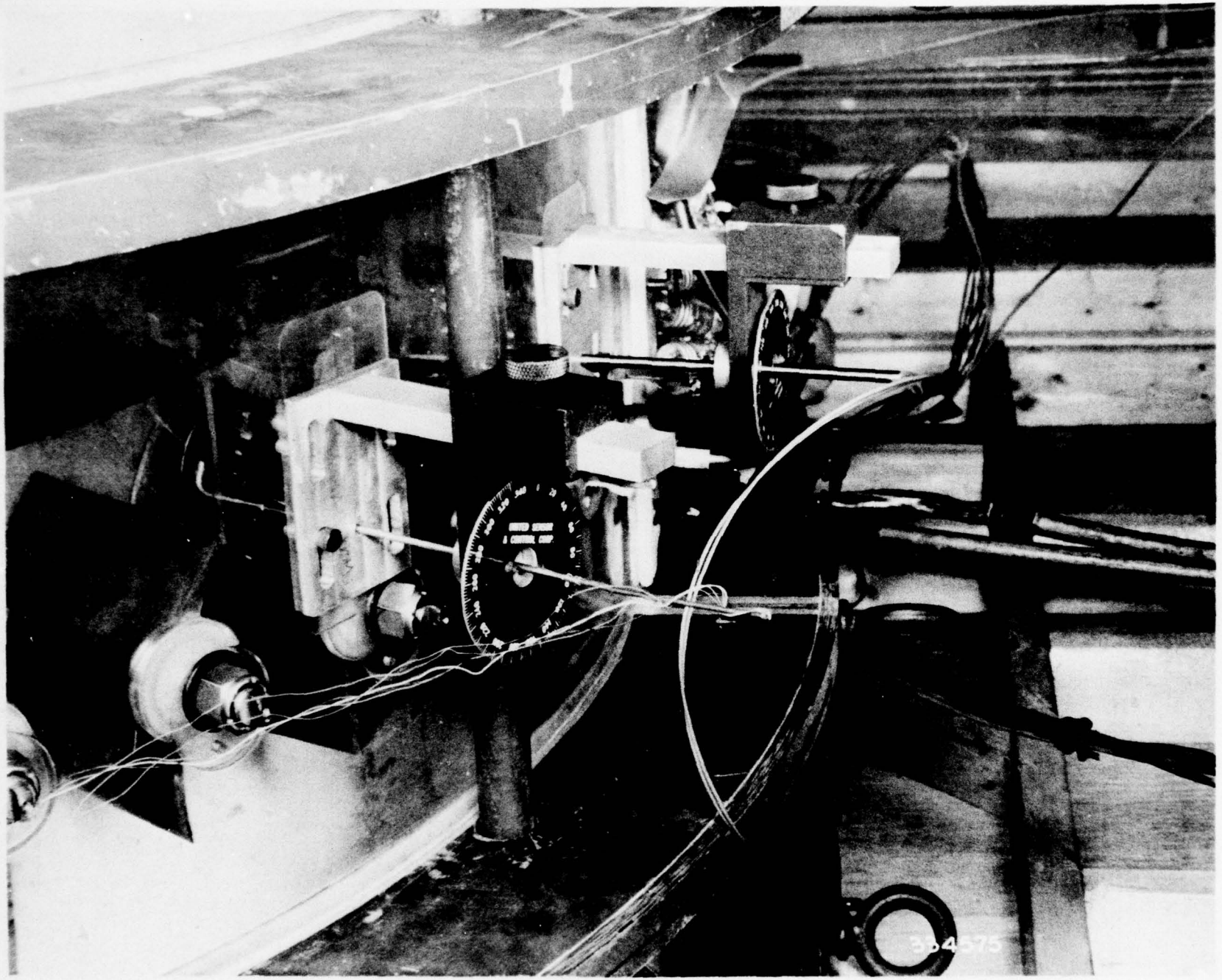

FIGURE 12. PROBE HOLDERS FOR CROSS-WIRE AND DYNAMIC TOTAL PRESSURE PROBE MOUNTED ON CASING EXTERIOR

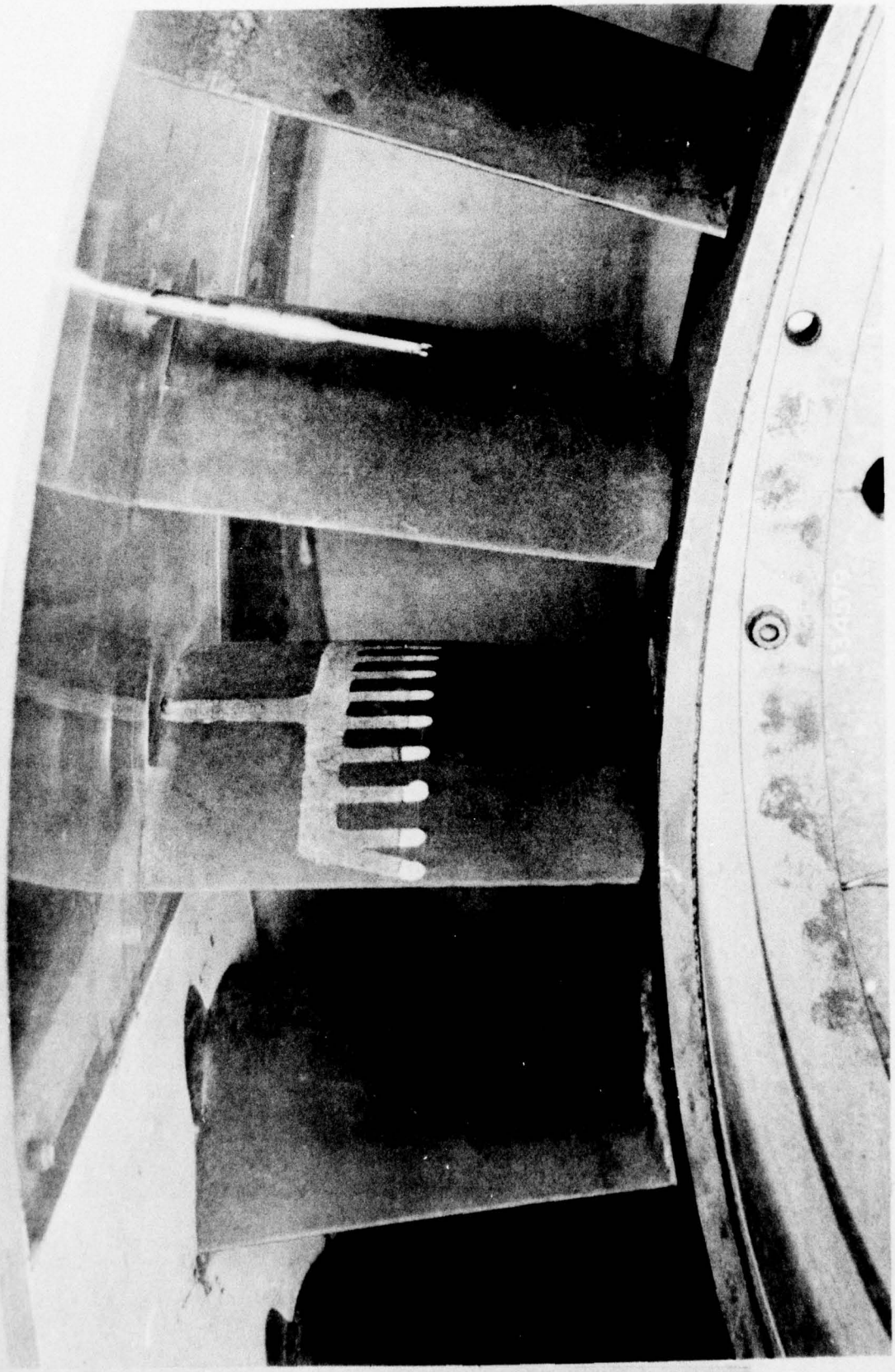

FIGURE 13. VIEW OF CROSS-WIRE PROBE AND INSTRUMENTED VANE SUCTION SURFACE

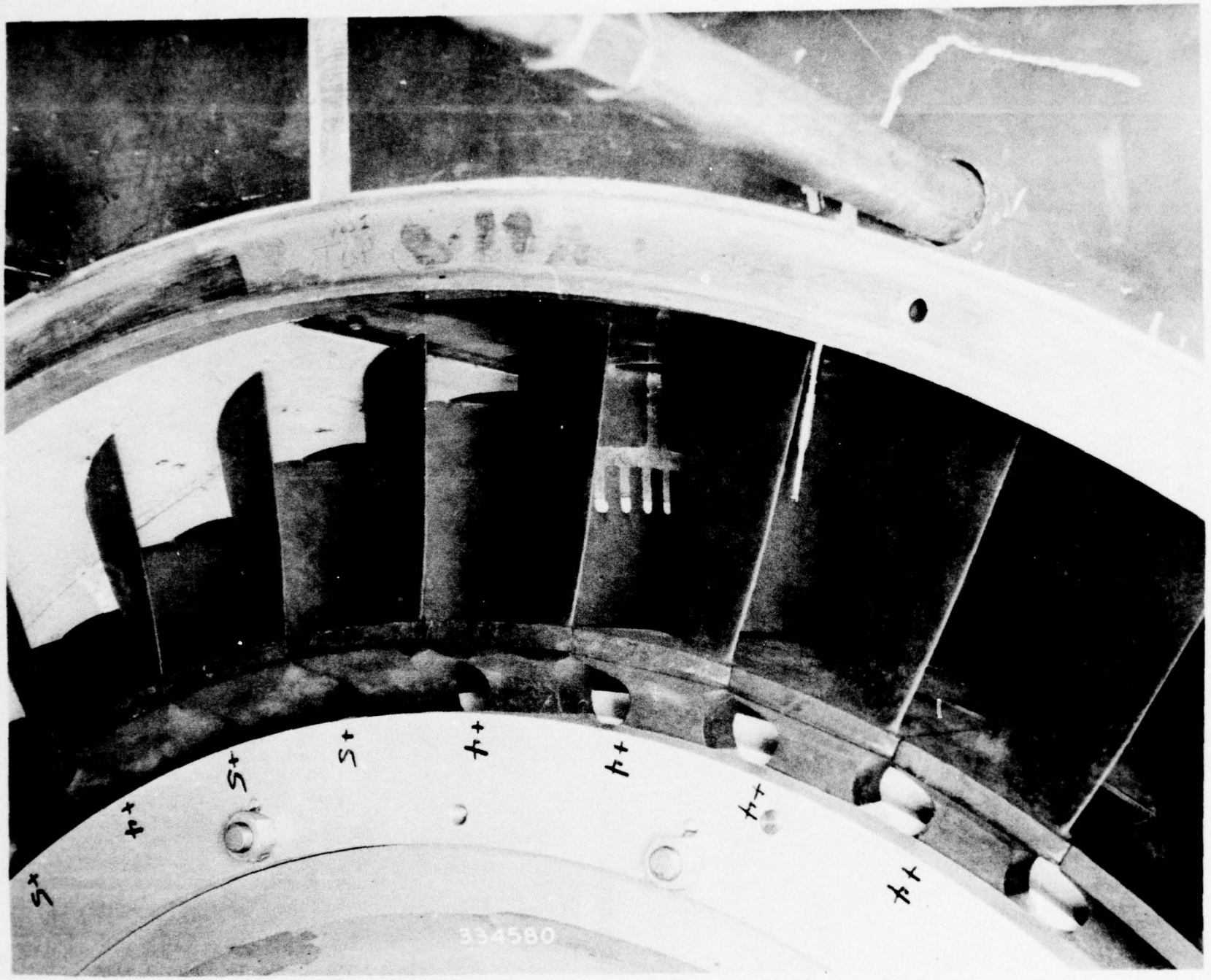

FIGURE 14. VIEW OF CROSS-WIRE PROBE AND INSTRUMENTED VANE SUCTION SURFACE WITH ROTOR INSTALLED

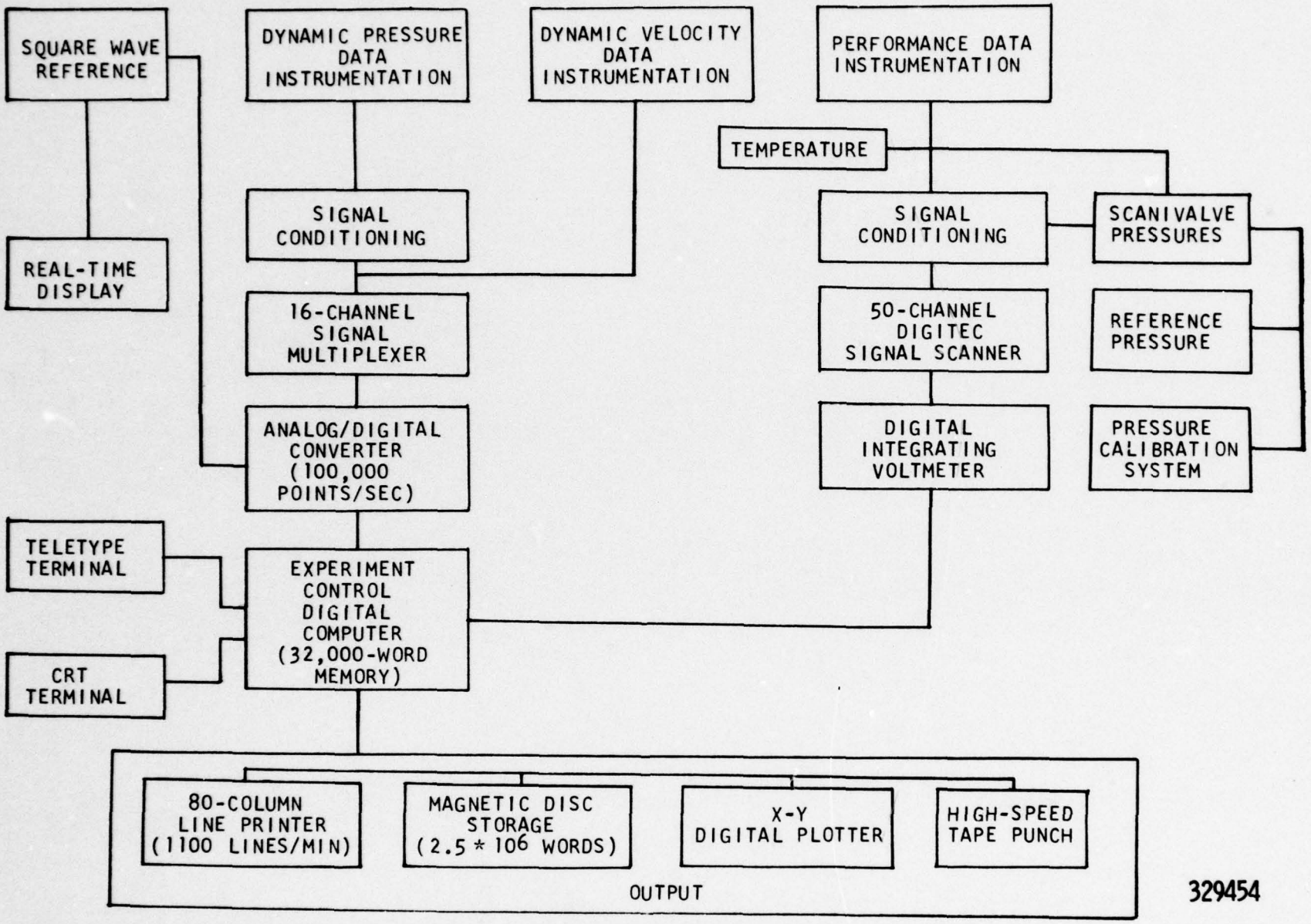

FIGURE 15. SCHEMATIC OF ON-LINE COMPUTER CONTROLLED DATA ACQUISITION SYSTEM

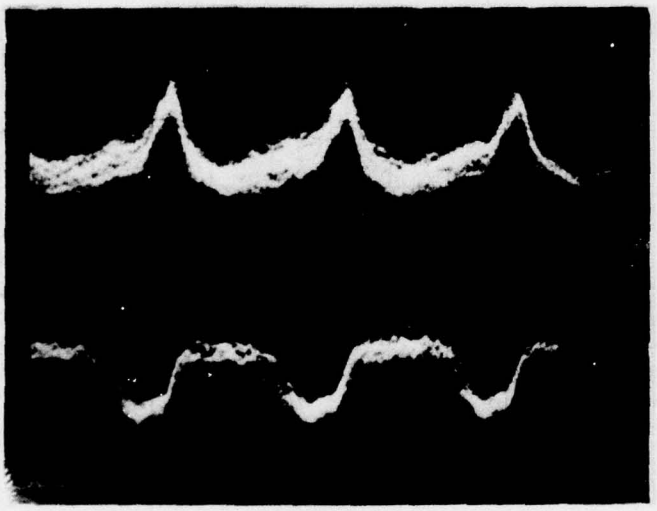

FIGURE 16. EXAMPLE OF ON-LINE ANALOG AVERAGED SIGNALS

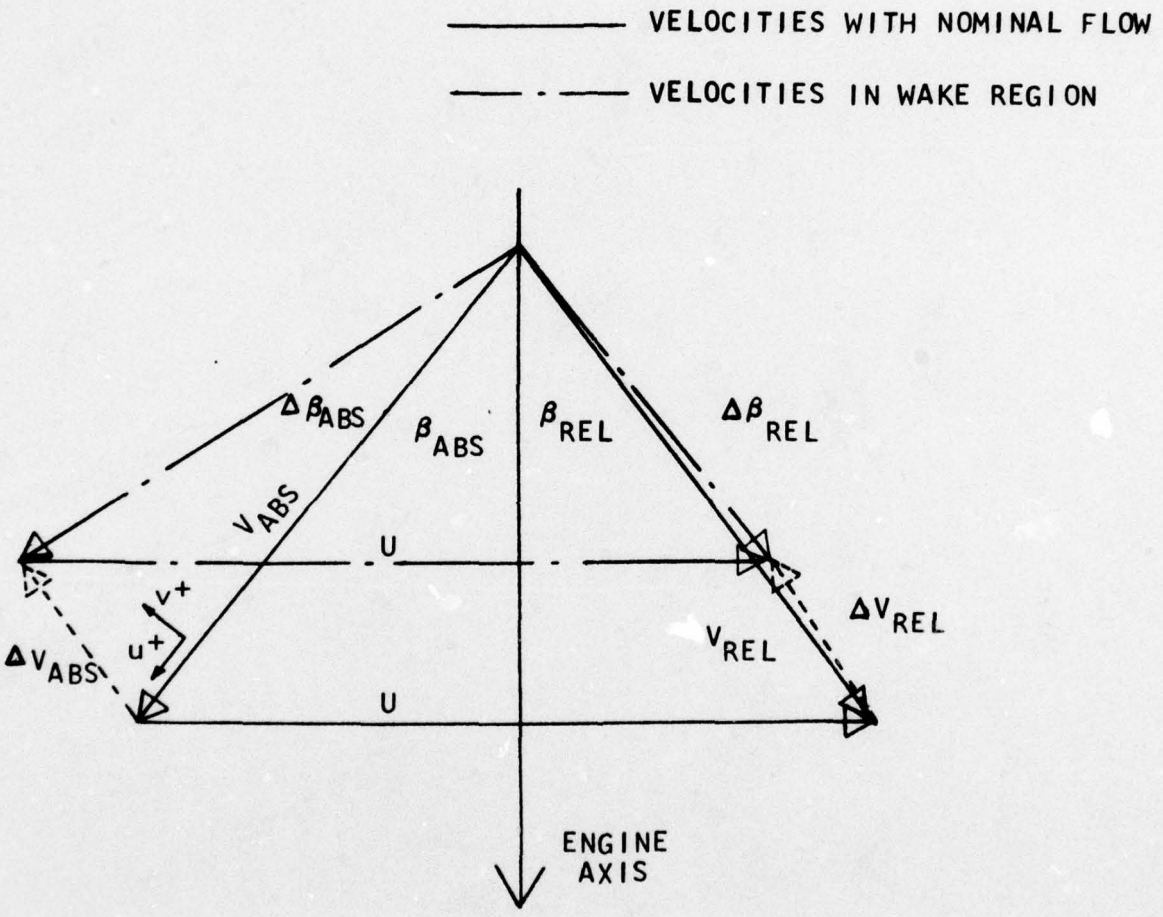

FIGURE 17. REDUCTION IN RELATIVE VELOCITY GENERATED BY BLADE WAKE CREATES CORRESPONDING VELOCITY AND ANGULAR CHANGE IN ABSOLUTE FRAME

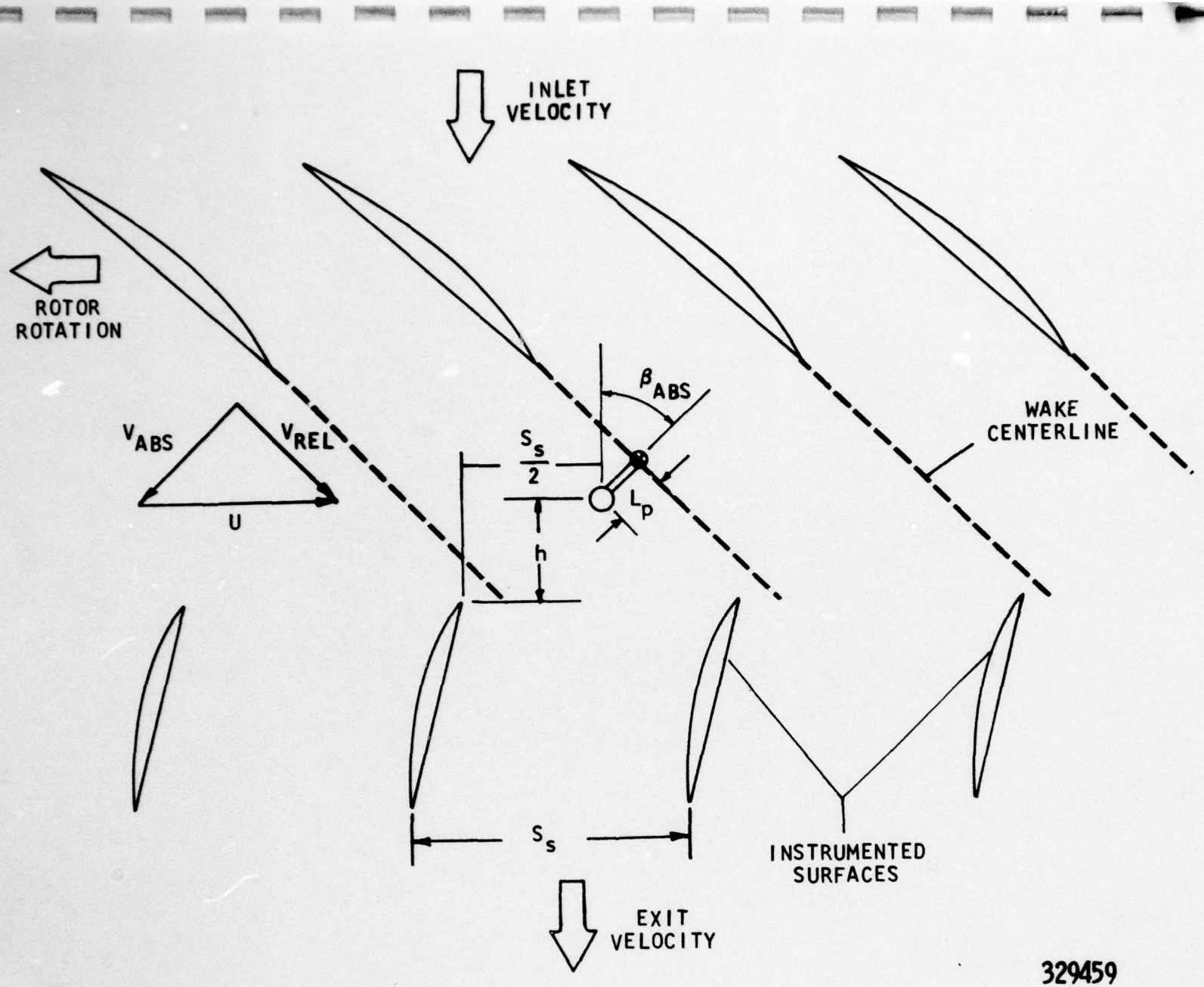

FIGURE 18. SCHEMATIC OF FLOW FIELD USED IN DYNAMIC DATA ANALYSIS

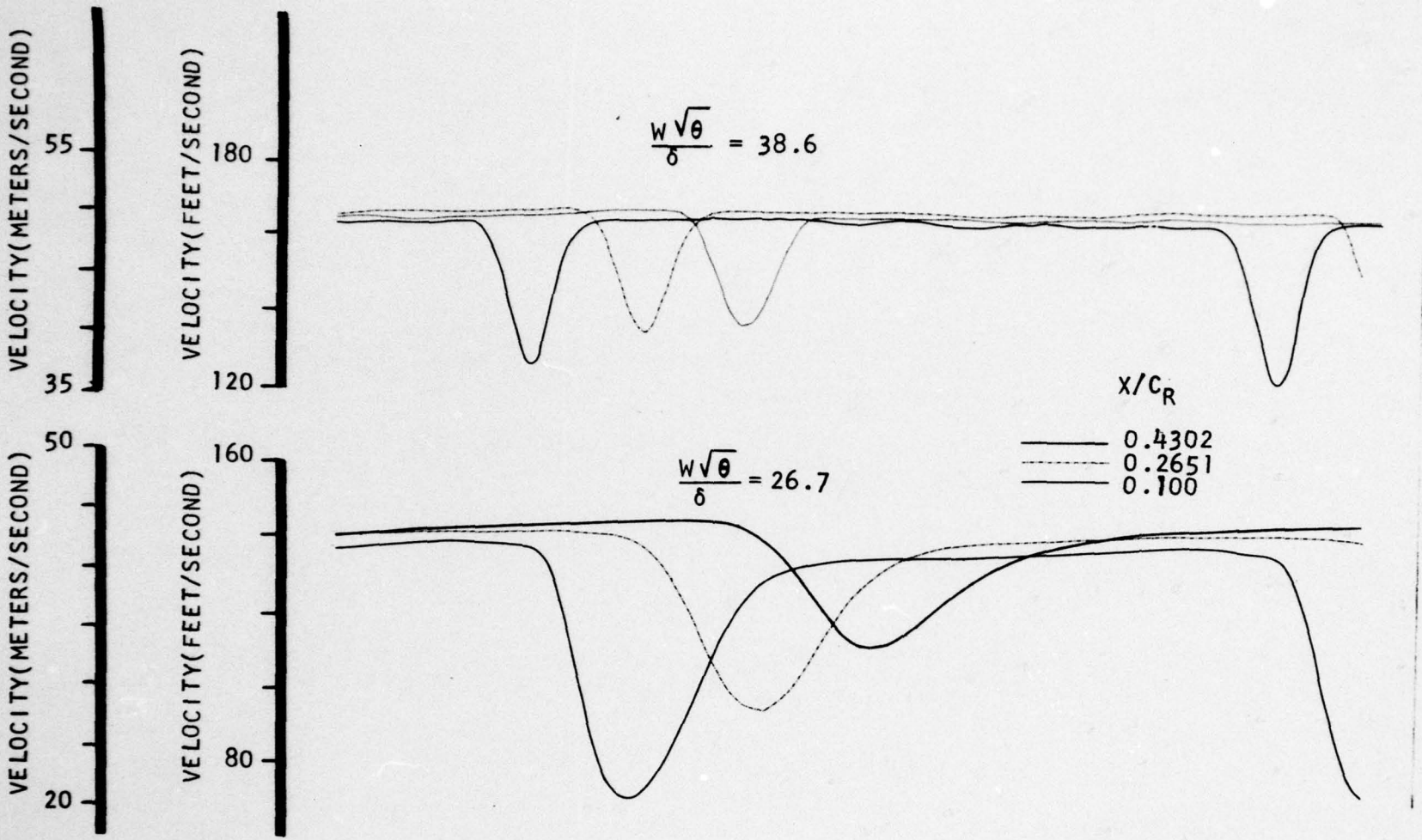

FIGURE 19. VARIATION OF THE ROTOR WAKE PROFILE WITH AXIAL DISTANCE FOR TWO LEVELS OF LOADING

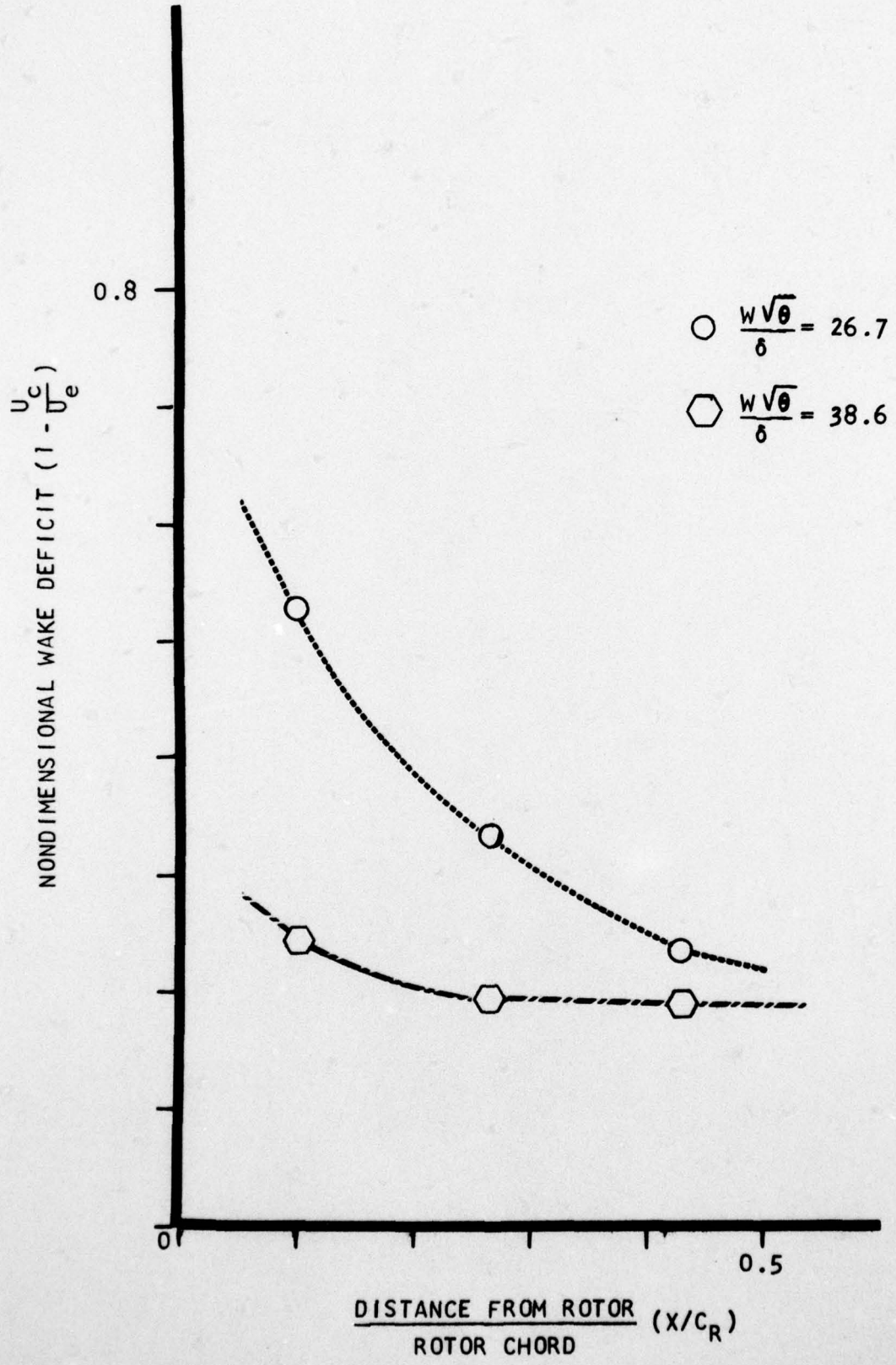

FIGURE 20. VARIATION OF ROTOR WAKE DEFICIT WITH AXIAL DISTANCE

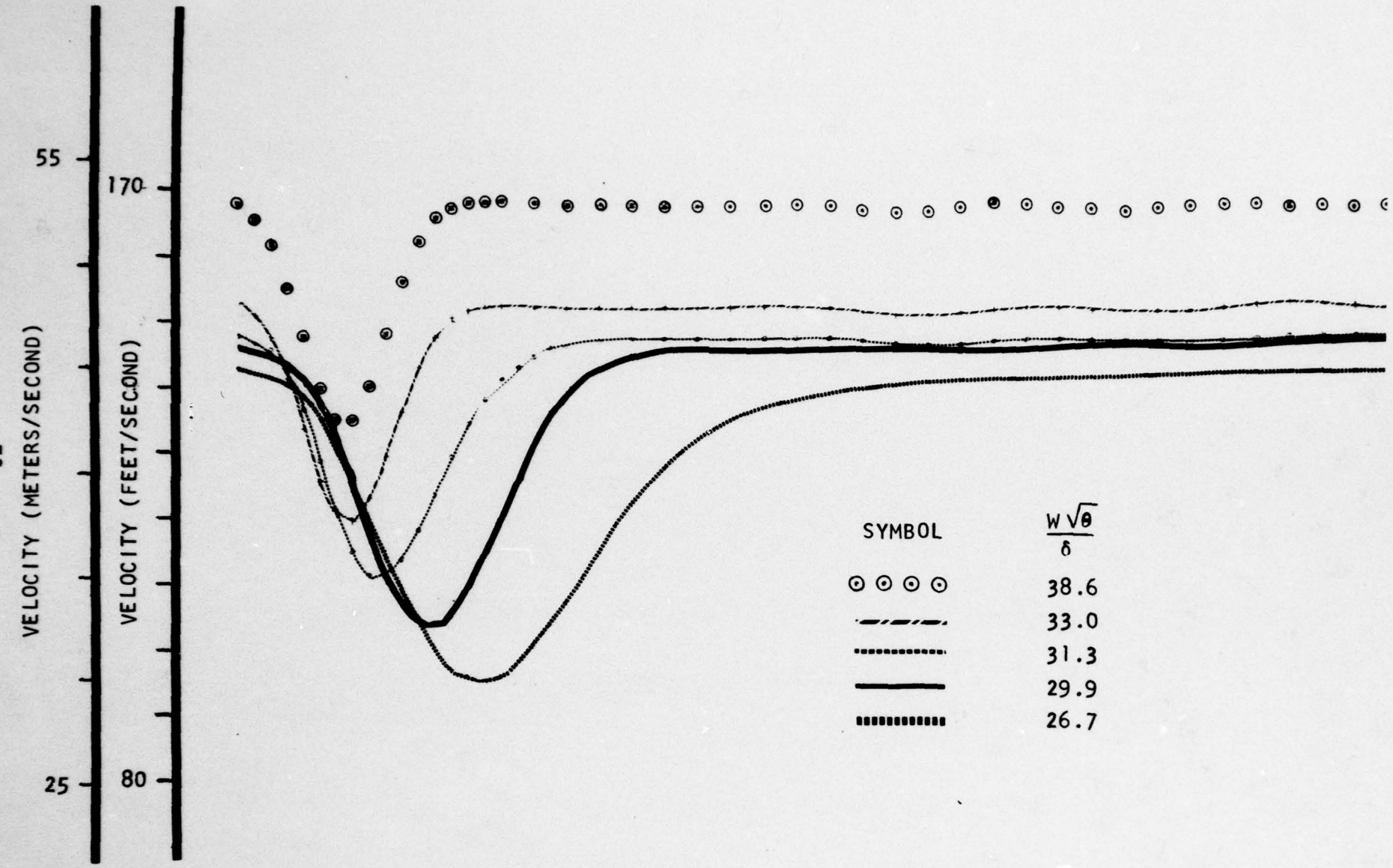

FIGURE 21. EFFECT OF LOADING ON THE ROTOR WAKE PROFILE

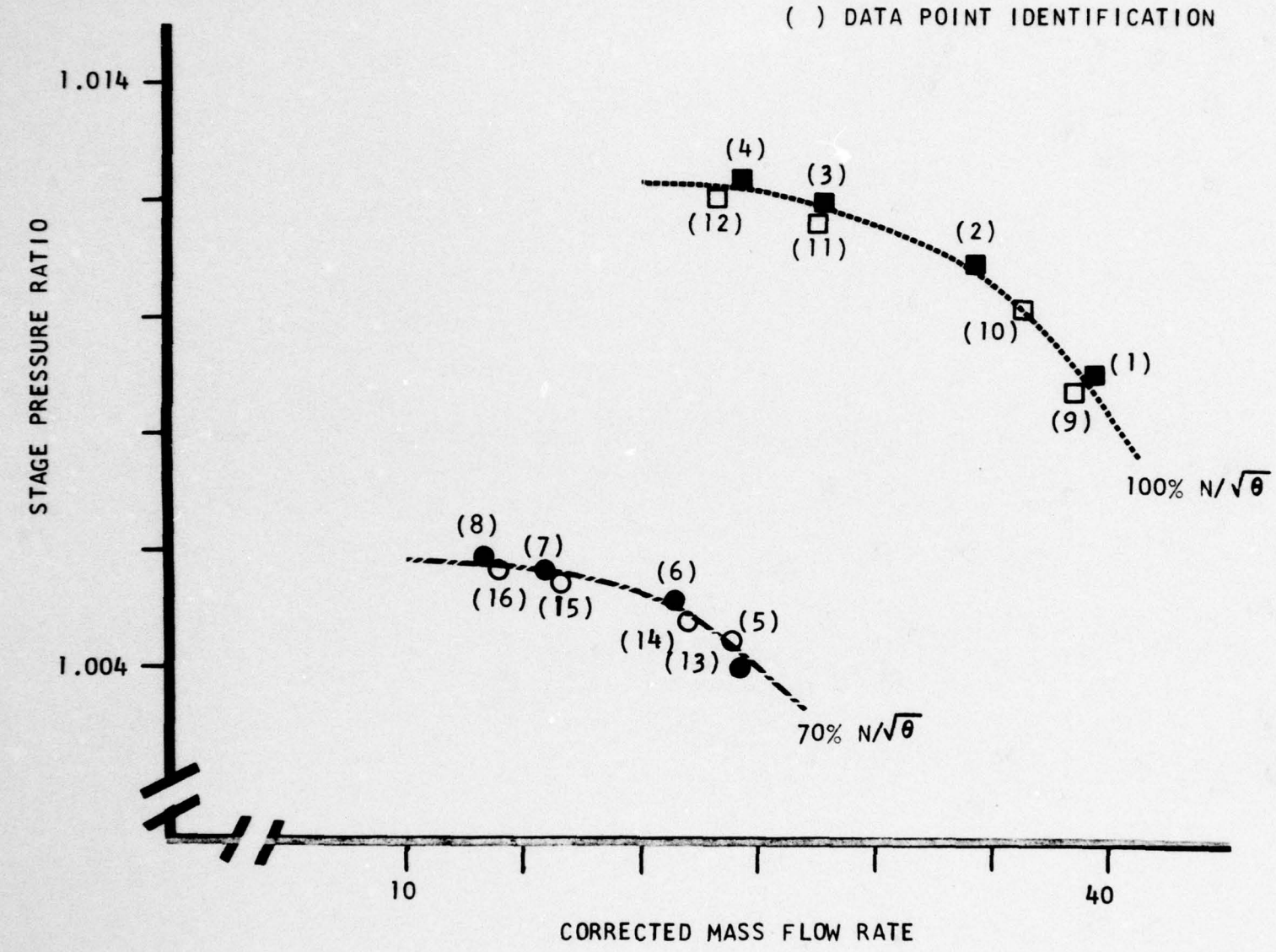

FIGURE 22. DATA POINT IDENTIFICATION IN TERMS OF PRESSURE RATIO AND MASS FLOW RATE

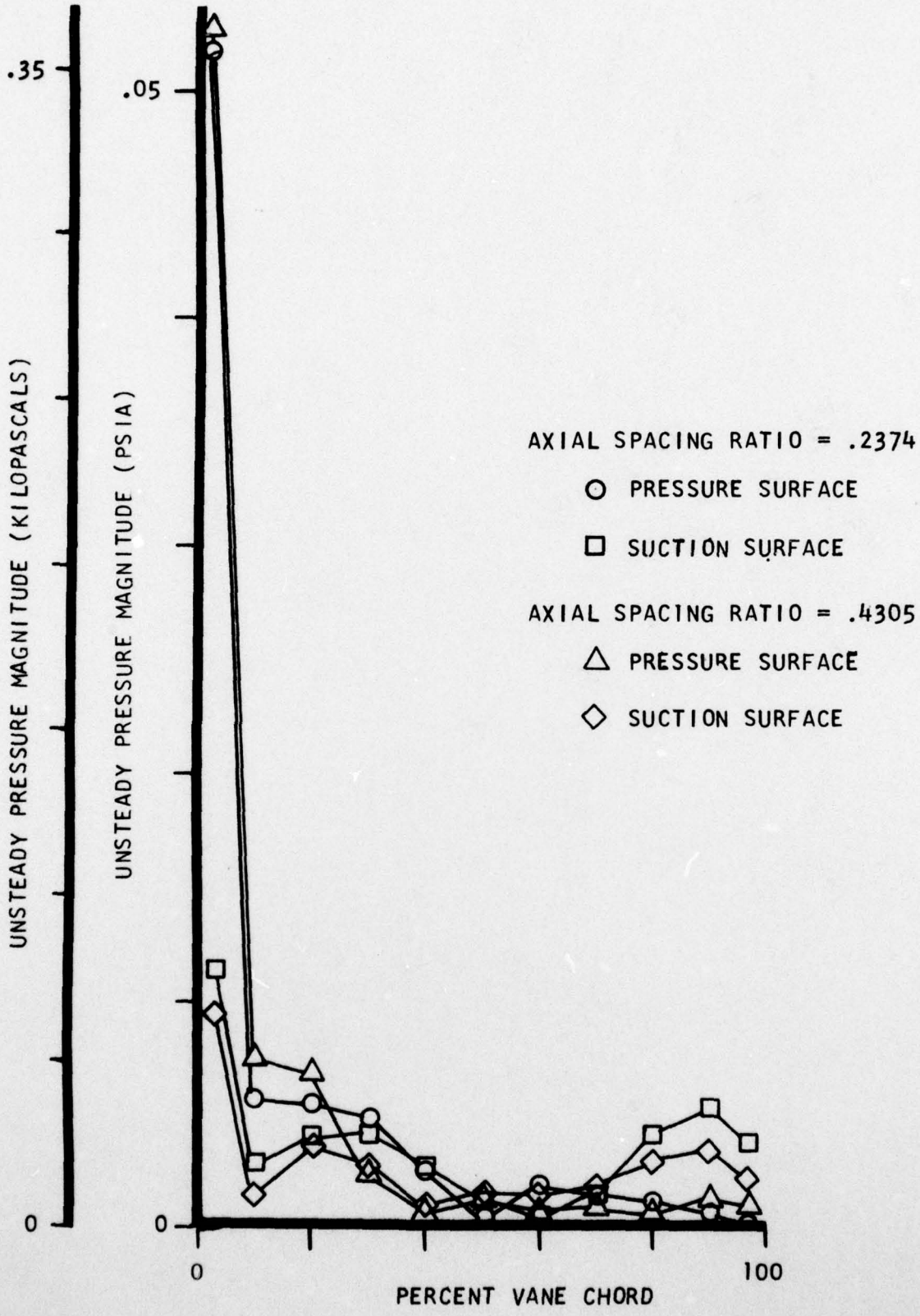

FIGURE 23. UNSTEADY PRESSURE MAGNITUDE ON THE VANE SURFACE FOR DATA POINTS 1 AND 9.

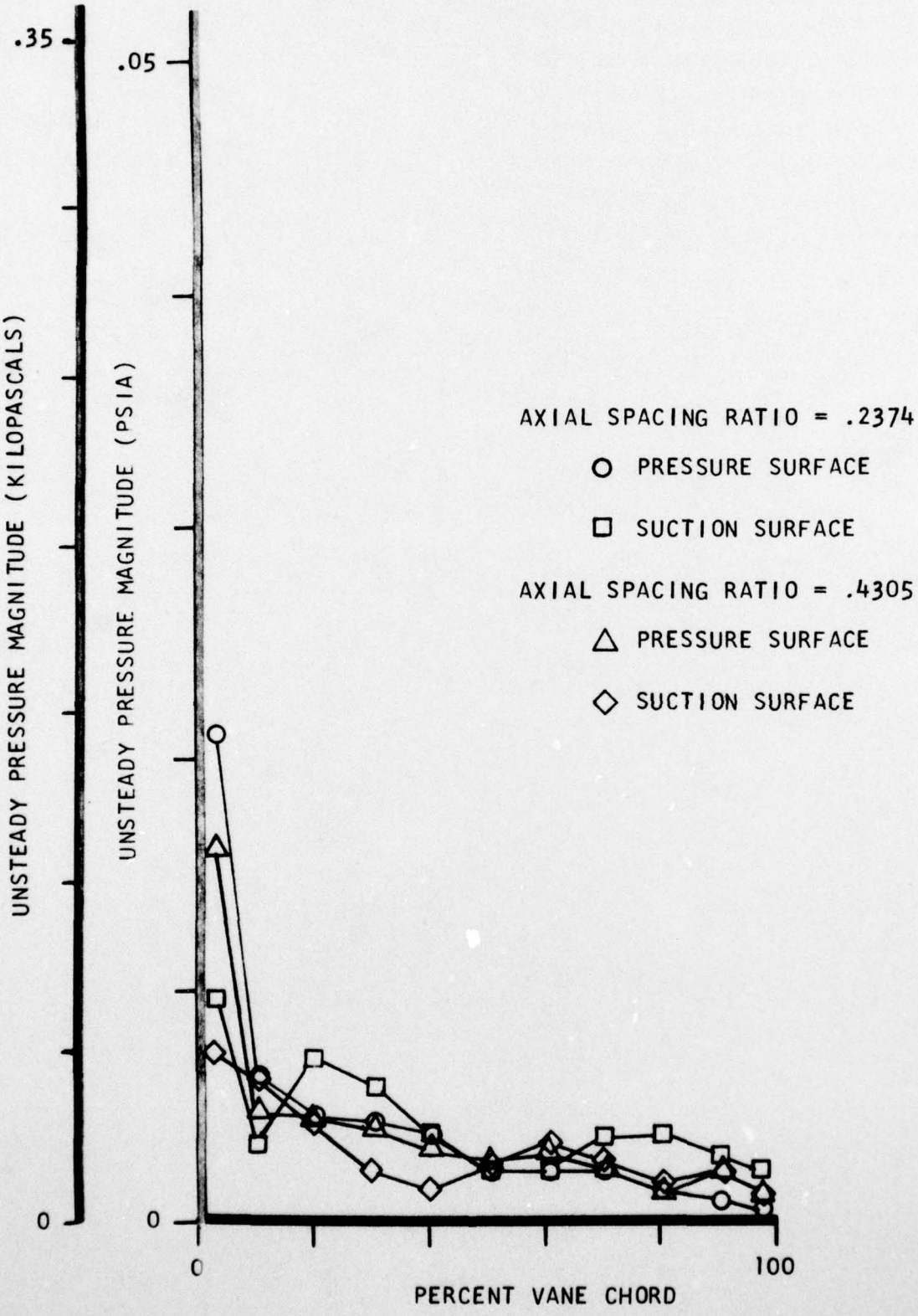

FIGURE 24. UNSTEADY PRESSURE MAGNITUDE ON THE VANE SURFACE FOR DATA POINTS 2 AND 10.

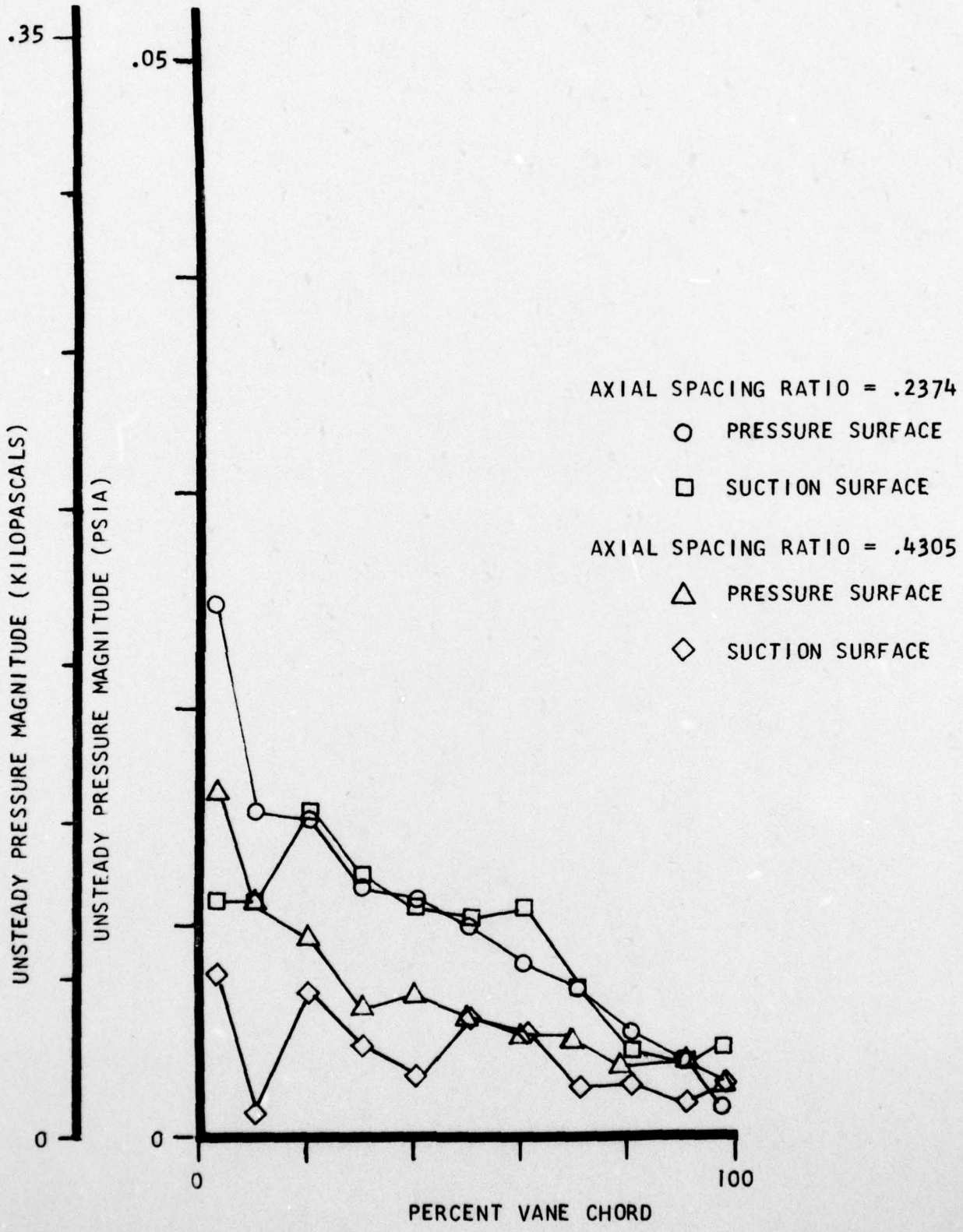

FIGURE 25. UNSTEADY PRESSURE MAGNITUDE ON THE VANE SURFACE FOR DATA POINTS 3 AND 11.

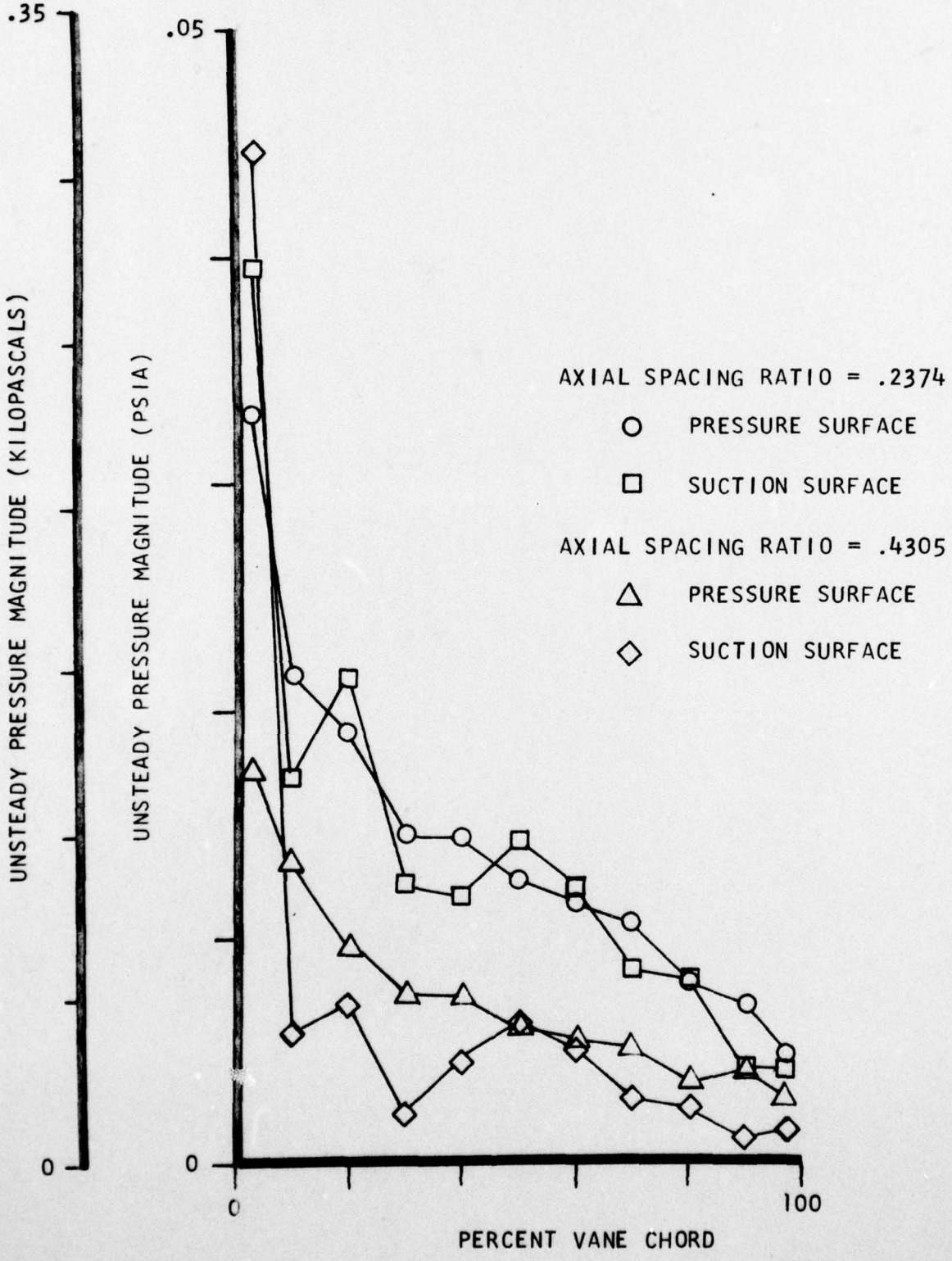

FIGURE 26. UNSTEADY PRESSURE MAGNITUDE ON THE VANE SURFACE FOR DATA POINTS 4 AND 12.

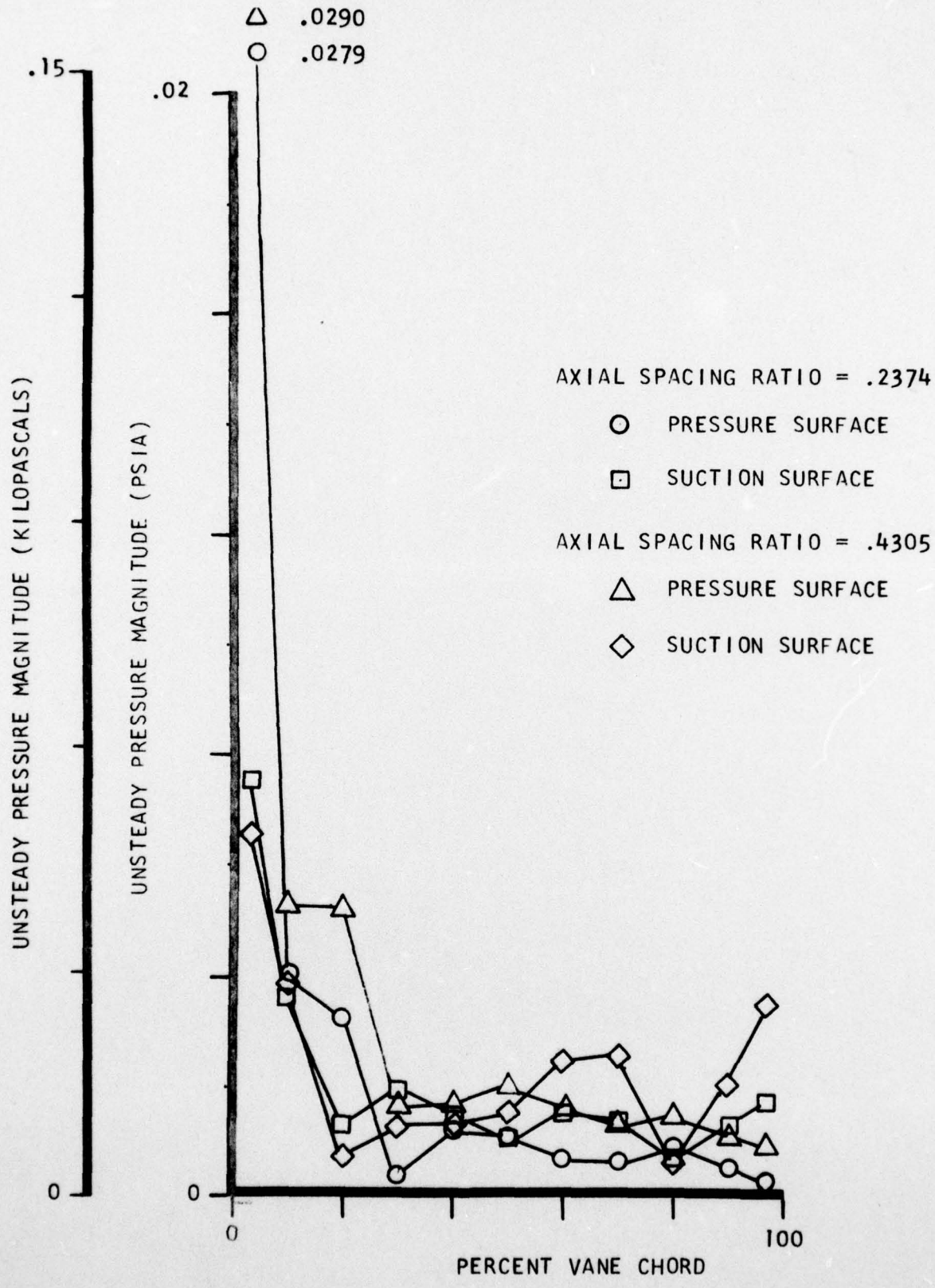

FIGURE 27. UNSTEADY PRESSURE MAGNITUDE ON THE VANE SURFACE FOR DATA POINTS 5 AND 13.

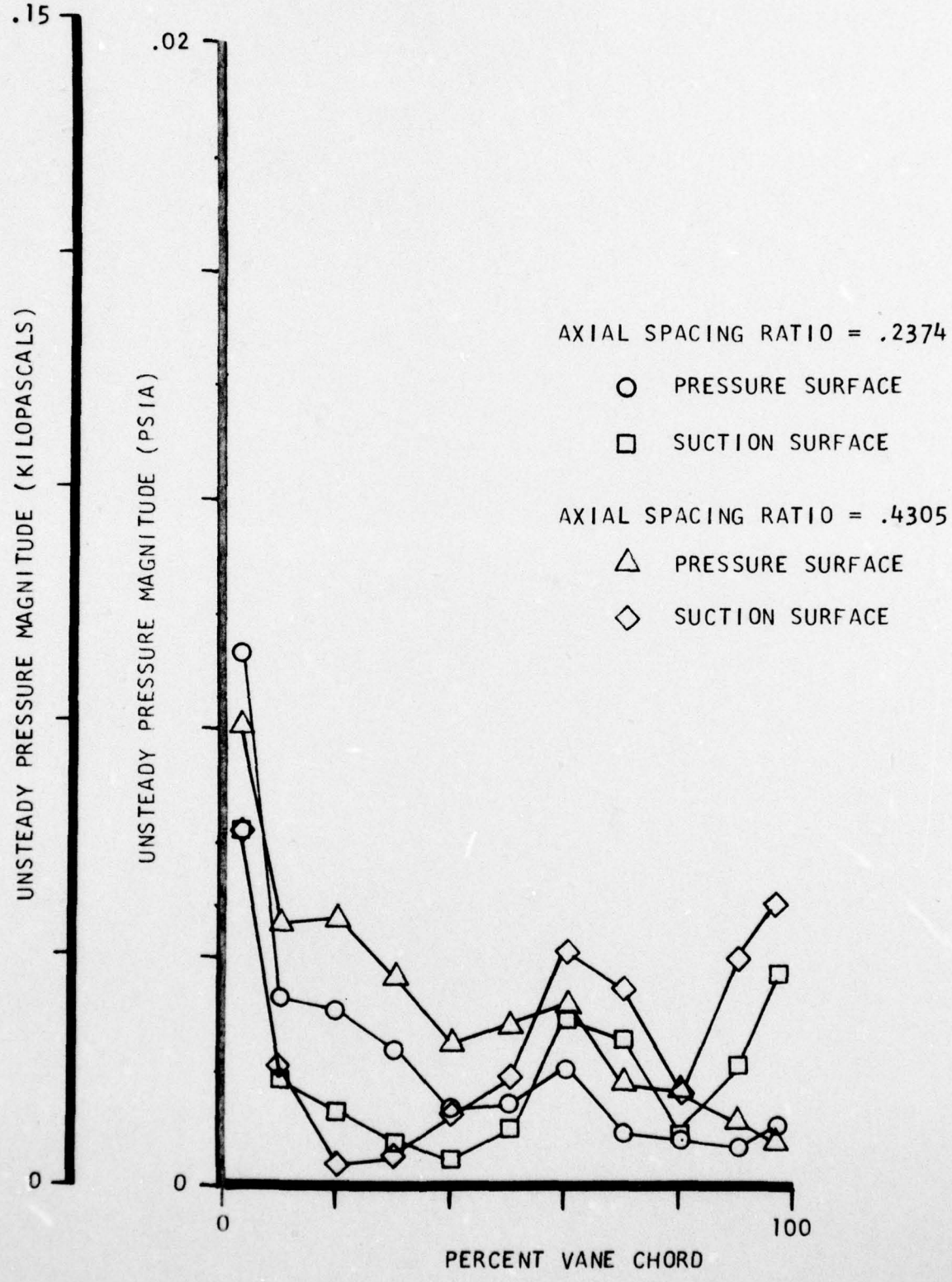

FIGURE 28. UNSTEADY PRESSURE MAGNITUDE ON THE VANE SURFACE FOR DATA POINTS 6 AND 14.

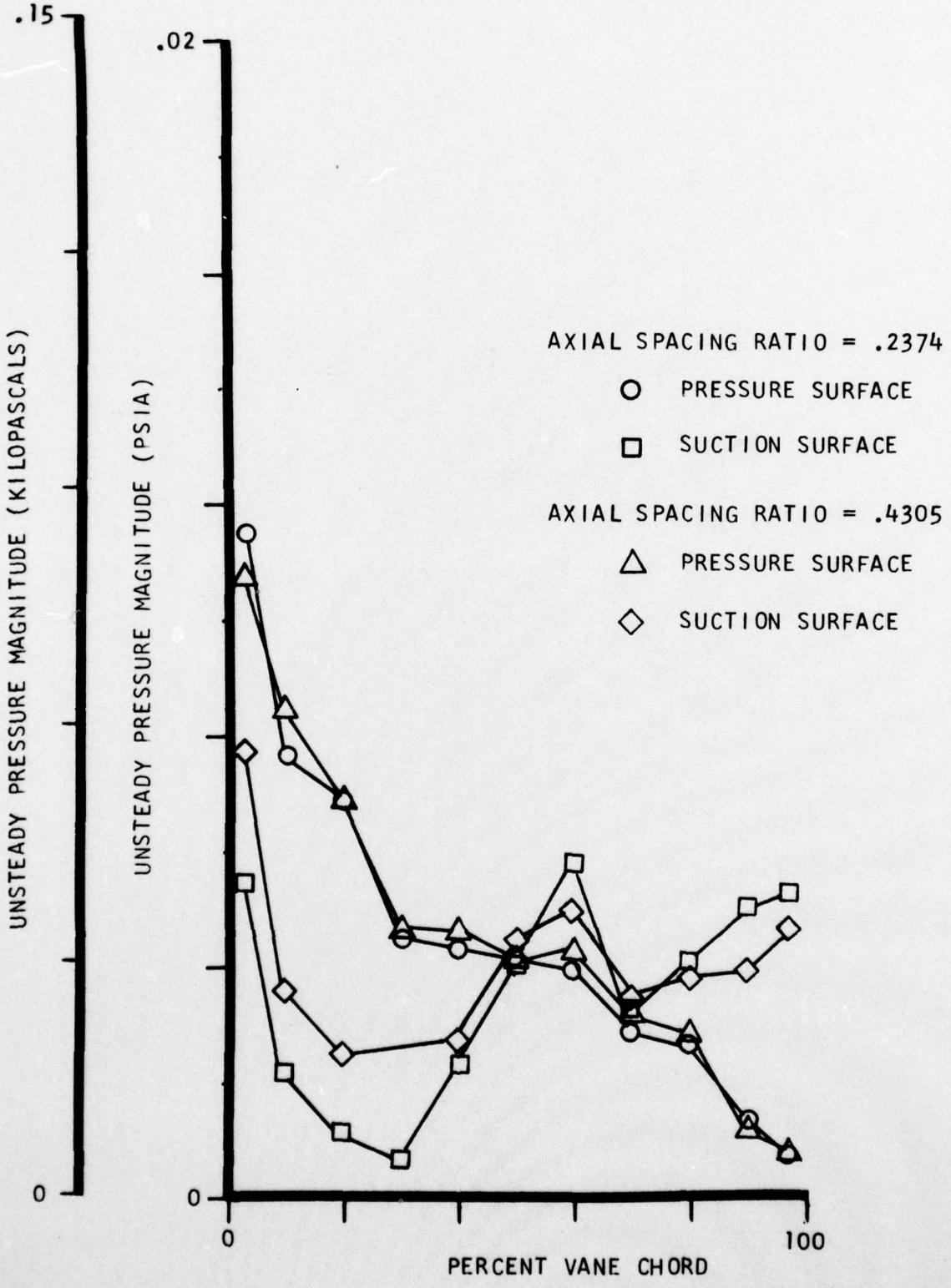

FIGURE 29. UNSTEADY PRFSSURE MAGNITUDE ON THE VANE SURFACE FOR DATA POINTS 7 AND 15.

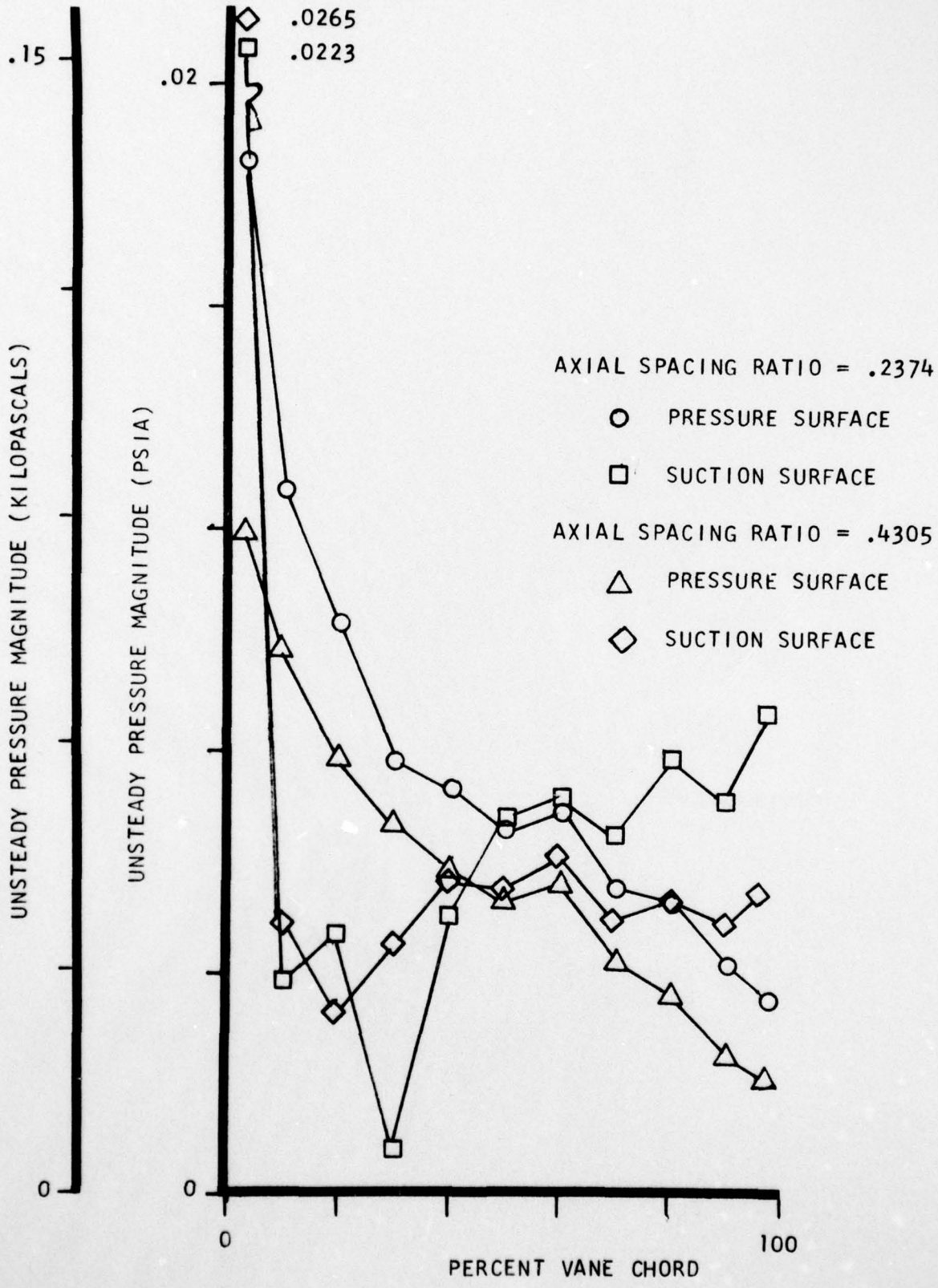

FIGURE 30. UNSTEADY PRESSURE MAGNITUDE ON THE VANE SURFACE FOR DATA POINTS 8 AND 16.

AD-A050 648 GENERAL MOTORS CORP INDIANAPOLIS IND DETROIT DIESEL --ETC F/G 21/5
THE EFFECT OF ROTOR-STATOR AXIAL SPACING ON THE TIME-VARIANT AE--ETC(U)
DEC 77 S FLEETER, R L JAY, W A BENNETT F49620-77-C-0024
UNCLASSIFIED DDA-EDR-9379 AFOSR-TR-78-0165 NL

2 OF 2
AD
AD50648

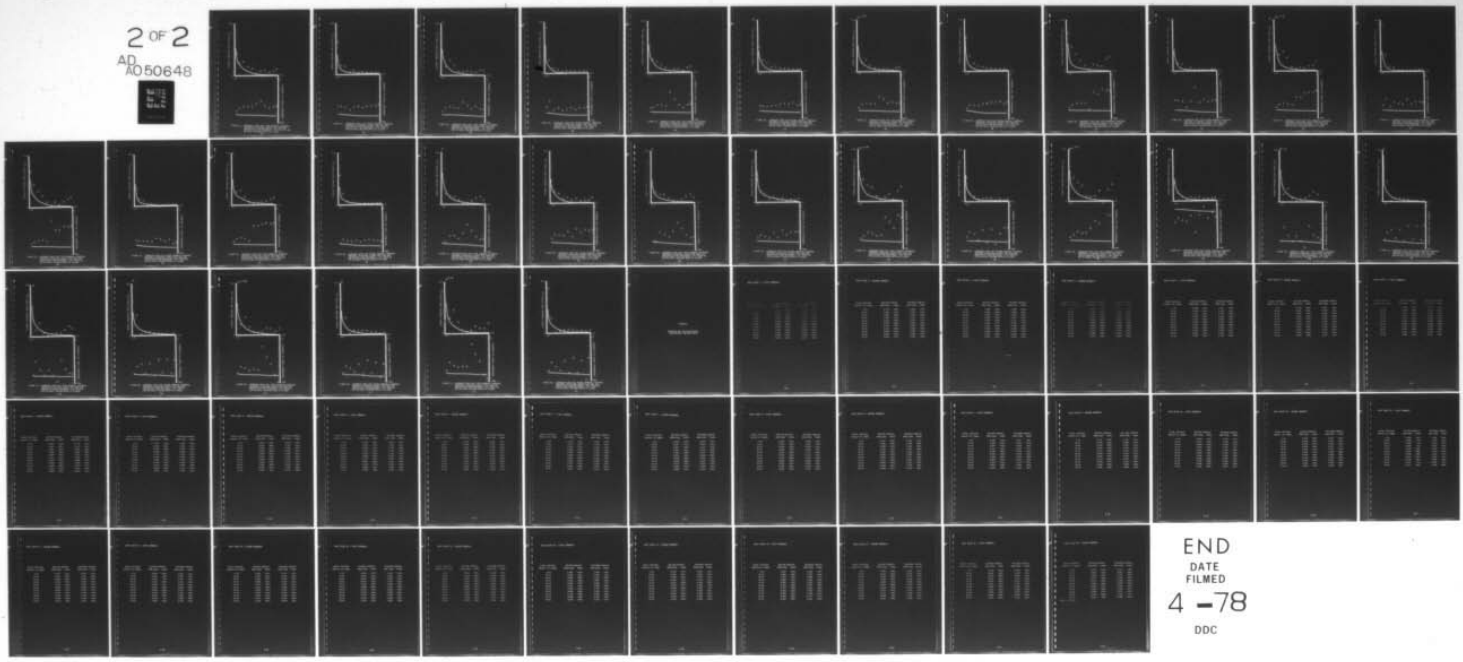

END
DATE
FILMED
4 -78
DDC

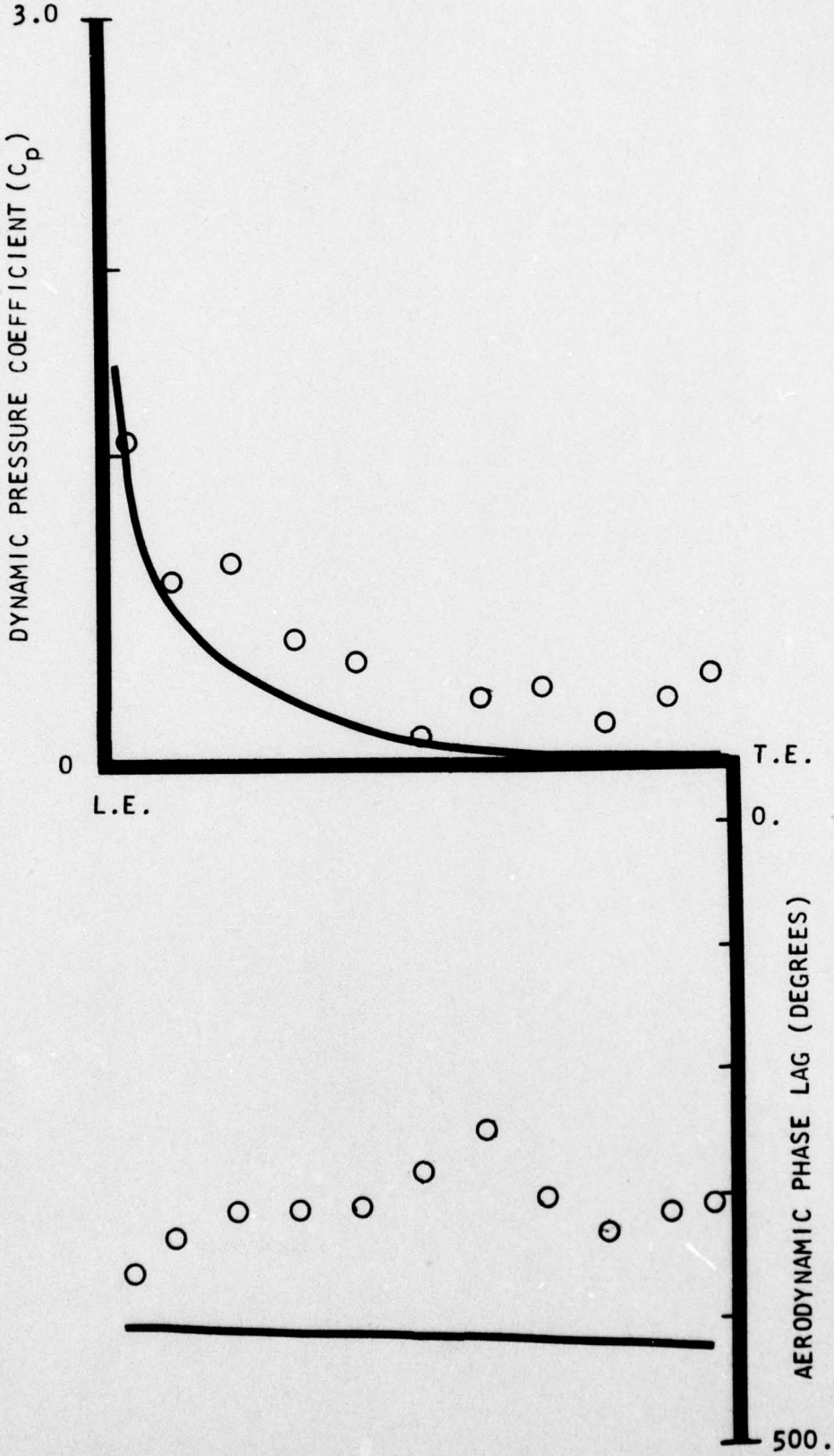

FIGURE 31. CHORDWISE DATA FOR FIRST HARMONIC UNSTEADY PRESSURE DIFFERENCE ACROSS THE VANE AND PREDICTION FROM REFERENCE 7 FOR POINT 3 FOR AN AXIAL SPACING RATIO OF 0.2374

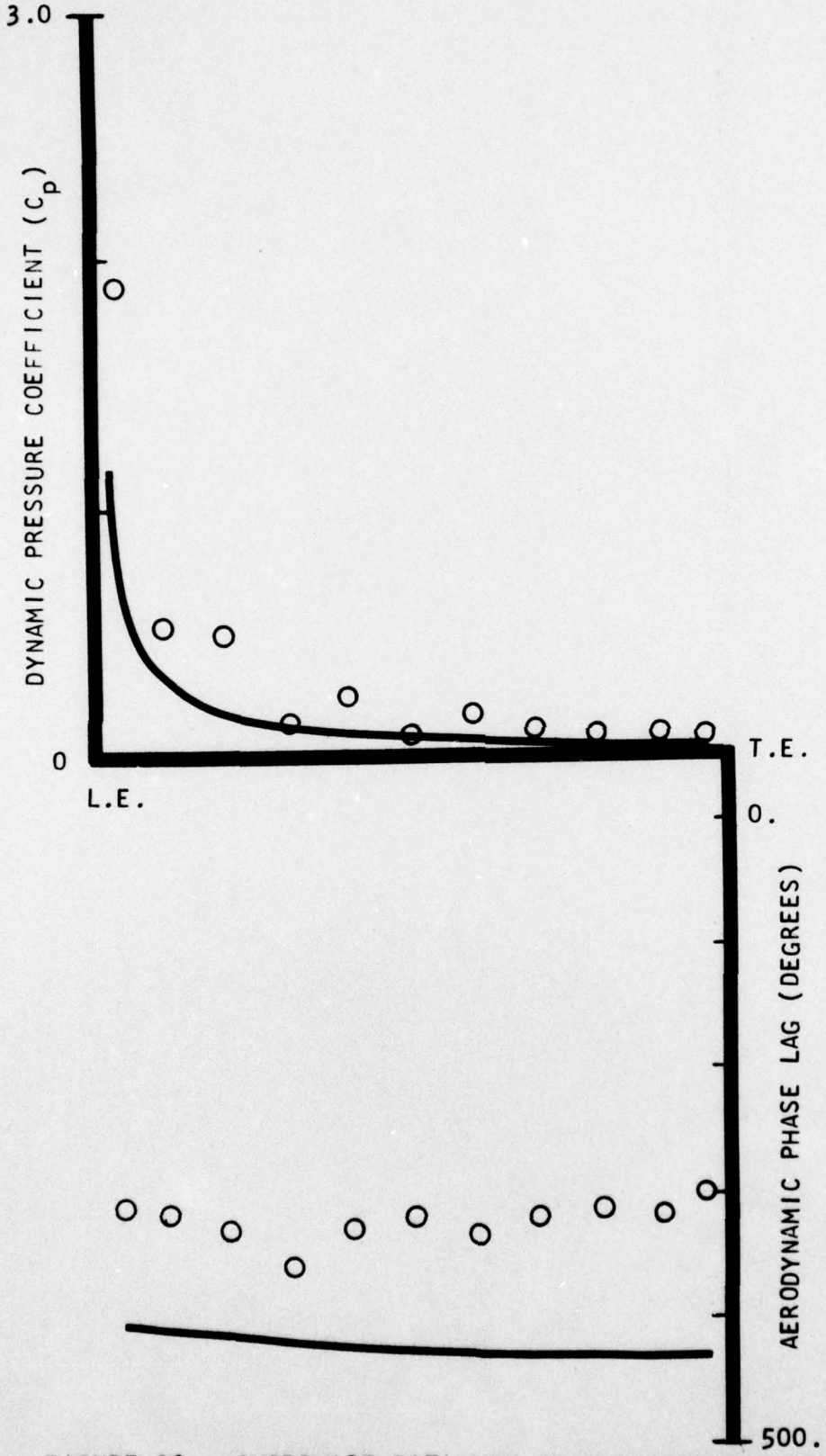

FIGURE 32. CHORDWISE DATA FOR SECOND HARMONIC UNSTEADY PRESSURE DIFFERENCE ACROSS THE VANE AND PREDICTION FROM REFERENCE 7 FOR POINT 3 FOR AN AXIAL SPACING RATIO OF 0.2374

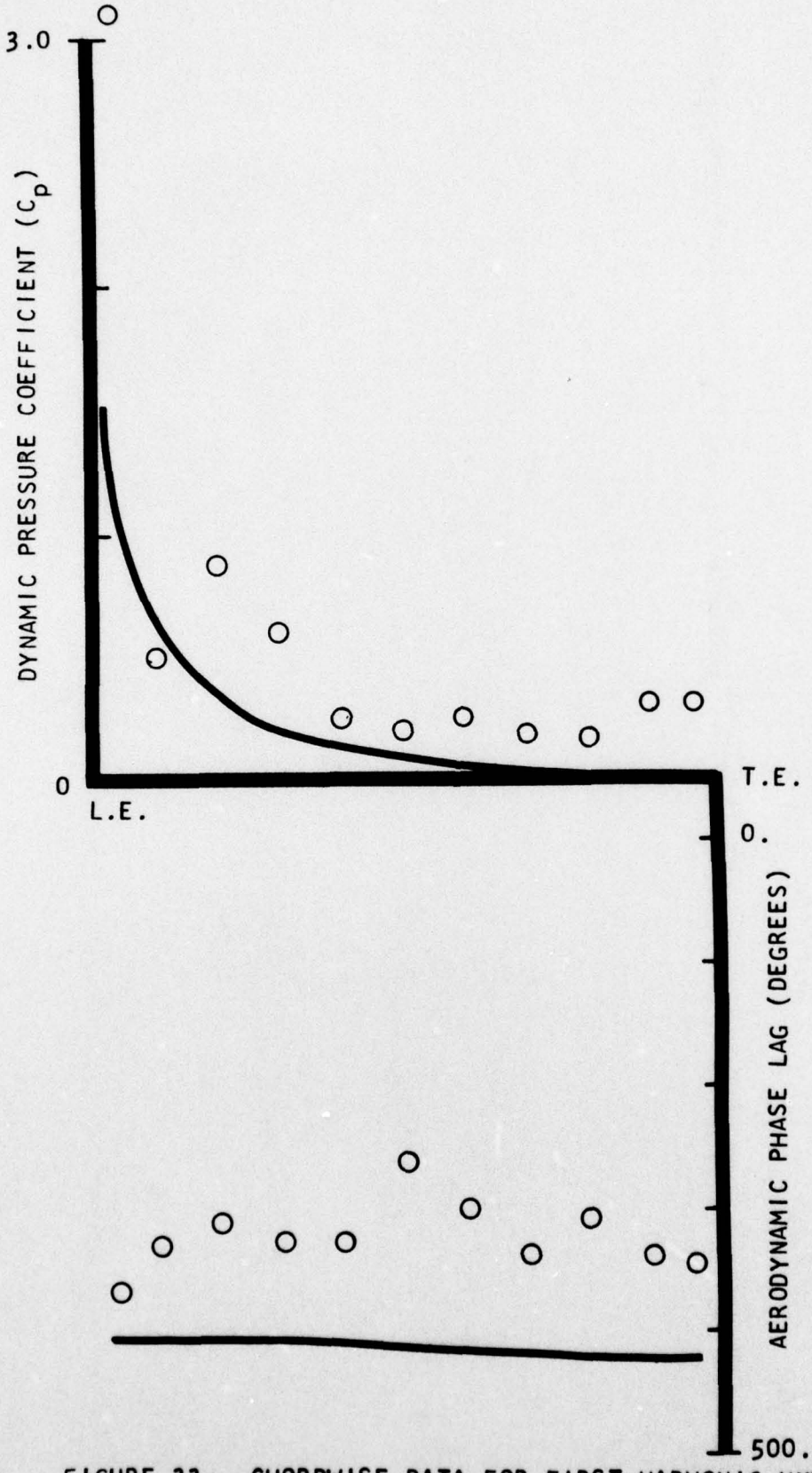

FIGURE 33. CHORDWISE DATA FOR FIRST HARMONIC UNSTEADY PRESSURE DIFFERENCE ACROSS THE VANE AND PREDICTION FROM REFERENCE 7 FOR POINT 4 FOR AN AXIAL SPACING RATIO OF 0.2374

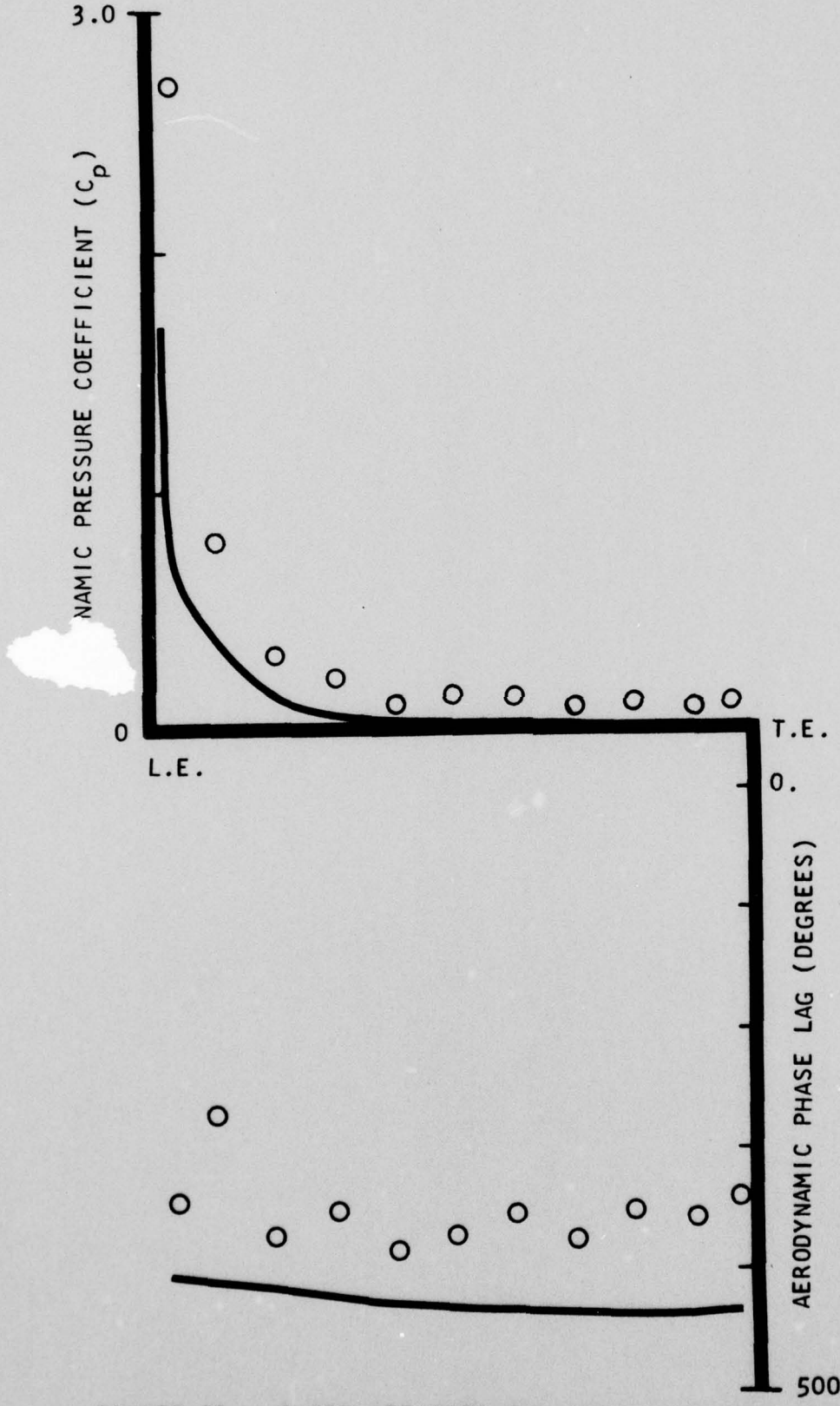

FIGURE 34. CHORDWISE DATA FOR SECOND HARMONIC UNSTEADY PRESSURE DIFFERENCE ACROSS THE VANE AND PREDICTION FROM REFERENCE 7 FOR POINT 4 FOR AN AXIAL SPACING RATIO OF 0.2374

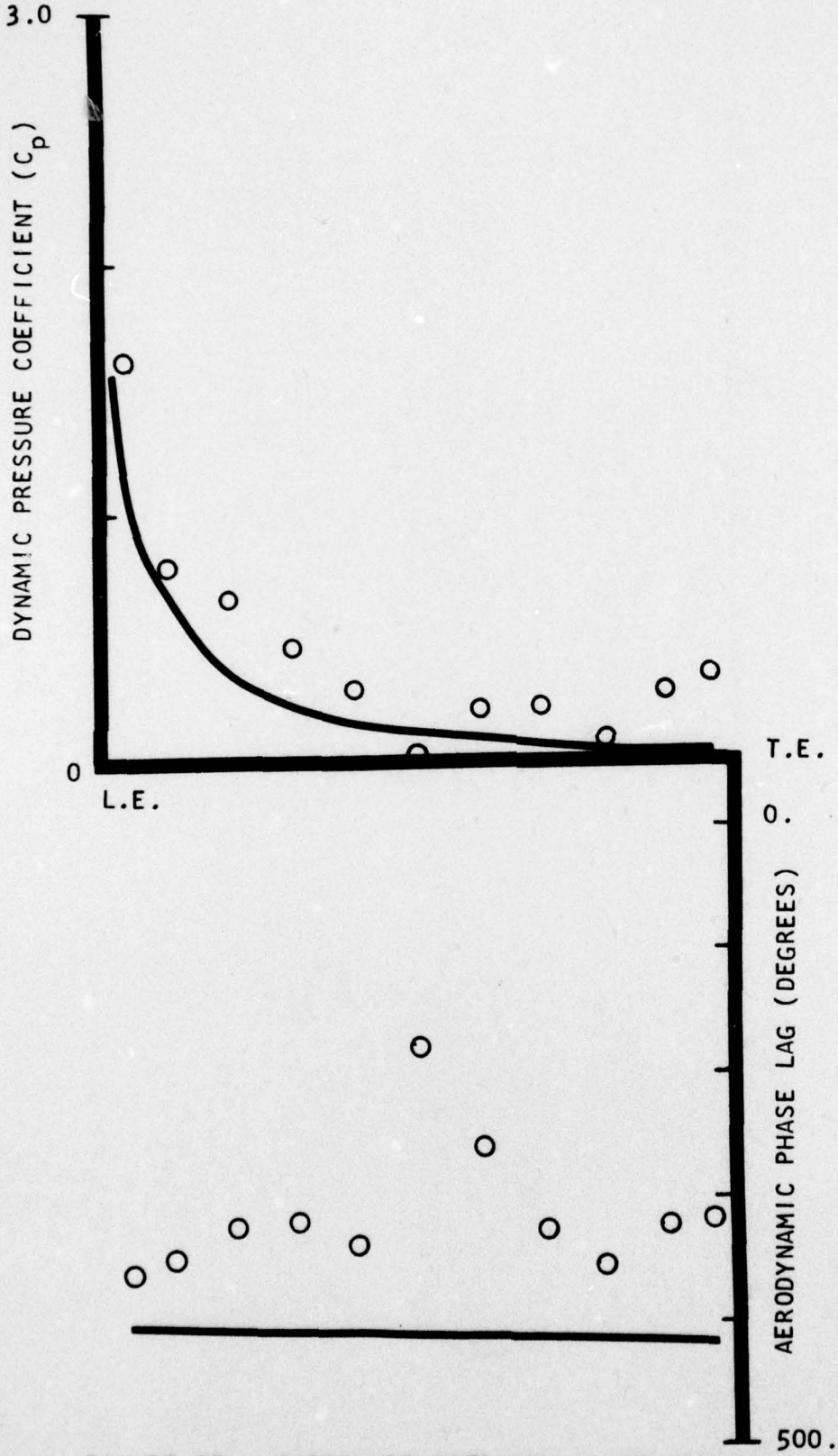

FIGURE 35. CHORDWISE DATA FOR FIRST HARMONIC UNSTEADY PRESSURE DIFFERENCE ACROSS THE VANE AND PREDICTION FROM REFERENCE 7 FOR POINT 11 FOR AN AXIAL SPACING RATIO OF 0.4305

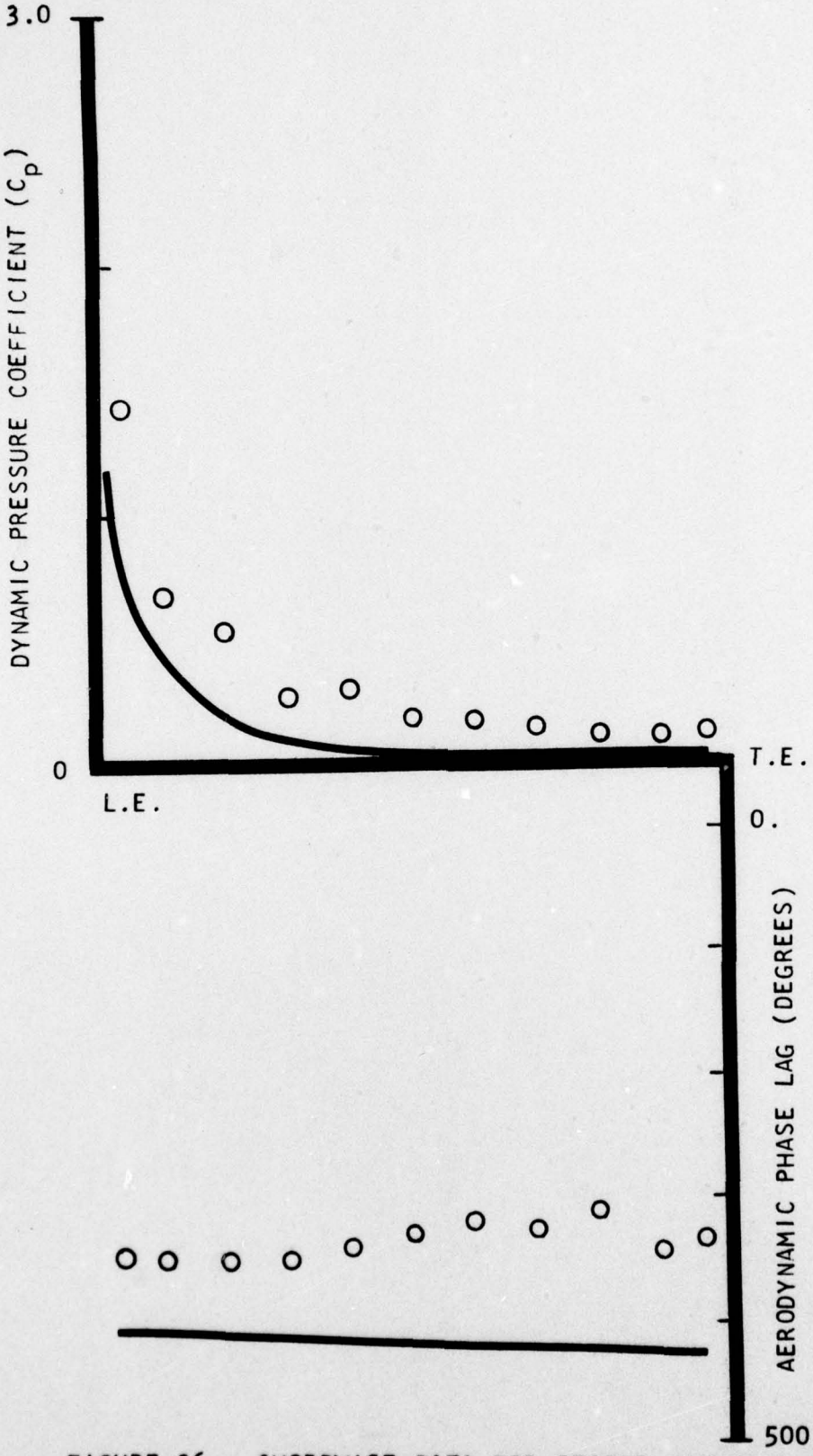

FIGURE 36. CHORDWISE DATA FOR SECOND HARMONIC UNSTEADY PRESSURE DIFFERENCE ACROSS THE VANE AND PREDICTION FROM REFERENCE 7 FOR POINT 11 FOR AN AXIAL SPACING RATIO OF 0.4305

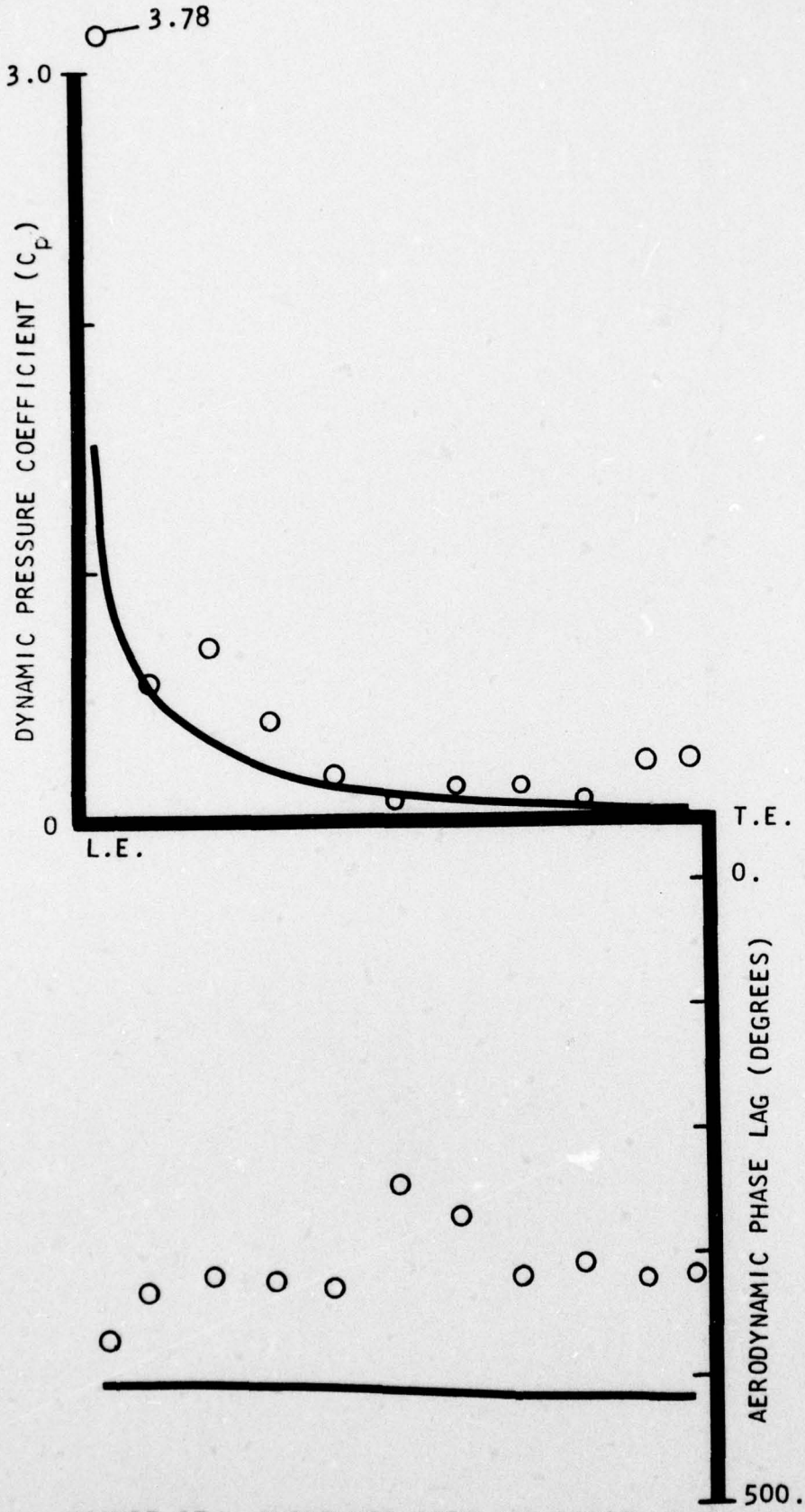

FIGURE 37. CHORDWISE DATA FOR FIRST HARMONIC UNSTEADY PRESSURE DIFFERENCE ACROSS THE VANE AND PREDICTION FROM REFERENCE 7 FOR POINT 12 FOR AN AXIAL SPACING RATIO OF 0.4305

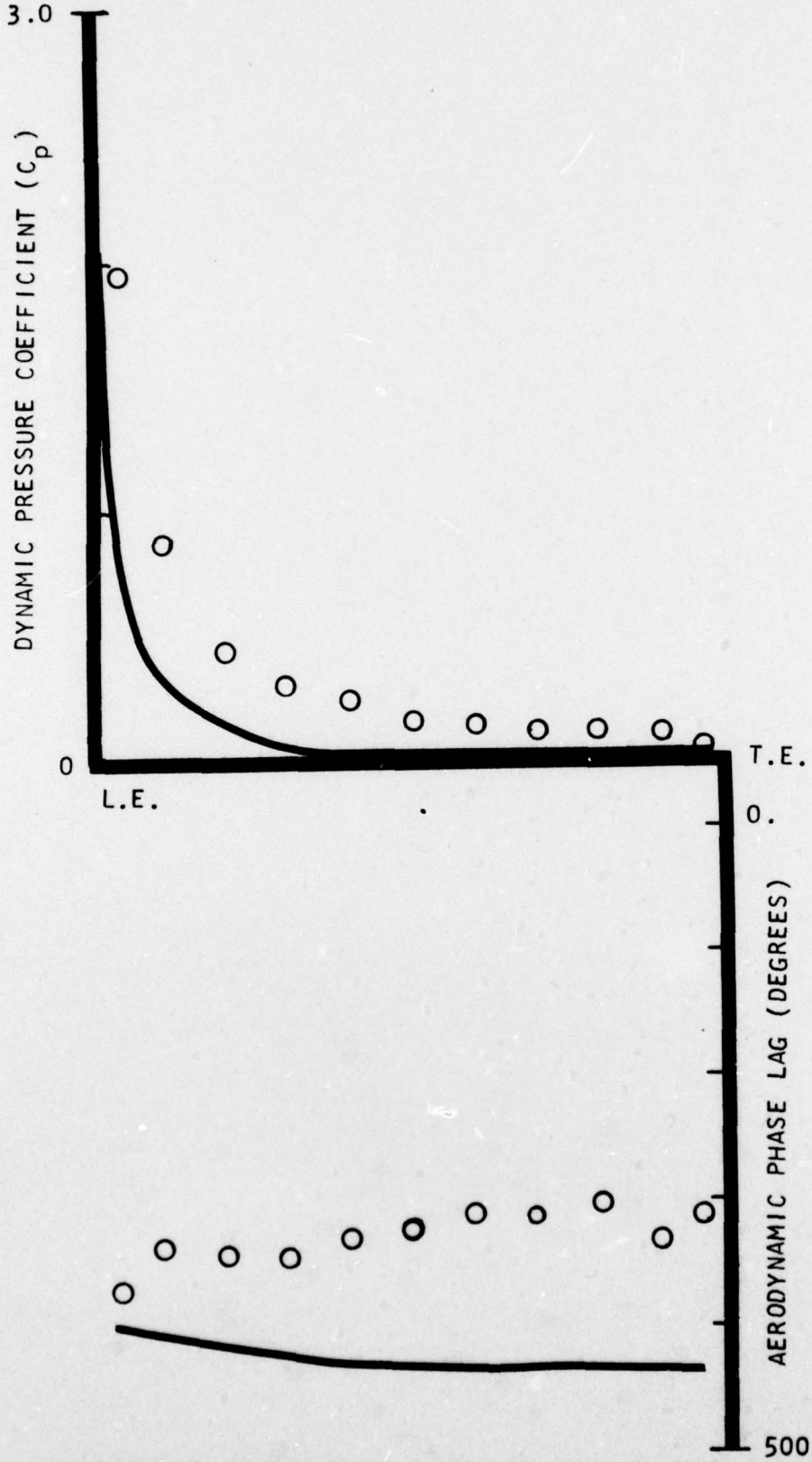

FIGURE 38. CHORDWISE DATA FOR SECOND HARMONIC UNSTEADY PRESSURE DIFFERENCE ACROSS THE VANE AND PREDICTION FROM REFERENCE 7 FOR POINT 12 FOR AN AXIAL SPACING RATIO OF 0.4305

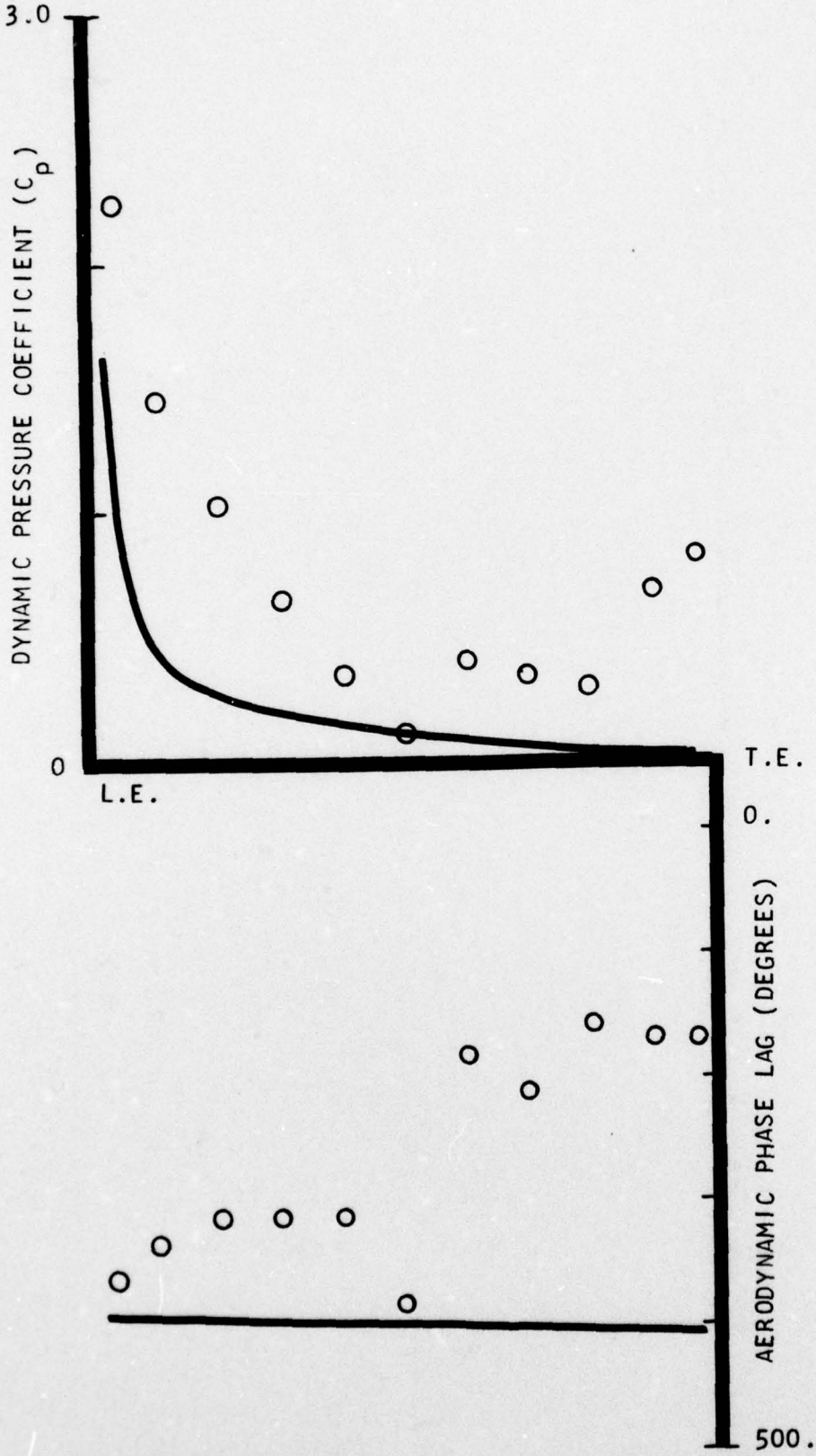

FIGURE 39. CHORDWISE DATA FOR FIRST HARMONIC UNSTEADY PRESSURE DIFFERENCE ACROSS THE VANE AND PREDICTION FROM REFERENCE 7 FOR POINT 7 FOR AN AXIAL SPACING RATIO OF 0.2374

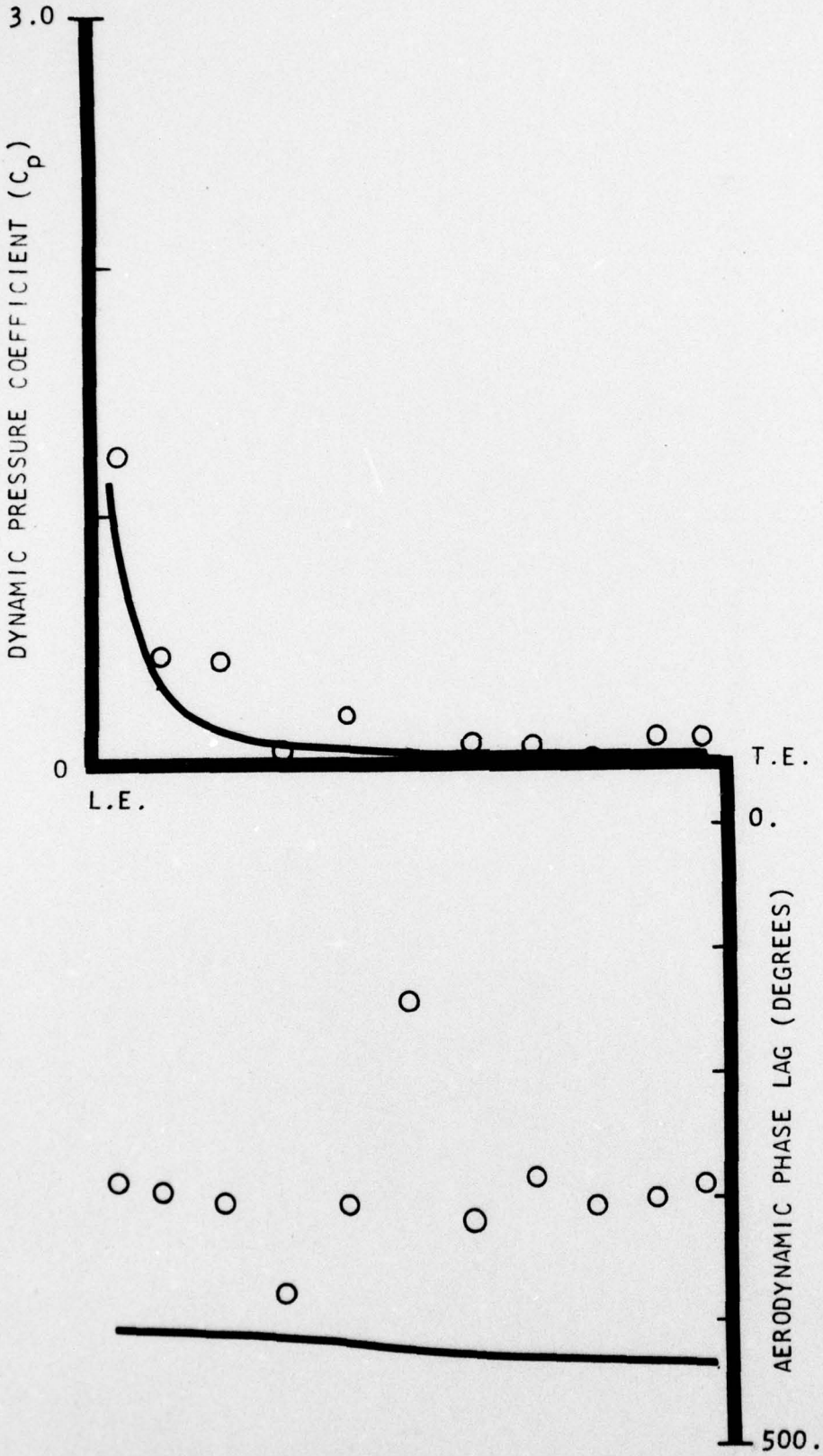

FIGURE 40. CHORDWISE DATA FOR SECOND HARMONIC UNSTEADY PRESSURE DIFFERENCE ACROSS THE VANE AND PREDICTION FROM REFERENCE 7 FOR POINT 7 FOR AN AXIAL SPACING RATIO OF 0.2374

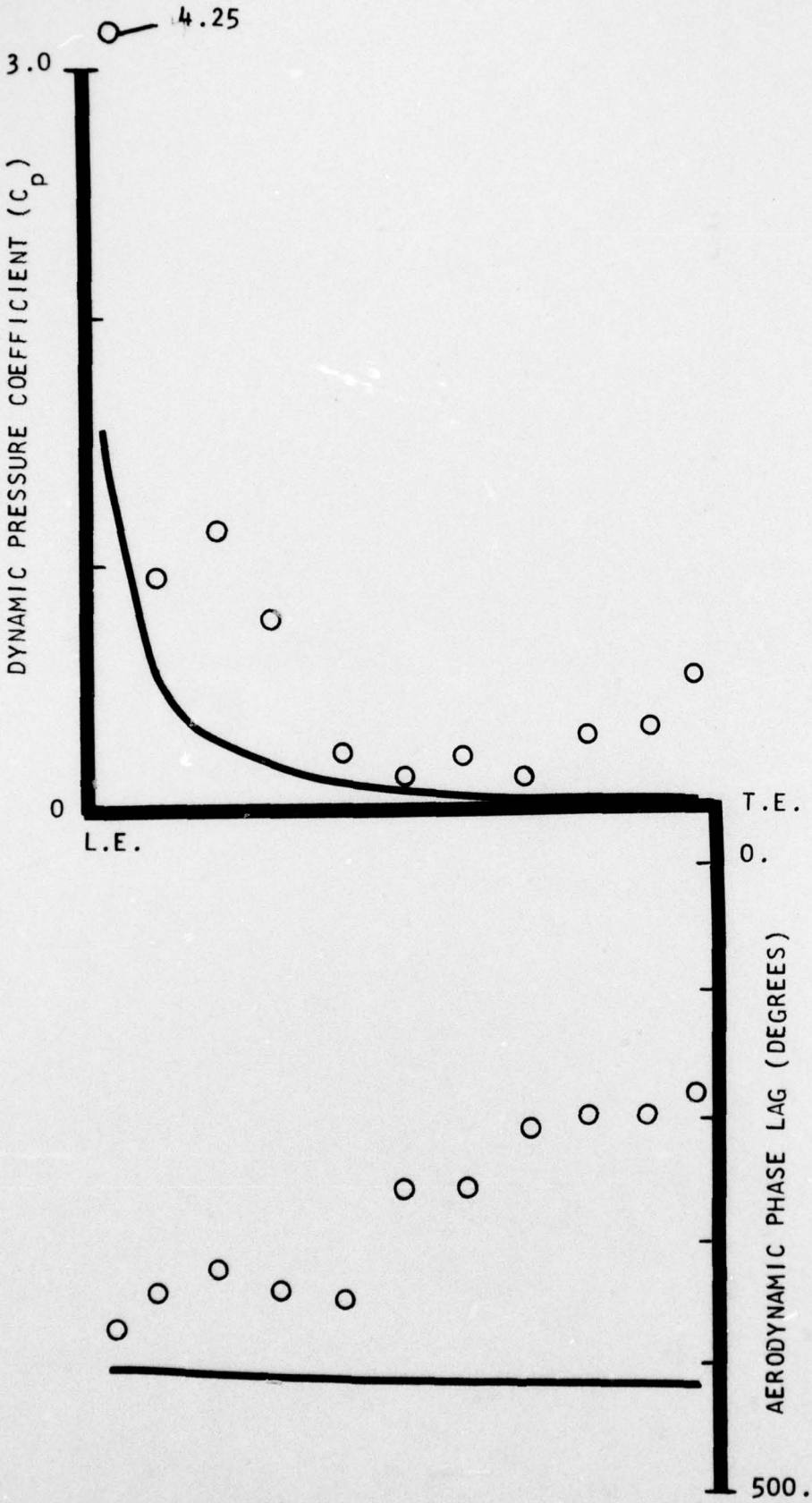

FIGURE 41. CHORDWISE DATA FOR FIRST HARMONIC UNSTEADY PRESSURE DIFFERENCE ACROSS THE VANE AND PREDICTION FROM REFERENCE 7 FOR POINT 8 FOR AN AXIAL SPACING RATIO OF 0.2374

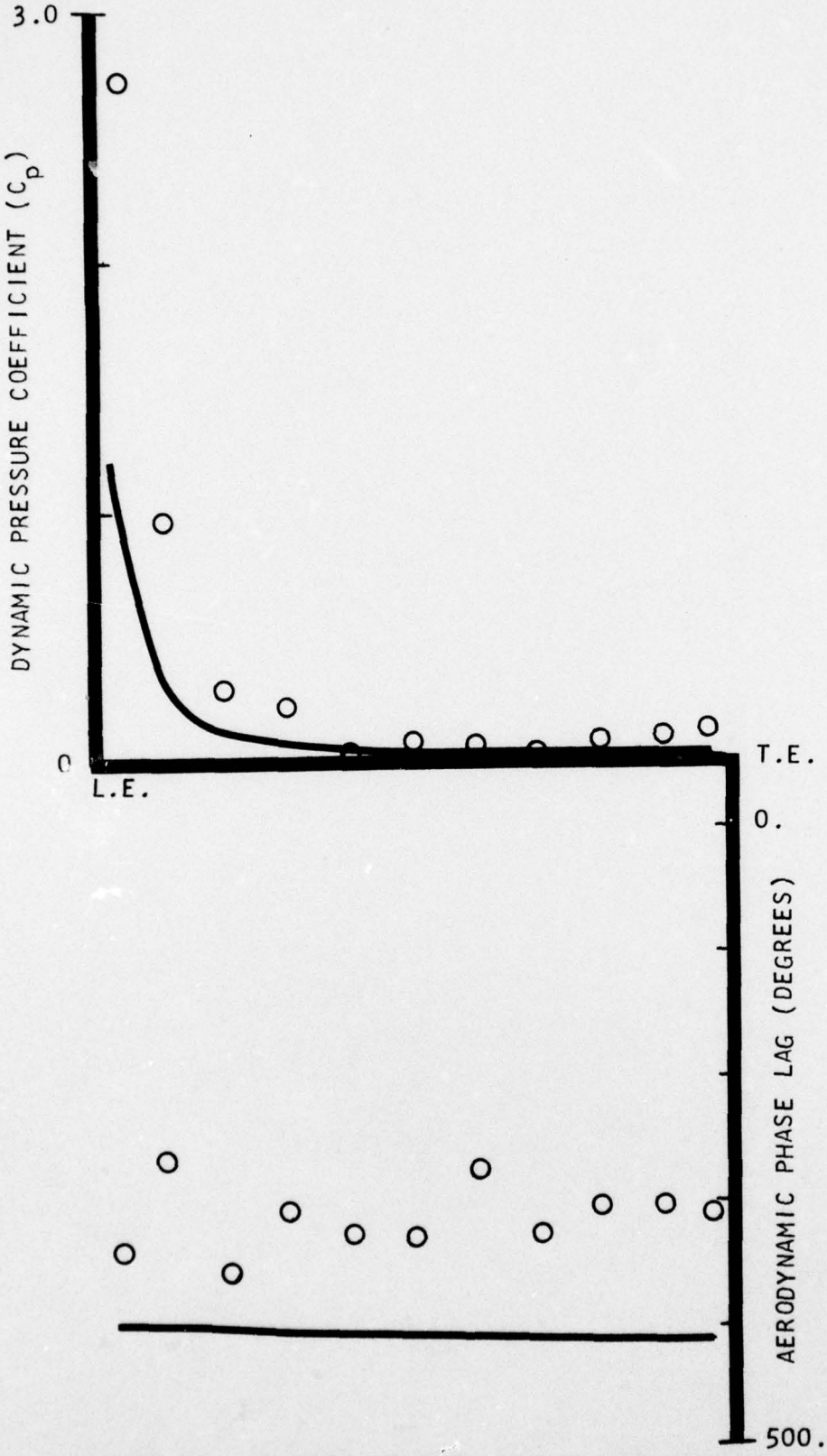

FIGURE 42. CHORDWISE DATA FOR SECOND HARMONIC UNSTEADY PRESSURE DIFFERENCE ACROSS THE VANE AND PREDICTION FROM REFERENCE 7 FOR POINT 8 FOR AN AXIAL SPACING RATIO OF 0.2374

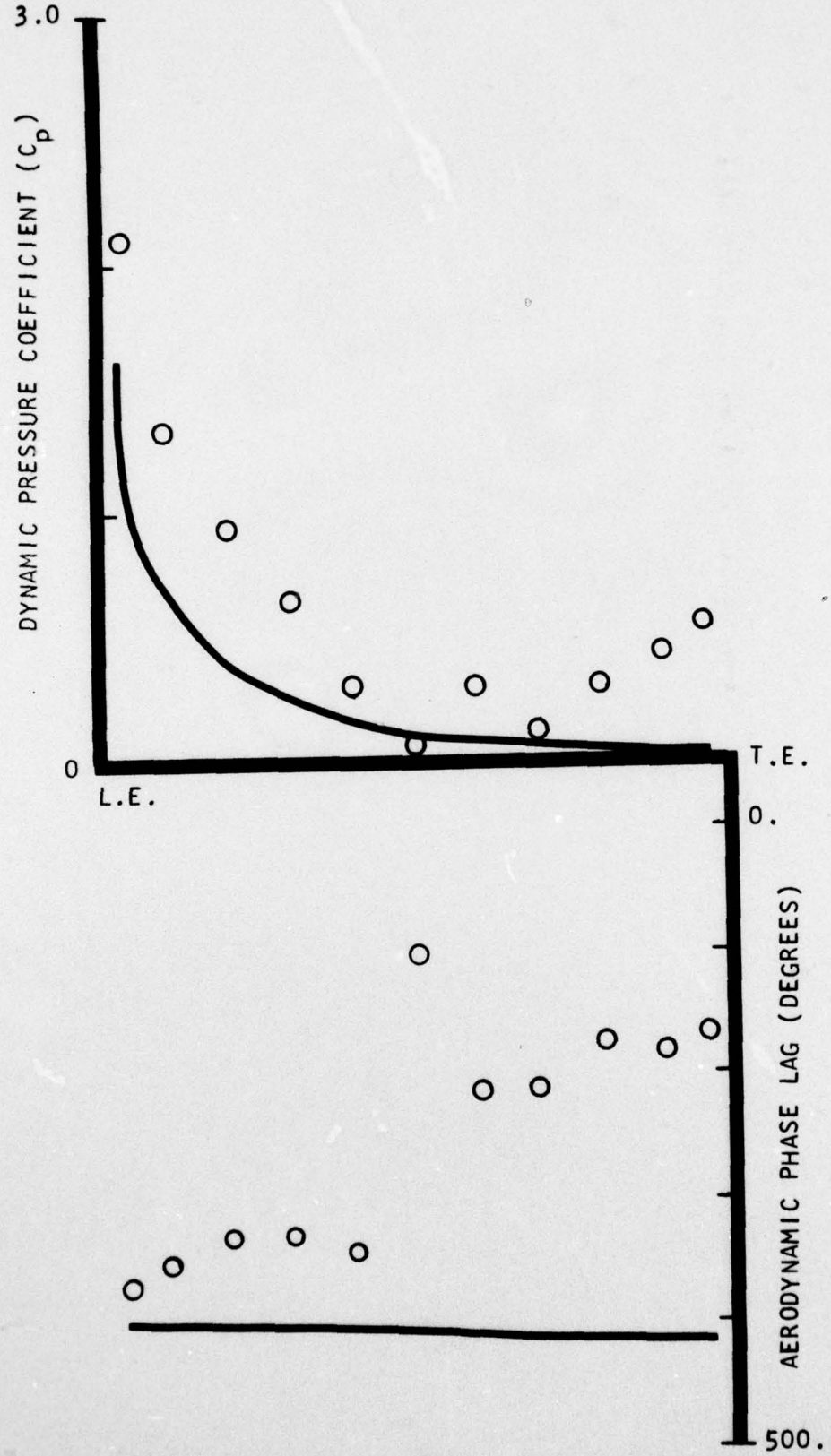

FIGURE 43. CHORDWISE DATA FOR FIRST HARMONIC UNSTEADY PRESSURE DIFFERENCE ACROSS THE VANE AND PREDICTION FROM REFERENCE 7 FOR POINT 15 FOR AN AXIAL SPACING RATIO OF 0.4305

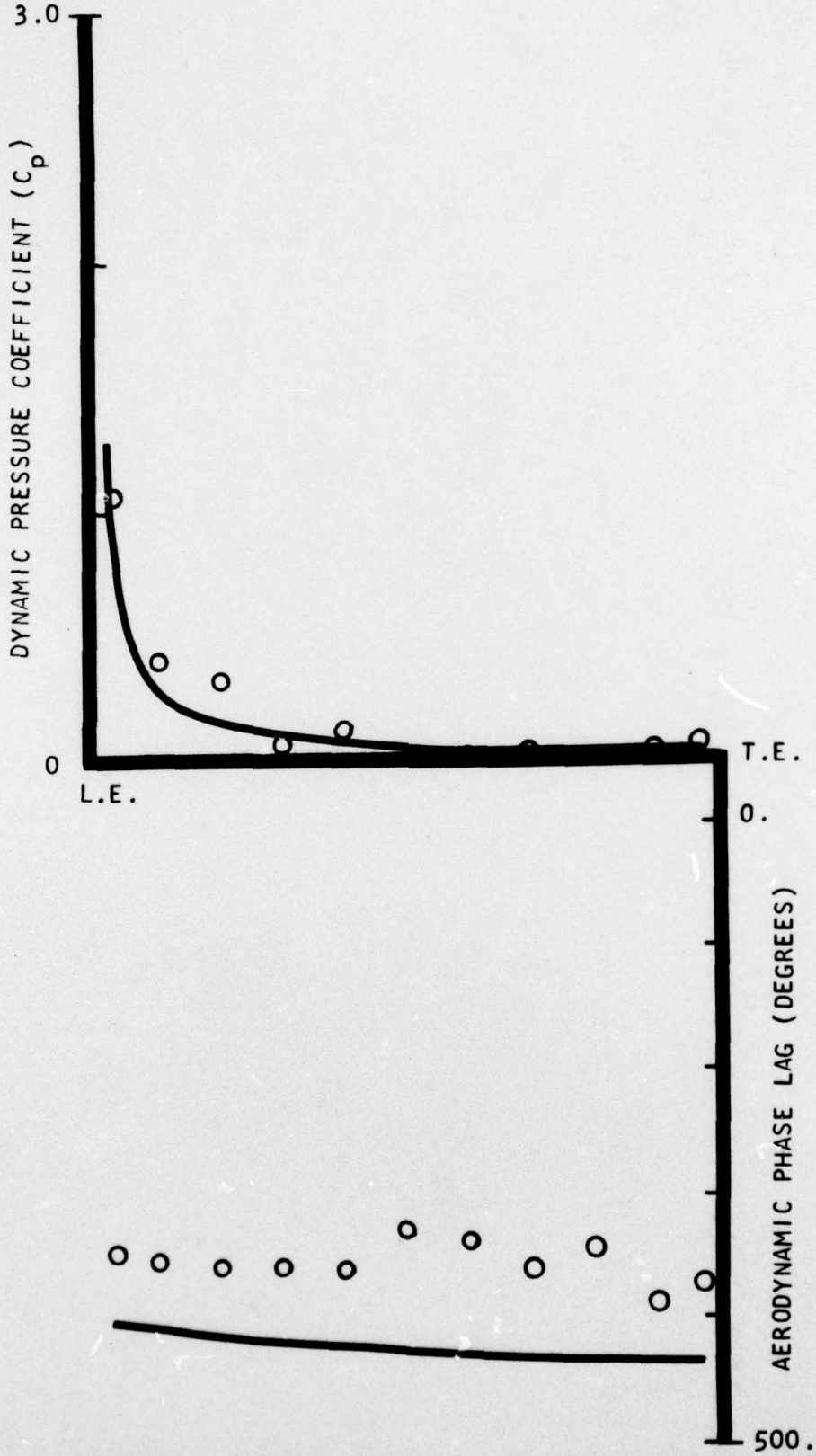

FIGURE 44. CHORDWISE DATA FOR SECOND HARMONIC UNSTEADY PRESSURE DIFFERENCE ACROSS THE VANE AND PREDICTION FROM REFERENCE 7 FOR POINT 15 FOR AN AXIAL SPACING RATIO OF 0.4305

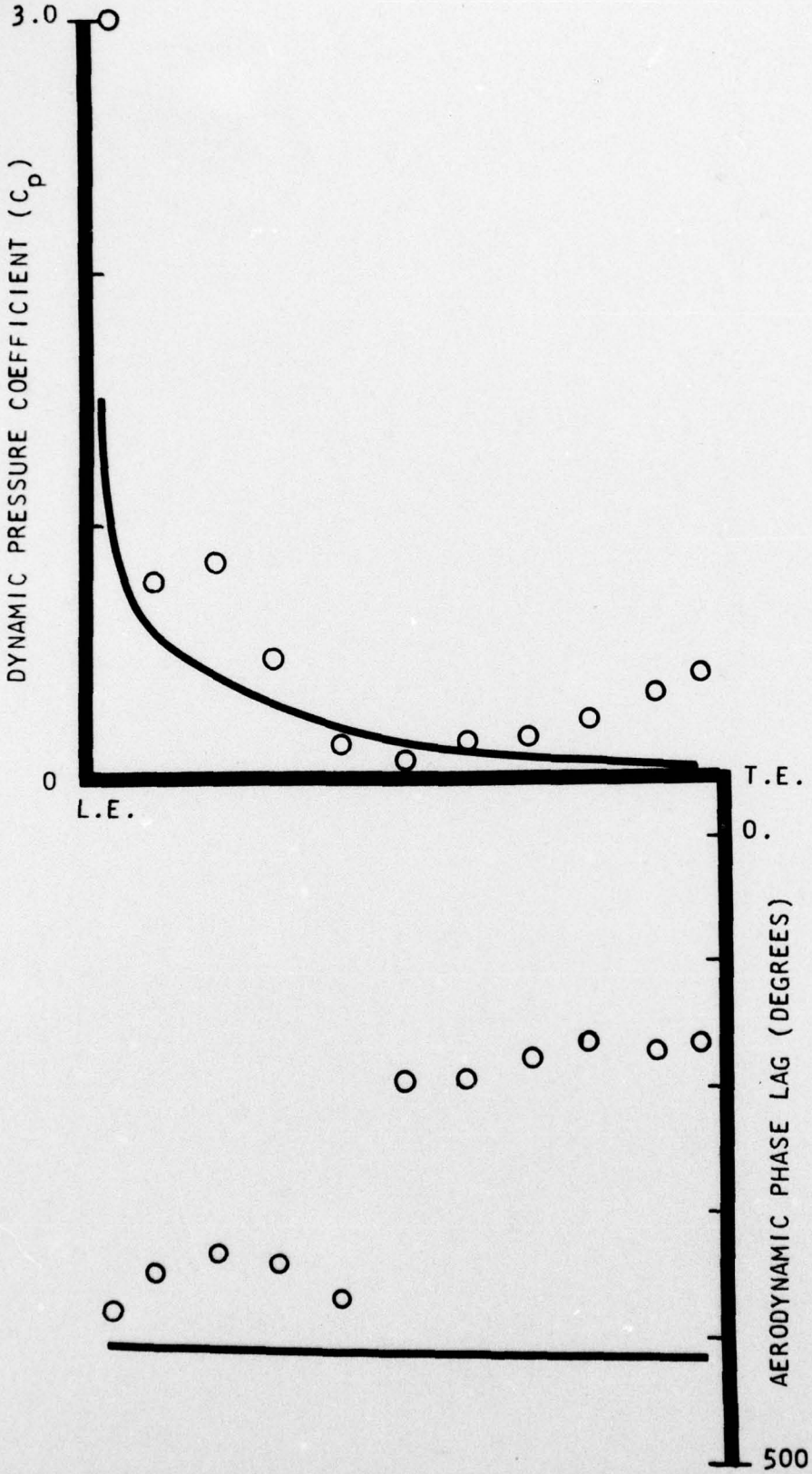

FIGURE 45. CHORDWISE DATA FOR FIRST HARMONIC UNSTEADY PRESSURE DIFFERENCE ACROSS THE VANE AND PREDICTION FROM REFERENCE 7 FOR POINT 16 FOR AN AXIAL SPACING RATIO OF 0.4305

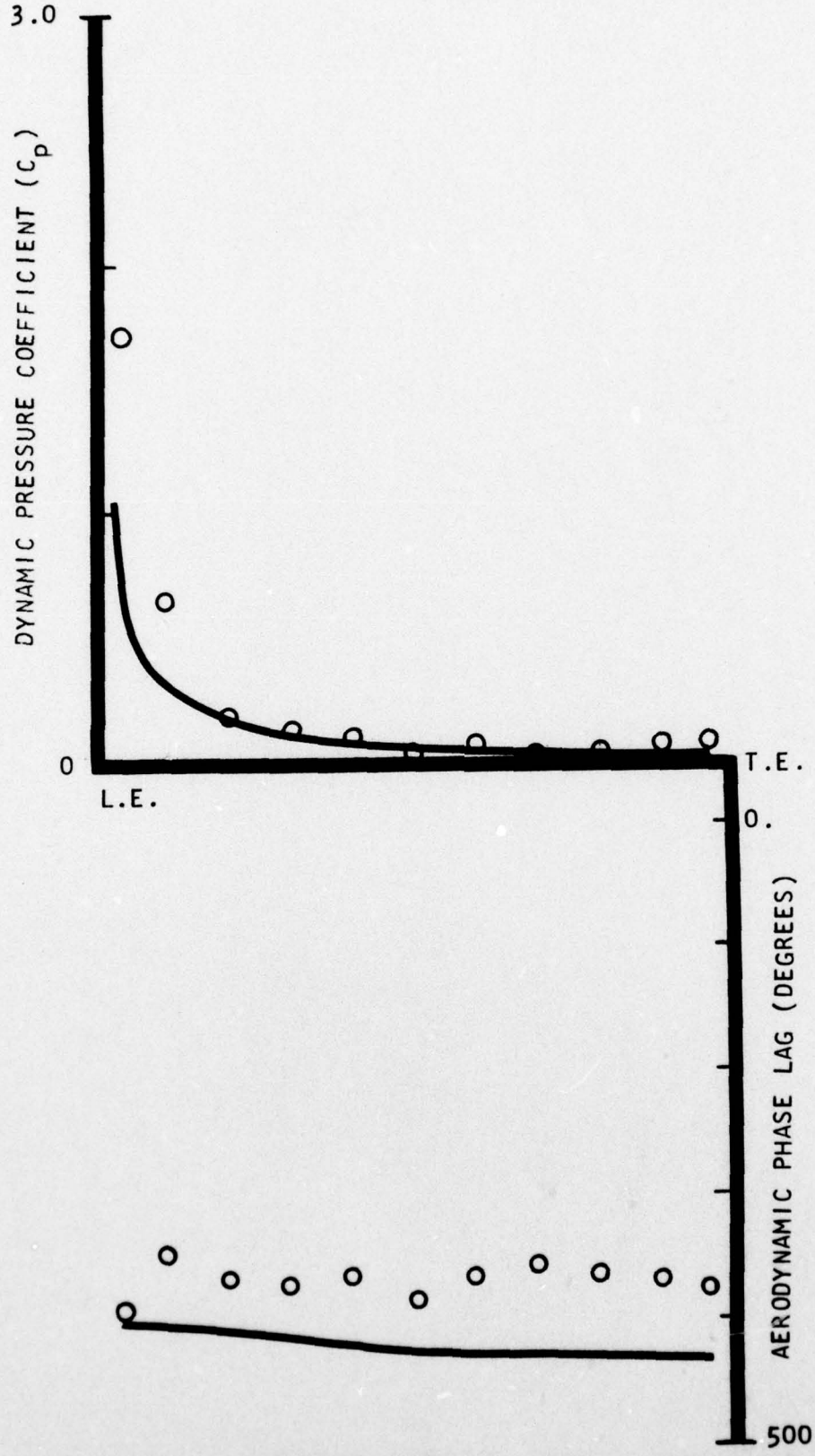

FIGURE 46. CHORDWISE DATA FOR SECOND HARMONIC UNSTEADY PRESSURE DIFFERENCE ACROSS THE VANE AND PREDICTION FROM REFERENCE 7 FOR POINT 16 FOR AN AXIAL SPACING RATIO OF 0.4305

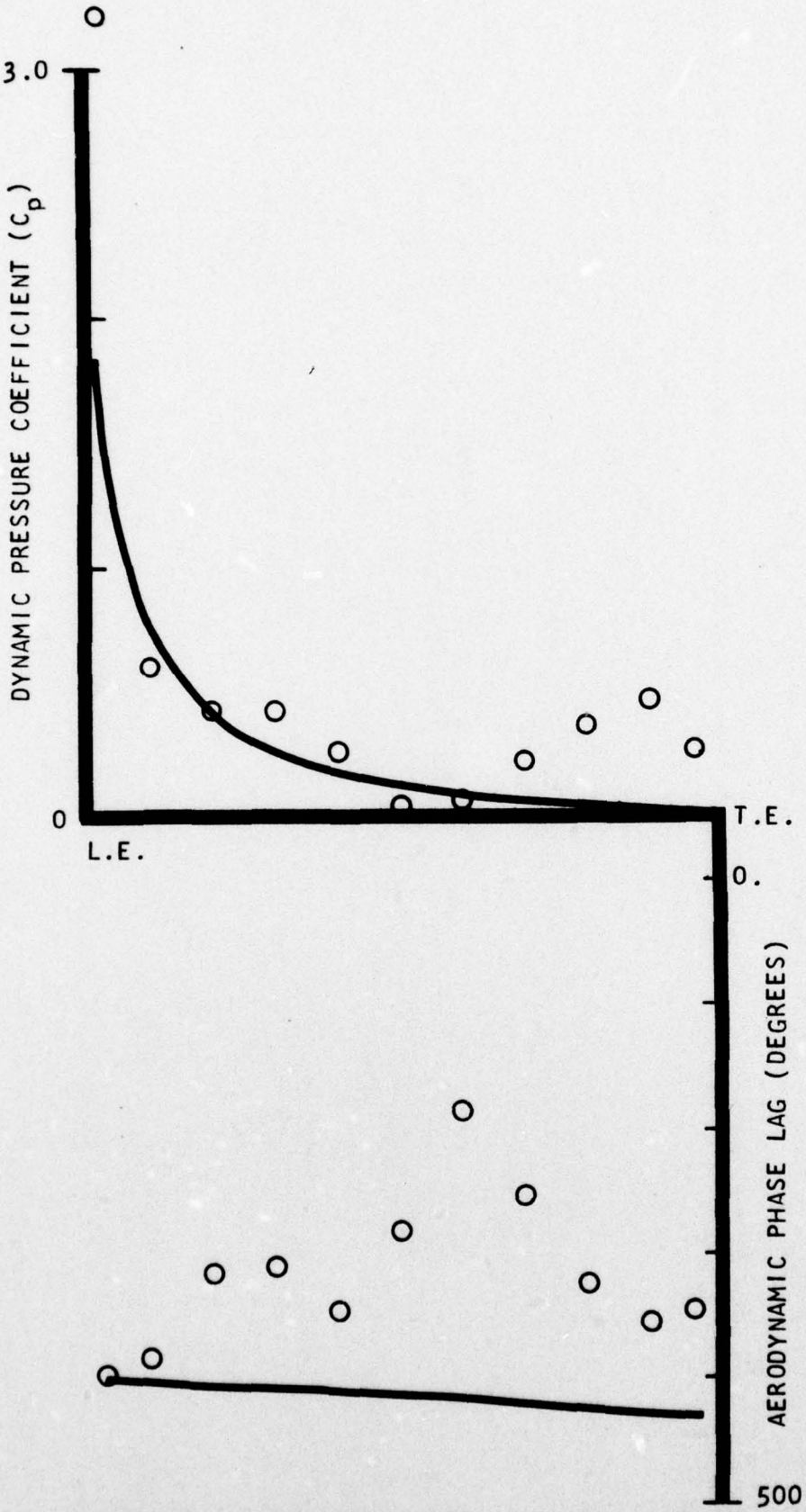

FIGURE 47. CHORDWISE DATA FOR FIRST HARMONIC UNSTEADY PRESSURE DIFFERENCE ACROSS THE VANE AND PREDICTION FROM REFERENCE 7 FOR POINT 2 FOR AN AXIAL SPACING RATIO OF 0.2374

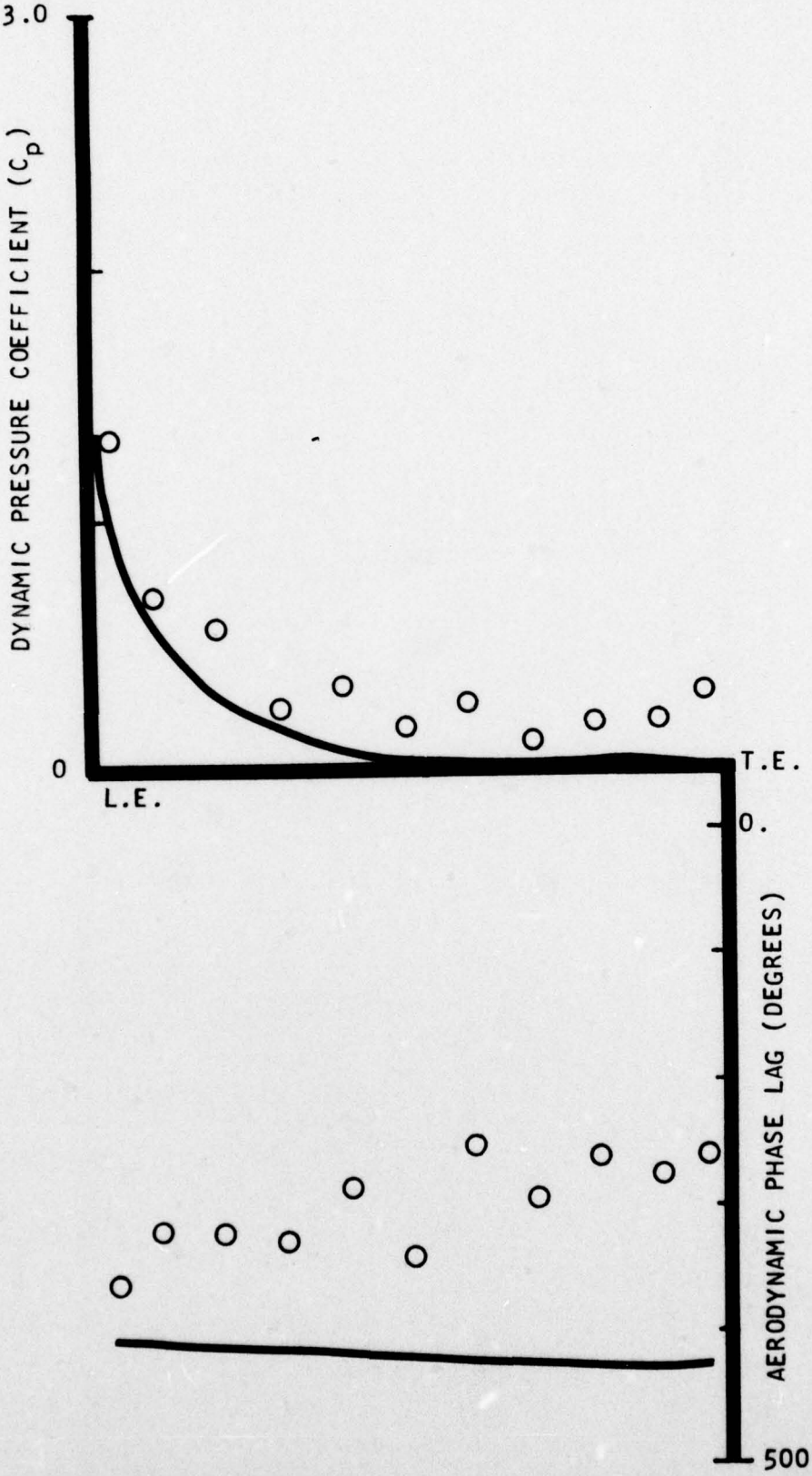

FIGURE 48. CHORDWISE DATA FOR SECOND HARMONIC UNSTEADY PRESSURE DIFFERENCE ACROSS THE VANE AND PREDICTION FROM REFERENCE 7 FOR POINT 2 FOR AN AXIAL SPACING RATIO OF 0.2374

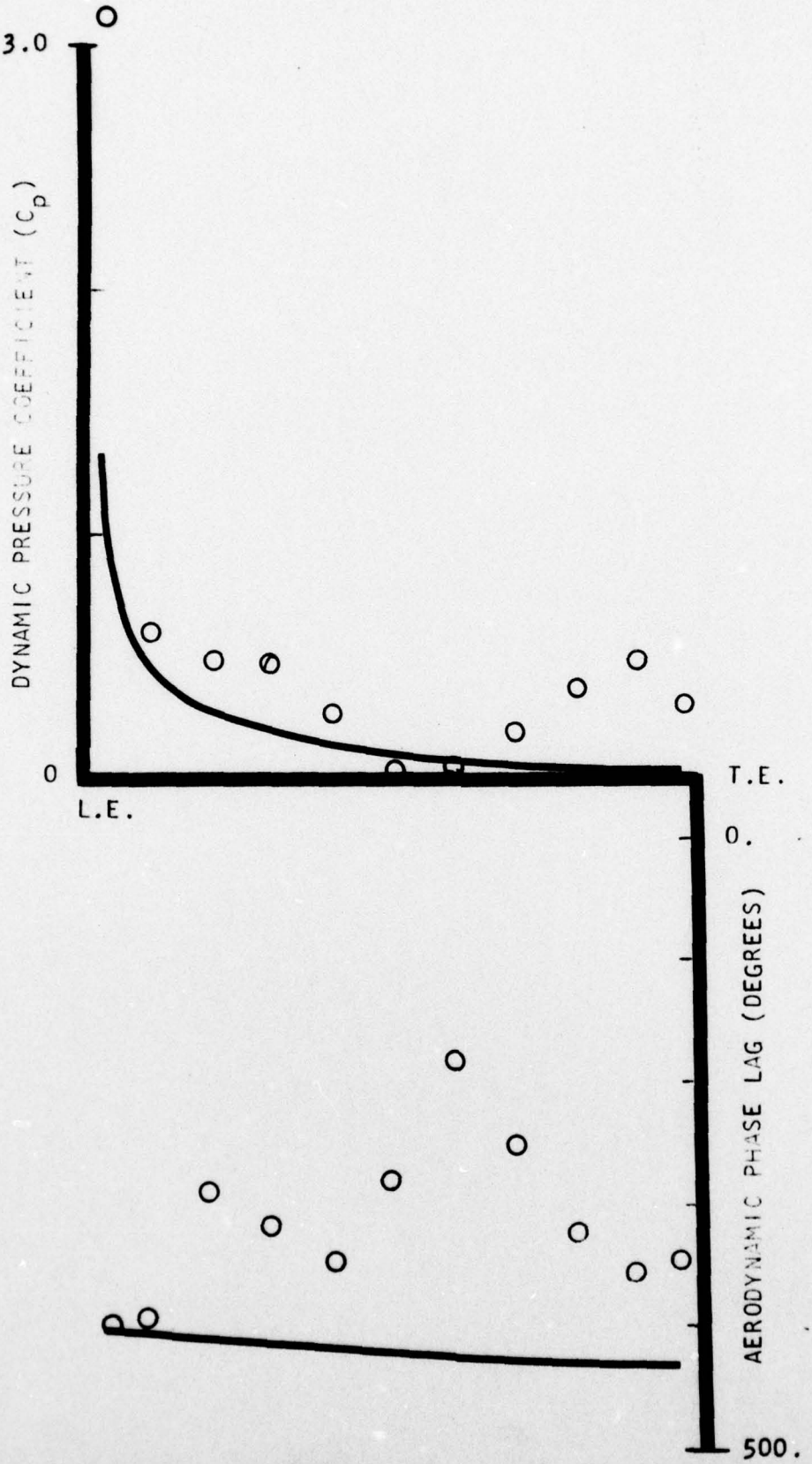

FIGURE 49. CHORDWISE DATA FOR FIRST HARMONIC UNSTEADY PRESSURE DIFFERENCE ACROSS THE VANE AND PREDICTION FROM REFERENCE 7 FOR POINT 10 FOR AN AXIAL SPACING RATIO OF 0.4305

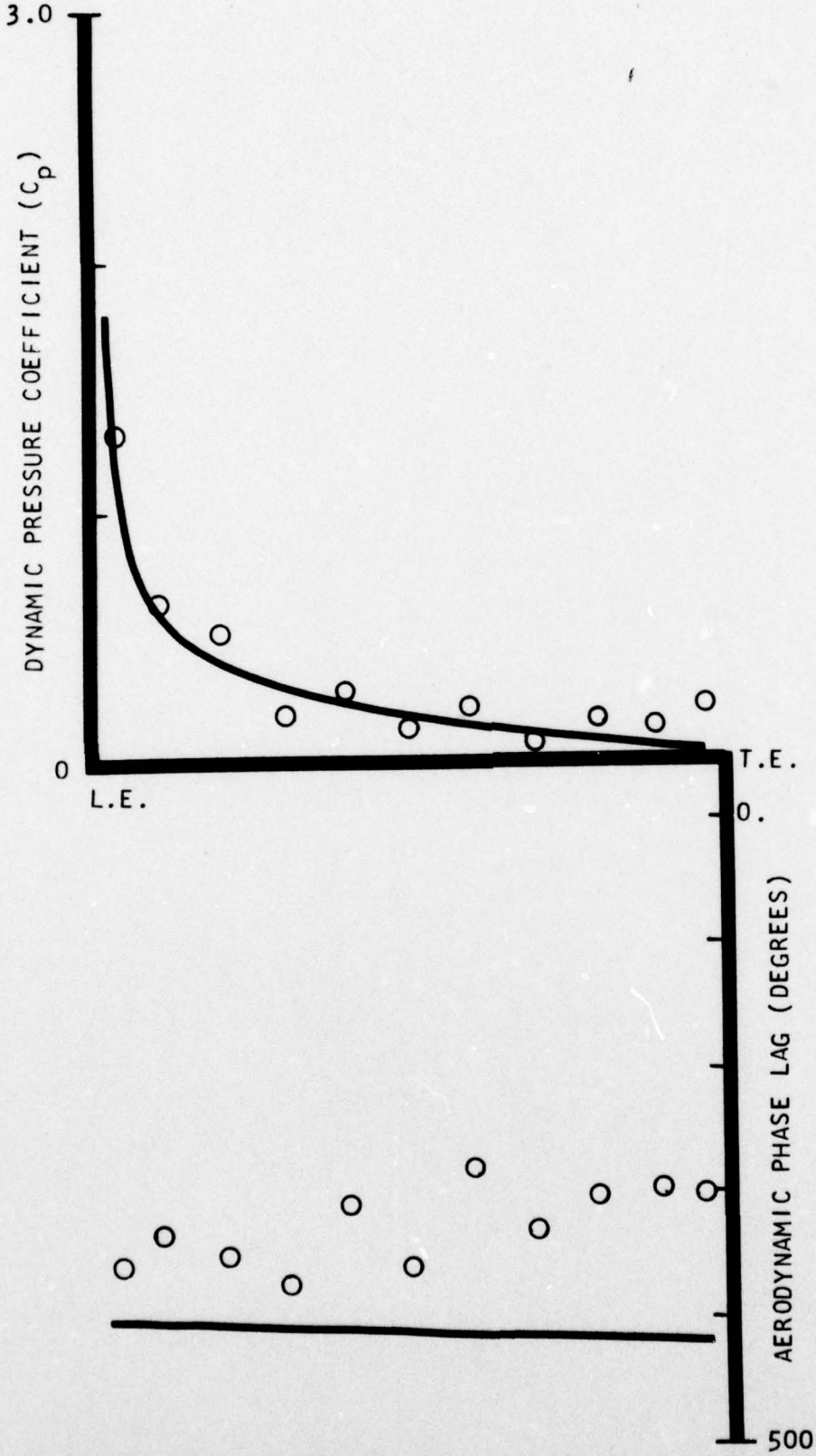

FIGURE 50. CHORDWISE DATA FOR SECOND HARMONIC UNSTEADY PRESSURE DIFFERENCE ACROSS THE VANE AND PREDICTION FROM REFERENCE 7 FOR POINT 10 FOR AN AXIAL SPACING RATIO OF 0.4305

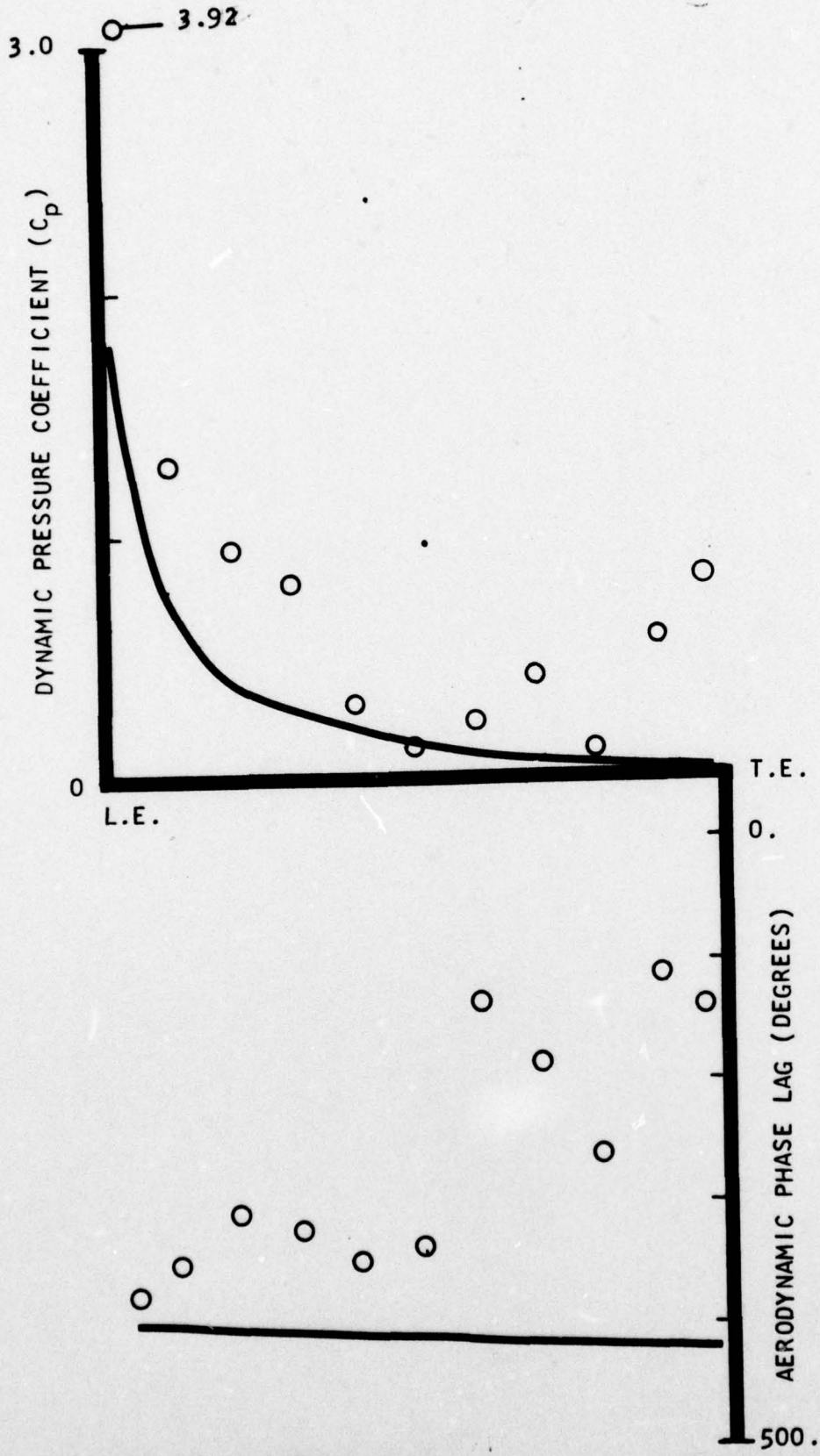

FIGURE 51. CHORDWISE DATA FOR FIRST HARMONIC UNSTEADY PRESSURE DIFFERENCE ACROSS THE VANE AND PREDICTION FROM REFERENCE 7 FOR POINT 6 FOR AN AXIAL SPACING RATIO OF 0.2374

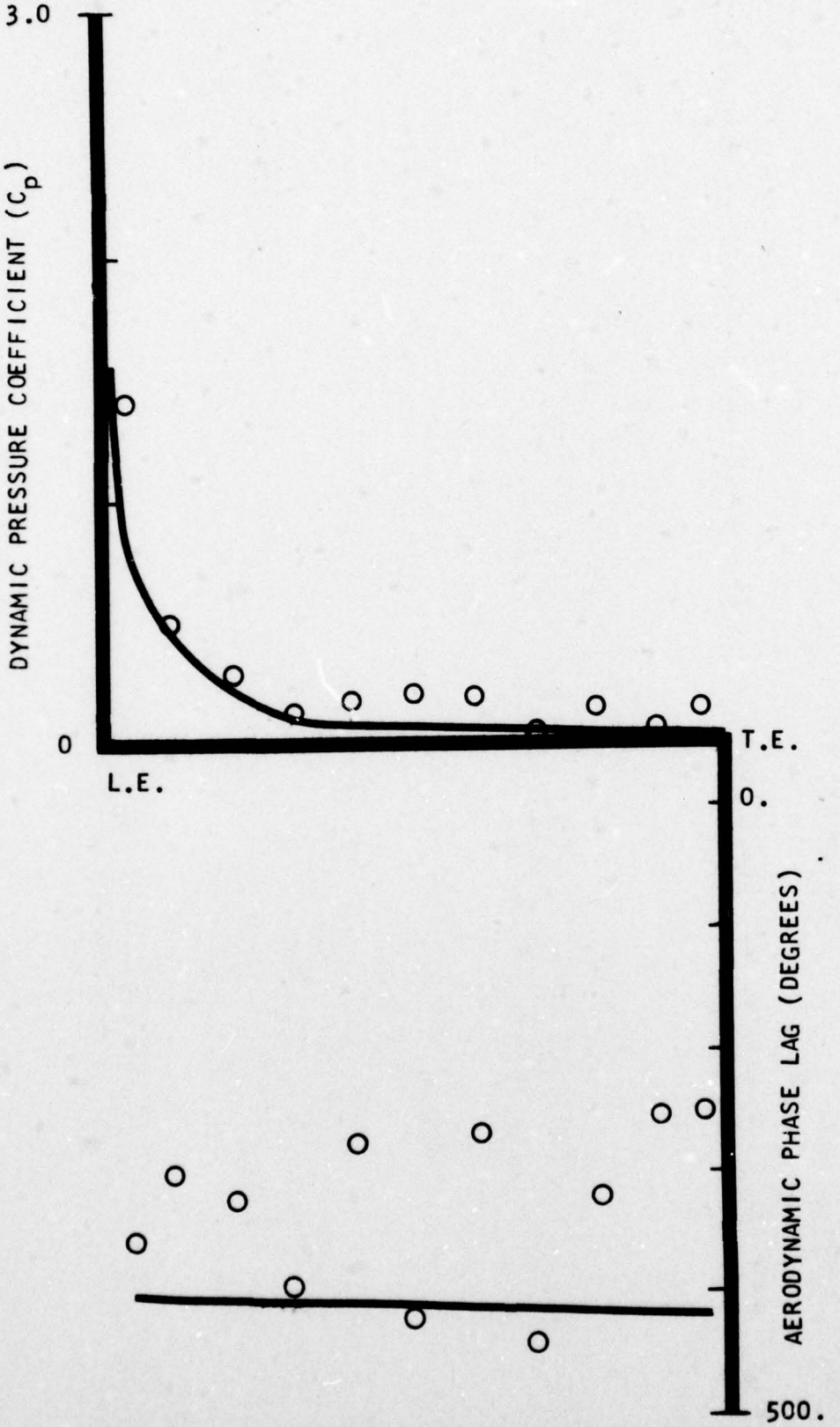

FIGURE 52. CHORDWISE DATA FOR SECOND HARMONIC UNSTEADY PRESSURE DIFFERENCE ACROSS THE VANE AND PREDICTION FROM REFERENCE 7 FOR POINT 6 FOR AN AXIAL SPACING RATIO OF 0.2374

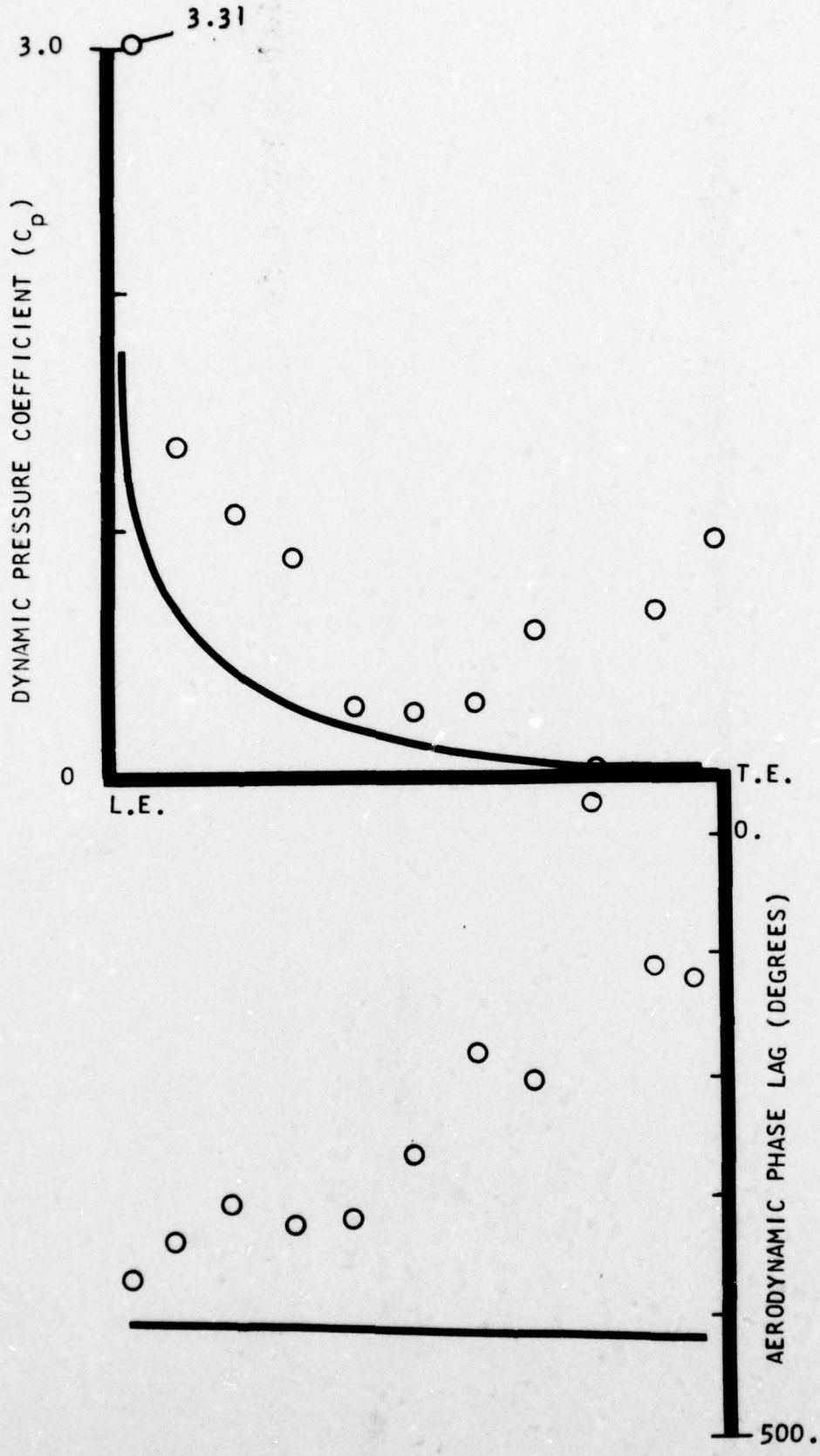

FIGURE 53. CHORDWISE DATA FOR FIRST HARMONIC UNSTEADY PRESSURE DIFFERENCE ACROSS THE VANE AND PREDICTION FROM REFERENCE 7 FOR POINT 14 FOR AN AXIAL SPACING RATIO OF 0.4305

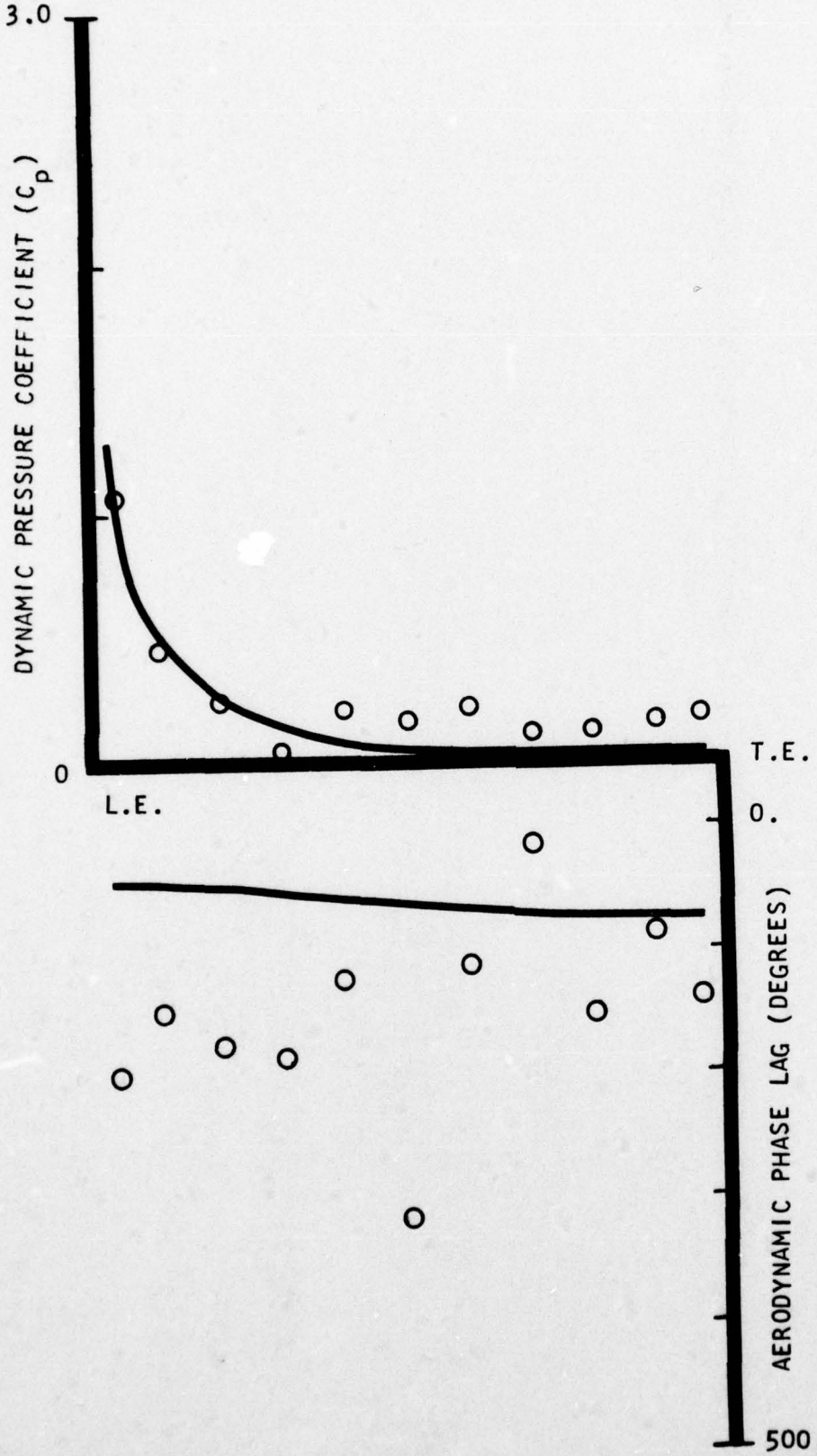

FIGURE 54. CHORDWISE DATA FOR SECOND HARMONIC UNSTEADY PRESSURE DIFFERENCE ACROSS THE VANE AND PREDICTION FROM REFERENCE 7 FOR POINT 14 FOR AN AXIAL SPACING RATIO OF 0.4305

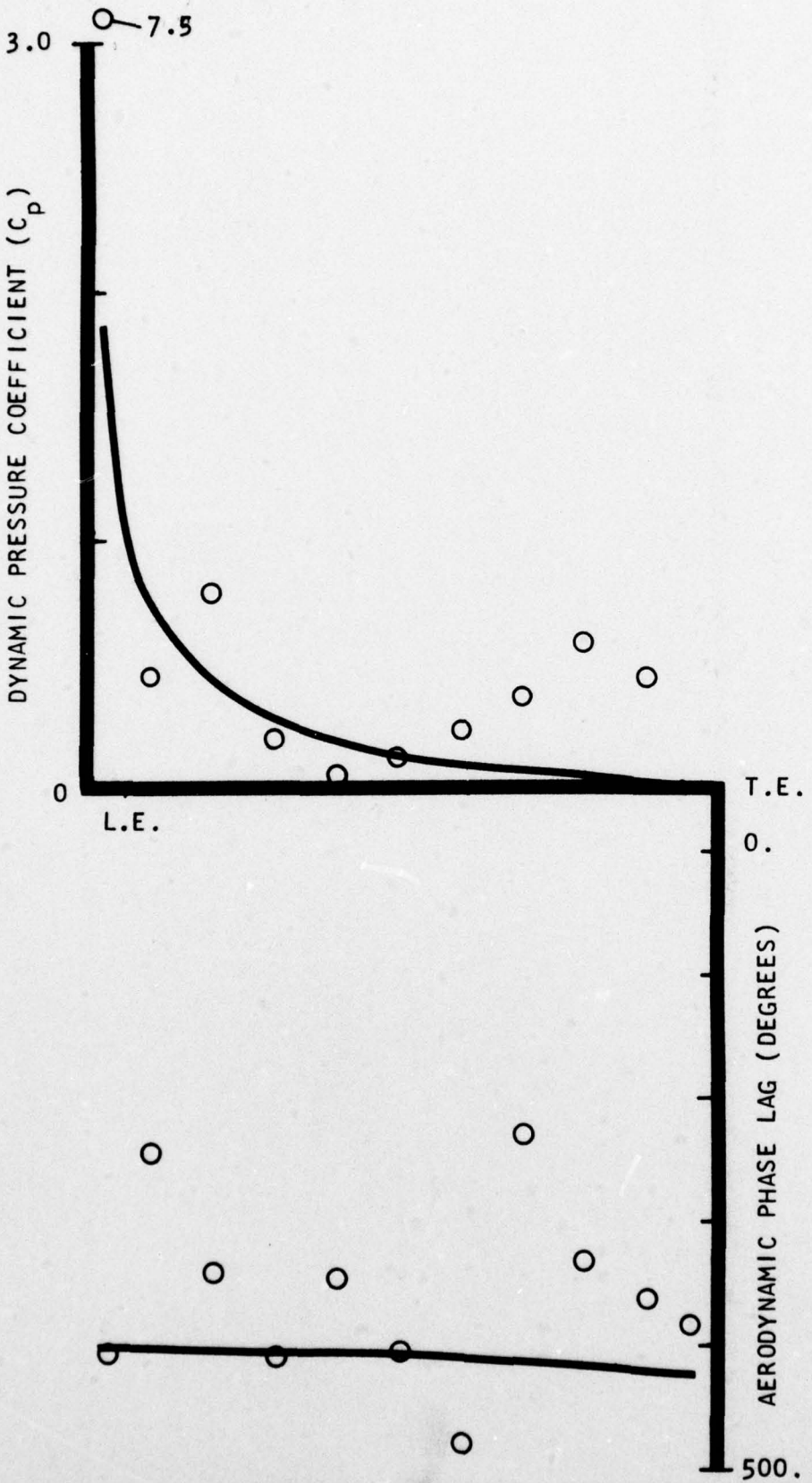

FIGURE 55. CHORDWISE DATA FOR FIRST HARMONIC UNSTEADY PRESSURE DIFFERENCE ACROSS THE VANE AND PREDICTION FROM REFERENCE 7 FOR POINT 1 FOR AN AXIAL SPACING RATIO OF 0.2374

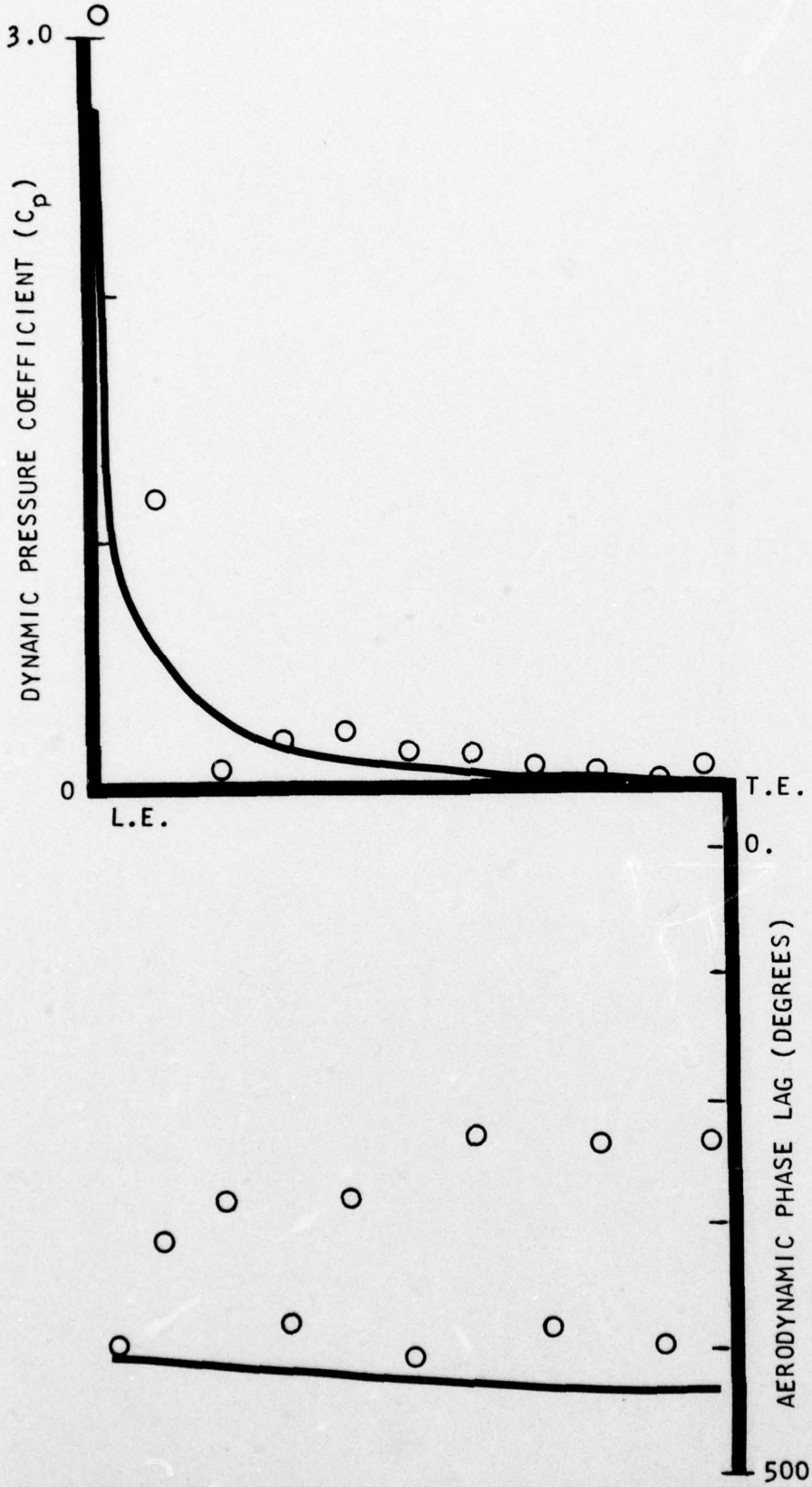

FIGURE 56. CHORDWISE DATA FOR SECOND HARMONIC UNSTEADY PRESSURE DIFFERENCE ACROSS THE VANE AND PREDICTION FROM REFERENCE 7 FOR POINT 1 FOR AN AXIAL SPACING RATIO OF 0.2374

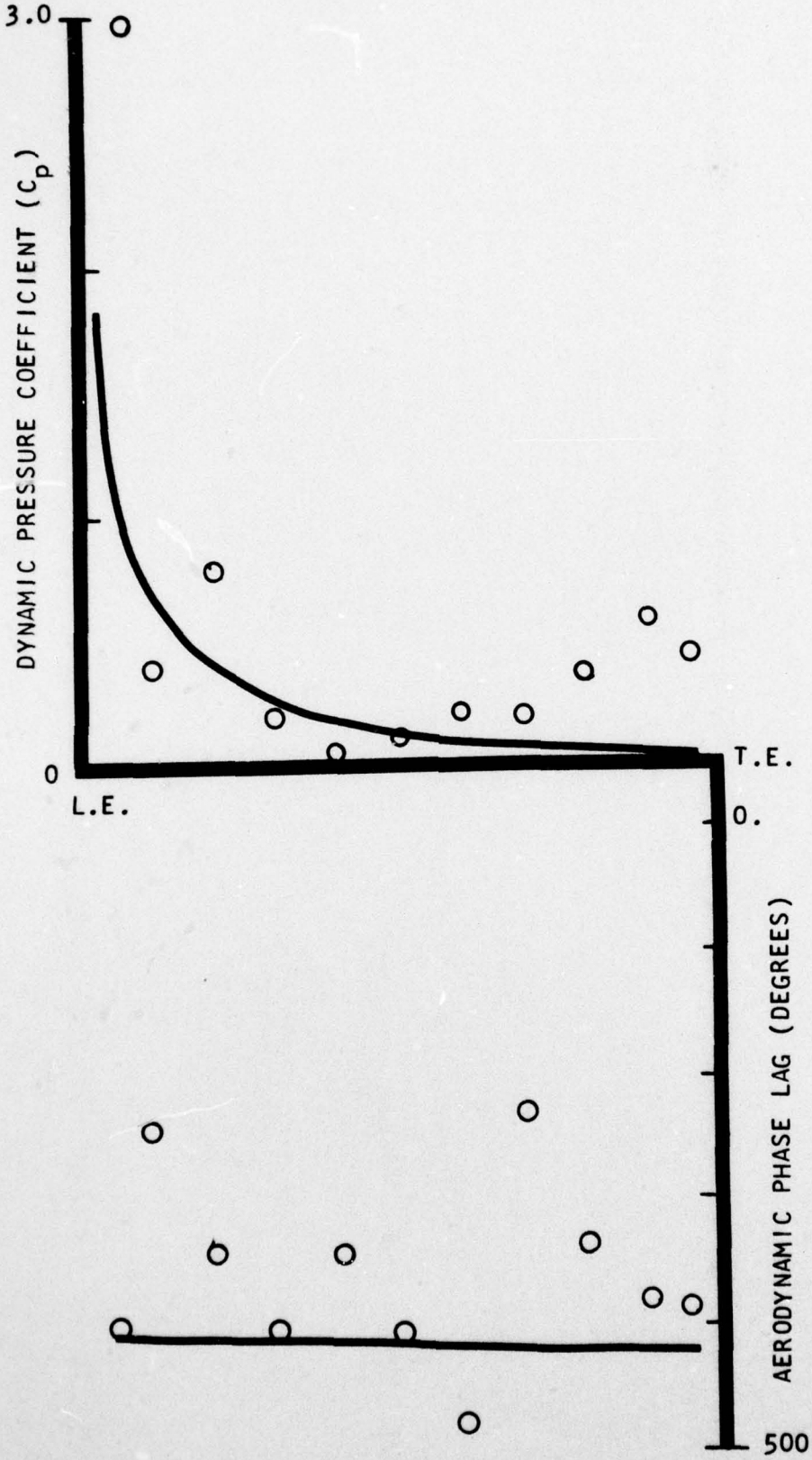

FIGURE 57. CHORDWISE DATA FOR FIRST HARMONIC UNSTEADY PRESSURE DIFFERENCE ACROSS THE VANE AND PREDICTION FROM REFERENCE 7 FOR POINT 9 FOR AN AXIAL SPACING RATIO OF 0.4305

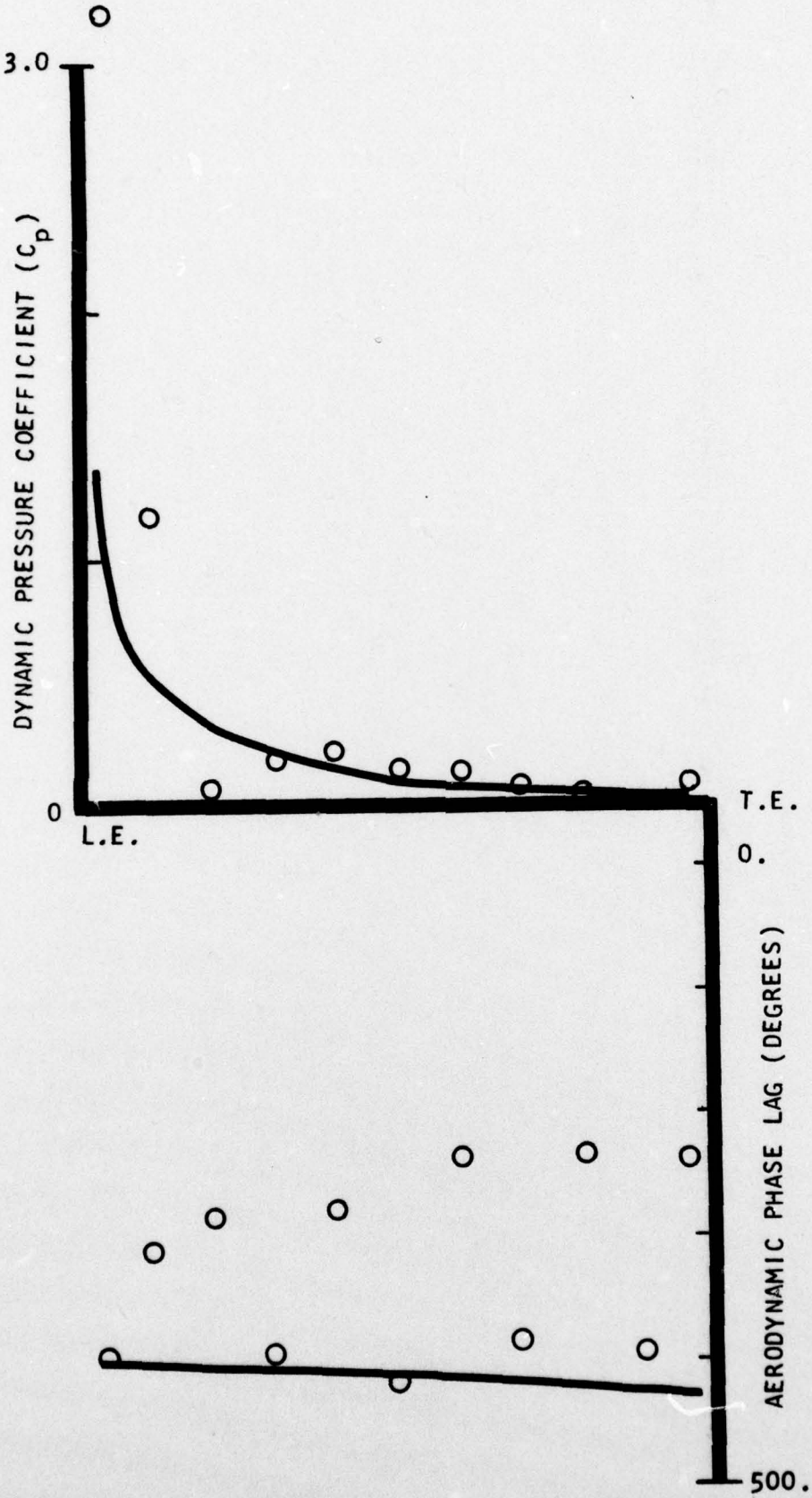

FIGURE 58. CHORDWISE DATA FOR SECOND HARMONIC UNSTEADY PRESSURE DIFFERENCE ACROSS THE VANE AND PREDICTION FROM REFERENCE 7 FOR POINT 9 FOR AN AXIAL SPACING RATIO OF 0.4305

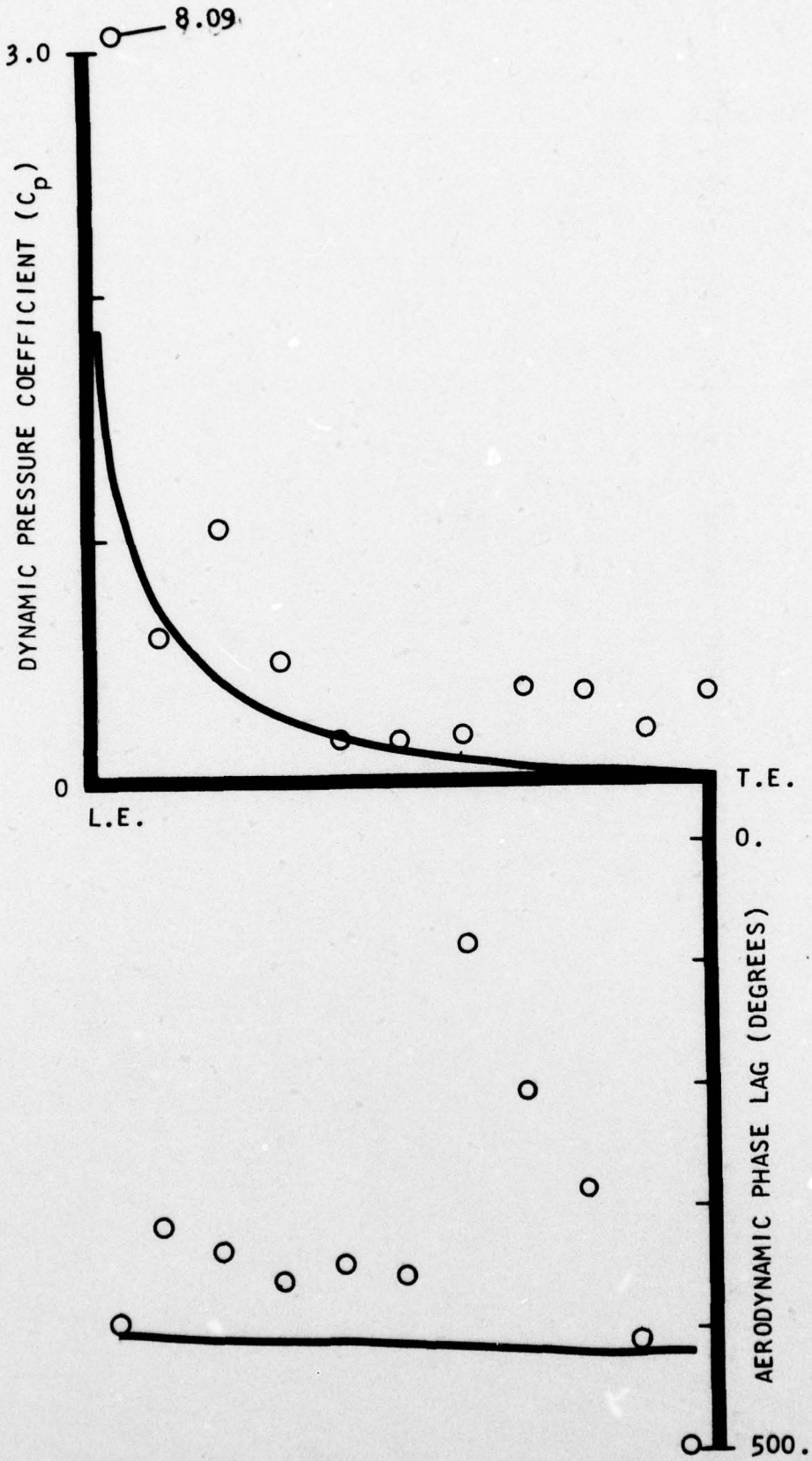

FIGURE 59. CHORDWISE DATA FOR FIRST HARMONIC UNSTEADY PRESSURE DIFFERENCE ACROSS THE VANE AND PREDICTION FROM REFERENCE 7 FOR POINT 5 FOR AN AXIAL SPACING RATIO OF 0.2374

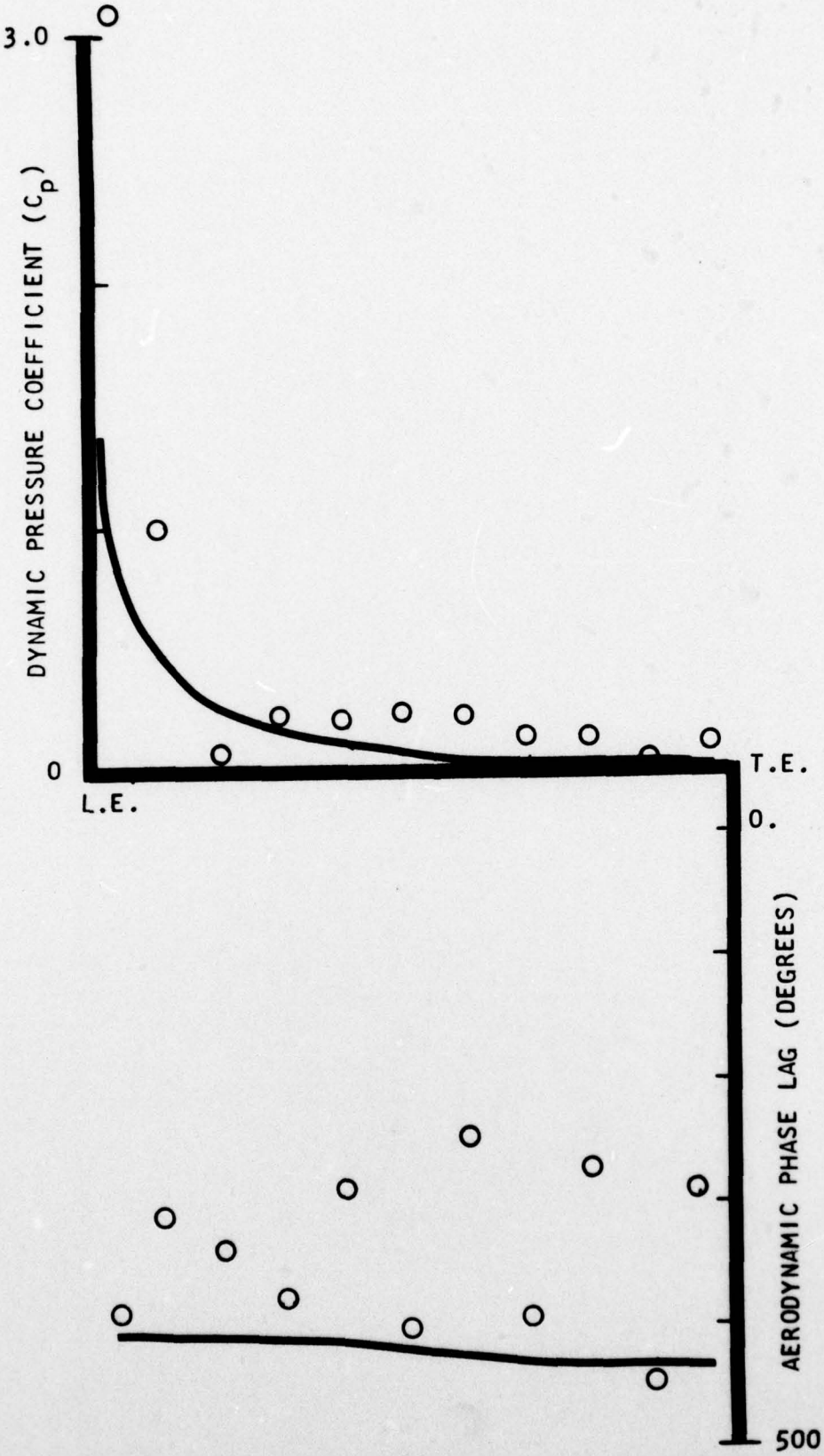

FIGURE 60. CHORDWISE DATA FOR SECOND HARMONIC UNSTEADY PRESSURE DIFFERENCE ACROSS THE VANE AND PREDICTION FROM REFERENCE 7 FOR POINT 5 FOR AN AXIAL SPACING RATIO OF 0.2374

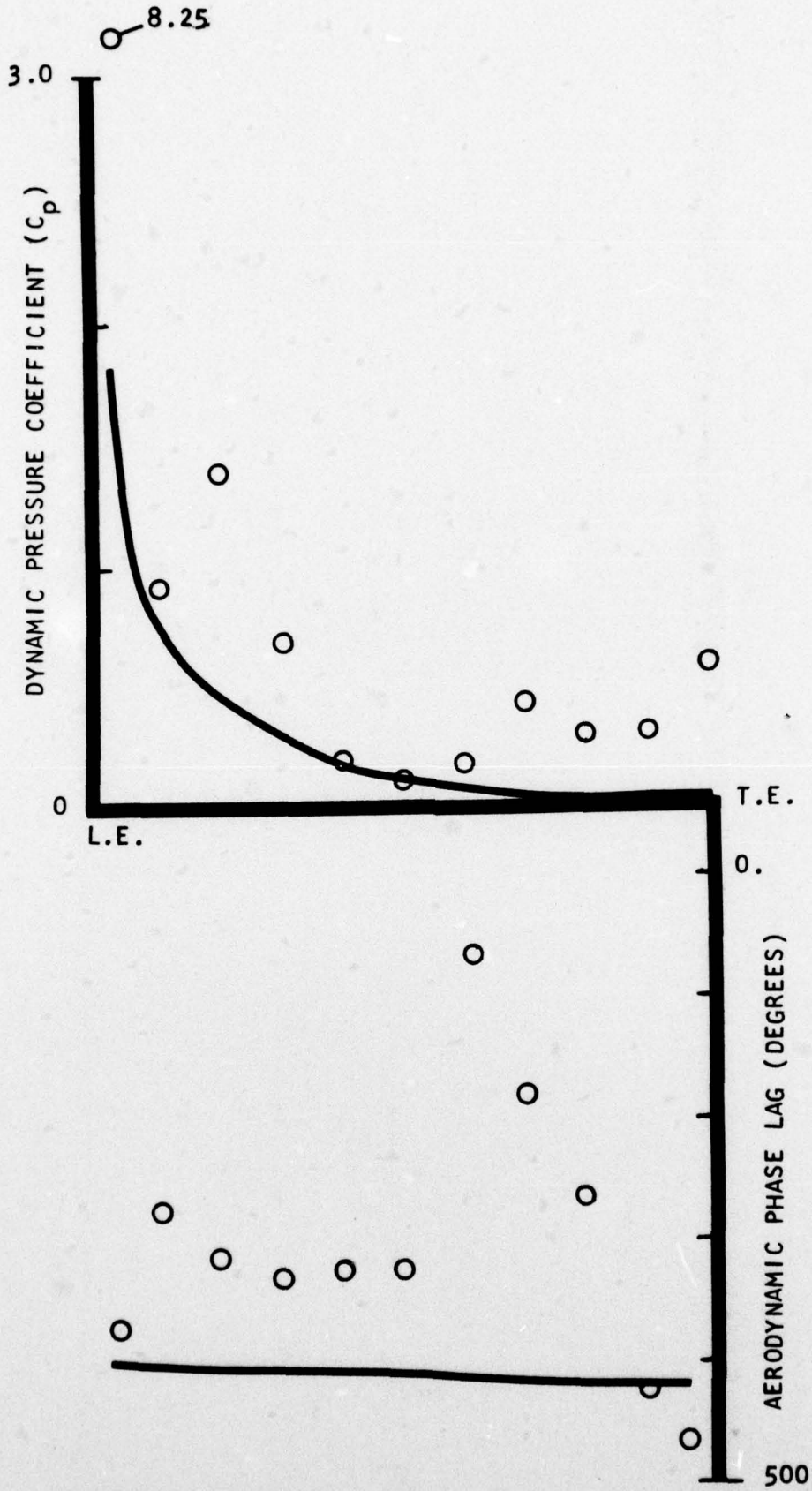

FIGURE 61. CHORDWISE DATA FOR FIRST HARMONIC UNSTEADY PRESSURE DIFFERENCE ACROSS THE VANE AND PREDICTION FROM REFERENCE 7 FOR POINT 13 FOR AN AXIAL SPACING RATIO OF 0.4305

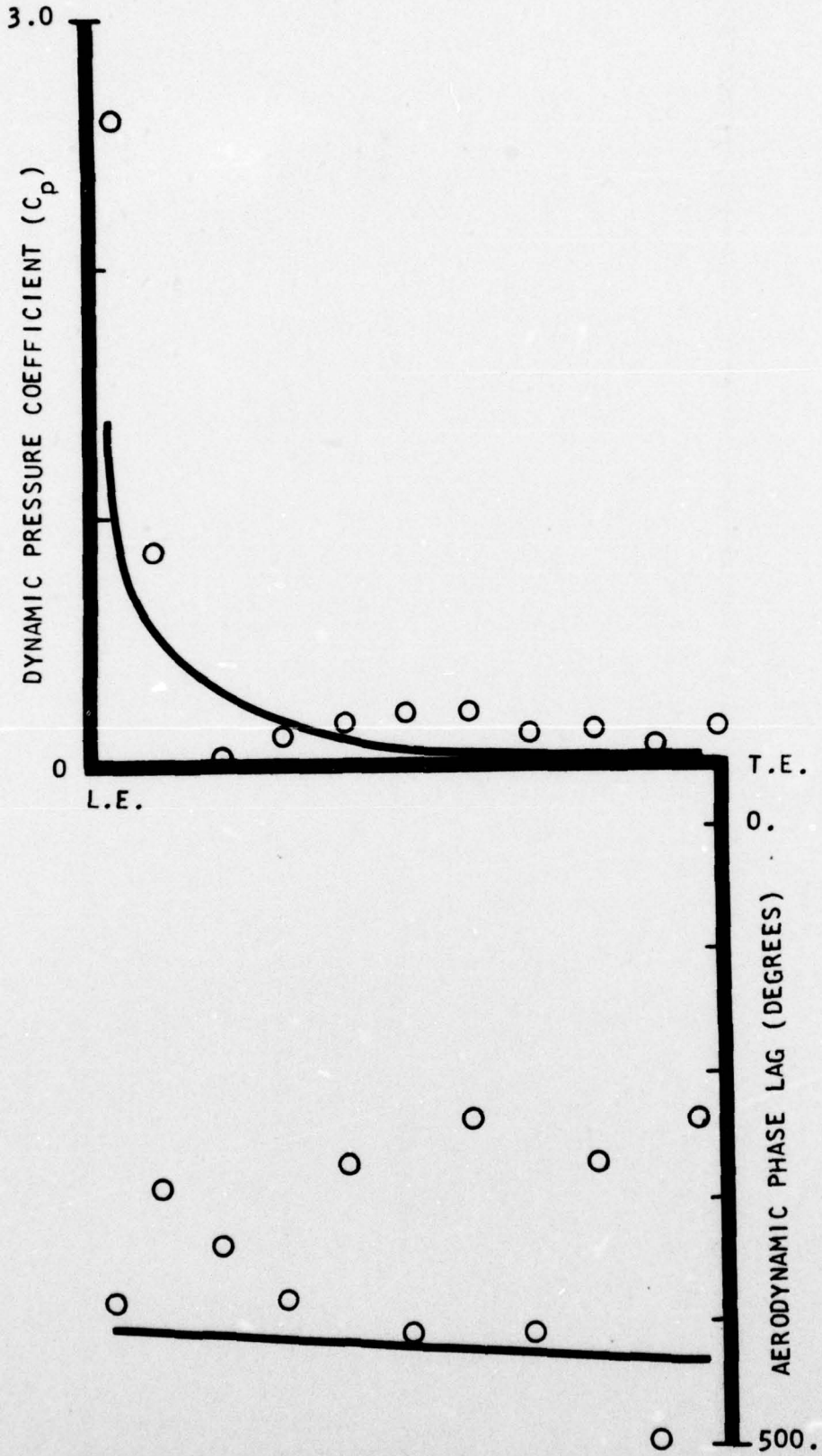

FIGURE 62. CHORDWISE DATA FOR SECOND HARMONIC UNSTEADY PRESSURE DIFFERENCE ACROSS THE VANE AND PREDICTION FROM REFERENCE 7 FOR POINT 13 FOR AN AXIAL SPACING RATIO OF 0.4305

APPENDIX

PRESSURE AND SUCTION SURFACE TIME-VARIANT PRESSURE DATA

DATA POINT 1 — FIRST HARMONIC

AXIAL LOCATION PERCENT OF CHORD	SUCTION SURFACE AMPLITUDE	SUCTION SURFACE PHASE	PRESSURE SURFACE AMPLITUDE	PRESSURE SURFACE PHASE
2.04	1.406	-185.	0.362	-414.
10.00	0.586	-196.	0.694	-420.
20.00	0.506	-463.	0.604	-579.
30.00	0.551	-132.	0.586	-472.
40.00	0.354	-171.	0.307	-172.
50.00	0.140	-206.	0.045	-149.
60.00	0.051	-221.	0.233	-132.
70.00	0.188	-463.	0.179	-173.
80.00	0.512	-161.	0.132	-168.
90.00	0.648	-205.	0.076	-254.
97.00	0.442	-208.	0.010	-341.

DATA POINT 1 — SECOND HARMONIC

AXIAL LOCATION PERCENT OF CHORD	SUCTION SURFACE AMPLITUDE	SUCTION SURFACE PHASE	PRESSURE SURFACE AMPLITUDE	PRESSURE SURFACE PHASE
2.94	0.755	-522.	2.695	-404.
10.00	0.221	-470.	0.970	-312.
20.00	0.229	-505.	0.185	-523.
30.00	0.062	-569.	0.260	-573.
40.00	0.227	-458.	0.012	-253.
50.00	0.093	-585.	0.066	-420.
60.00	0.175	-414.	0.035	-420.
70.00	0.117	-536.	0.052	-488.
80.00	0.083	-463.	0.063	-502.
90.00	0.092	-540.	0.085	-537.
97.00	0.069	-471.	0.082	-551.

DATA POINT 2 — FIRST HARMONIC

AXIAL LOCATION	SUCTION SURFACE		PRESSURE SURFACE	
PERCENT OF CHORD	AMPLITUDE	PHASE	AMPLITUDE	PHASE
2.94	1.388	-153.	2.880	-423.
10.00	0.493	-461.	0.888	-420.
20.00	1.030	-440.	0.648	-419.
30.00	0.854	-450.	0.606	-416.
40.00	0.544	-456.	0.527	-427.
50.00	0.358	-437.	0.308	-435.
60.00	0.334	-406.	0.295	-414.
70.00	0.523	-428.	0.302	-426.
80.00	0.536	-135.	0.166	-118.
90.00	0.394	-188.	0.122	-318.
97.00	0.299	-153.	0.063	-429.

DATA POINT 2 — SECOND HARMONIC

AXIAL LOCATION	SUCTION SURFACE		PRESSURE SURFACE	
PERCENT OF CHORD	AMPLITUDE	PHASE	AMPLITUDE	PHASE
2.94	1.002	-510.	0.502	-592.
10.00	0.365	-495.	0.330	-517.
20.00	0.373	-477.	0.274	-553.
30.00	0.140	-415.	0.287	-557.
40.00	0.378	-435.	0.172	-574.
50.00	0.055	-383.	0.209	-550.
60.00	0.284	-405.	0.123	-536.
70.00	0.073	-367.	0.149	-322.
80.00	0.133	-430.	0.062	-285.
90.00	0.095	-367.	0.187	-280.
97.00	0.147	-447.	0.149	-252.

DATA POINT 3 — FIRST HARMONIC

AXIAL LOCATION	SUCTION SURFACE		PRESSURE SURFACE	
PERCENT OF CHORD	AMPLITUDE	PHASE	AMPLITUDE	PHASE
2.94	0.856	-415.	1.930	-381.
10.00	0.848	-417.	1.175	-378.
20.00	1.175	-423.	1.144	-382.
30.00	0.942	-422.	0.895	-388.
40.00	0.833	-409.	0.856	-381.
50.00	0.786	-388.	0.763	-381.
60.00	0.833	-396.	0.625	-384.
70.00	0.533	-409.	0.538	-377.
80.00	0.310	-396.	0.384	-378.
90.00	0.269	-428.	0.281	-376.
97.00	0.337	-113.	0.101	-384.

DATA POINT 3 – SECOND HARMONIC

AXIAL LOCATION PERCENT OF CHORD	SUCTION SURFACE AMPLITUDE	SUCTION SURFACE PHASE	PRESSURE SURFACE AMPLITUDE	PRESSURE SURFACE PHASE
2.94	1.110	-485.	0.812	-514.
10.00	0.126	-489.	0.404	-516.
20.00	0.220	-500.	0.288	-538.
30.00	0.101	-576.	0.242	-566.
40.00	0.153	-454.	0.191	-563.
50.00	0.185	-412.	0.201	-385.
60.00	0.237	-437.	0.259	-398.
70.00	0.208	-436.	0.182	-399.
80.00	0.234	-445.	0.179	-418.
90.00	0.243	-456.	0.175	-429.
97.00	0.234	-458.	0.147	-443.

DATA POINT 4 — FIRST HARMONIC

AXIAL LOCATION	SUCTION SURFACE		PRESSURE SURFACE	
PERCENT OF CHORD	AMPLITUDE	PHASE	AMPLITUDE	PHASE
2.94	2.141	-182.	1.796	-377.
10.00	0.926	-399.	1.177	-375.
20.00	1.172	-432.	1.041	-382.
30.00	0.670	-430.	0.790	-381.
40.00	0.643	-397.	0.785	-378.
50.00	0.785	-395.	0.687	-383.
60.00	0.665	-408.	0.632	-384.
70.00	0.467	-394.	0.583	-378.
80.00	0.445	-406.	0.440	-385.
90.00	0.234	-435.	0.386	-377.
97.00	0.232	-110.	0.272	-387.

DATA POINT 4 — SECOND HARMONIC

AXIAL LOCATION	SUCTION SURFACE		PRESSURE SURFACE	
PERCENT OF CHORD	AMPLITUDE	PHASE	AMPLITUDE	PHASE
2.94	2.000	-530.	0.796	-513.
10.00	0.617	-420.	0.397	-315.
20.00	0.221	-227.	0.202	-328.
30.00	0.080	-502.	0.168	-362.
40.00	0.044	-390.	0.168	-386.
50.00	0.121	-459.	0.202	-406.
60.00	0.250	-441.	0.286	-411.
70.00	0.218	-460.	0.252	-434.
80.00	0.288	-458.	0.271	-433.
90.00	0.249	-451.	0.258	-429.
97.00	0.243	-449.	0.233	-415.

DATA POINT 5 – FIRST HARMONIC

AXIAL LOCATION PERCENT OF CHORD	SUCTION SURFACE AMPLITUDE	SUCTION SURFACE PHASE	PRESSURE SURFACE AMPLITUDE	PRESSURE SURFACE PHASE
2.94	1.754	-195.	6.446	-398.
10.00	0.829	-211.	0.936	-251.
20.00	0.293	-154.	0.762	-334.
30.00	0.460	-171.	0.085	-416.
40.00	0.356	-217.	0.280	-245.
50.00	0.291	-256.	0.263	-297.
60.00	0.358	-301.	0.158	-311.
70.00	0.323	-364.	0.146	-251.
80.00	0.158	-465.	0.224	-288.
90.00	0.293	-254.	0.118	-292.
97.00	0.402	-327.	0.052	-364.

DATA POINT 5 — SECOND HARMONIC

AXIAL LOCATION	SUCTION SURFACE		PRESSURE SURFACE	
PERCENT OF CHORD	AMPLITUDE	PHASE	AMPLITUDE	PHASE
2.94	0.815	-520.	2.689	-403.
10.00	0.241	-485.	0.776	-507.
20.00	0.239	-512.	0.152	-510.
30.00	0.051	-366.	0.282	-371.
40.00	0.250	-455.	0.052	-401.
50.00	0.110	-604.	0.155	-390.
60.00	0.312	-412.	0.103	-379.
70.00	0.062	-608.	0.110	-379.
80.00	0.201	-424.	0.108	-380.
90.00	0.091	-356.	0.097	-388.
97.00	0.194	-411.	0.077	-395.

DATA POINT 6 — FIRST HARMONIC

AXIAL LOCATION	SUCTION SURFACE		PRESSURE SURFACE	
PERCENT OF CHORD	AMPLITUDE	PHASE	AMPLITUDE	PHASE
2.94	1.603	-181.	2.423	-387.
10.00	0.481	-186.	0.866	-340.
20.00	0.328	-433.	0.796	-326.
30.00	0.207	-134.	0.621	-324.
40.00	0.120	-267.	0.352	-329.
50.00	0.266	-306.	0.378	-315.
60.00	0.776	-322.	0.535	-325.
70.00	0.667	-360.	0.247	-348.
80.00	0.229	-379.	0.210	-349.
90.00	0.559	-310.	0.176	-403.
97.00	0.959	-335.	0.261	-405.

DATA POINT 6 — SECOND HARMONIC

AXIAL LOCATION	SUCTION SURFACE		PRESSURE SURFACE	
PERCENT OF CHORD	AMPLITUDE	PHASE	AMPLITUDE	PHASE
2.94	0.853	-524.	0.616	-376.
10.00	0.166	-490.	0.345	-296.
20.00	0.224	-526.	0.124	-281.
30.00	0.145	-264.	0.120	-324.
40.00	0.121	-466.	0.067	-264.
50.00	0.224	-267.	0.106	-343.
60.00	0.187	-429.	0.074	-332.
70.00	0.101	-316.	0.079	-353.
80.00	0.167	-467.	0.098	-400.
90.00	0.157	-421.	0.100	-413.
97.00	0.220	-452.	0.095	-479.

DATA POINT 7 — FIRST HARMONIC

AXIAL LOCATION PERCENT OF CHORD	SUCTION SURFACE		PRESSURE SURFACE	
	AMPLITUDE	PHASE	AMPLITUDE	PHASE
2.94	0.951	-245.	1.946	-339.
10.00	0.372	-212.	1.293	-327.
20.00	0.198	-370.	1.173	-323.
30.00	0.105	-307.	0.756	-316.
40.00	0.384	-304.	0.736	-308.
50.00	0.685	-307.	0.709	-316.
60.00	0.983	-335.	0.673	-315.
70.00	0.562	-336.	0.489	-300.
80.00	0.702	-314.	0.455	-297.
90.00	0.851	-338.	0.237	-285.
97.00	0.899	-344.	0.133	-286.

DATA POINT 7 – SECOND HARMONIC

AXIAL LOCATION PERCENT OF CHORD	SUCTION SURFACE AMPLITUDE	SUCTION SURFACE PHASE	PRESSURE SURFACE AMPLITUDE	PRESSURE SURFACE PHASE
2.94	0.715	-450.	0.585	-307.
10.00	0.197	-474.	0.244	-296.
20.00	0.275	-499.	0.174	-279.
30.00	0.067	-246.	0.052	-288.
40.00	0.094	-495.	0.117	-291.
50.00	0.076	-294.	0.065	-289.
60.00	0.019	-258.	0.097	-310.
70.00	0.056	-382.	0.076	-308.
80.00	0.057	-433.	0.033	-369.
90.00	0.061	-429.	0.094	-331.
97.00	0.062	-410.	0.095	-337.

DATA POINT 8 – FIRST HARMONIC

AXIAL LOCATION PERCENT OF CHORD	SUCTION SURFACE		PRESSURE SURFACE	
	AMPLITUDE	PHASE	AMPLITUDE	PHASE
2.94	2.380	-196.	1.985	-350.
10.00	0.419	-359.	1.355	-344.
20.00	0.508	-426.	1.099	-343.
30.00	0.088	-399.	0.832	-341.
40.00	0.540	-339.	0.778	-340.
50.00	0.720	-356.	0.702	-344.
60.00	0.764	-360.	0.737	-342.
70.00	0.698	-350.	0.589	-342.
80.00	0.842	-357.	0.559	-345.
90.00	0.760	-357.	0.434	-342.
97.00	0.924	-353.	0.377	-344.

DATA POINT 8 — SECOND HARMONIC

AXIAL LOCATION	SUCTION SURFACE		PRESSURE SURFACE	
PERCENT OF CHORD	AMPLITUDE	PHASE	AMPLITUDE	PHASE
2.94	2.124	-528.	0.685	-317.
10.00	0.765	-434.	0.288	-309.
20.00	0.248	-213.	0.163	-302.
30.00	0.106	-497.	0.132	-304.
40.00	0.086	-297.	0.122	-307.
50.00	0.029	-244.	0.105	-315.
60.00	0.093	-365.	0.117	-326.
70.00	0.050	-340.	0.102	-335.
80.00	0.090	-414.	0.107	-357.
90.00	0.096	-407.	0.130	-351.
97.00	0.095	-414.	0.143	-354.

DATA POINT 9 – FIRST HARMONIC

AXIAL LOCATION	SUCTION SURFACE		PRESSURE SURFACE	
PERCENT OF CHORD	AMPLITUDE	PHASE	AMPLITUDE	PHASE
2.94	1.156	-175.	6.437	-386.
10.00	0.166	-194.	0.914	-216.
20.00	0.443	-435.	0.844	-340.
30.00	0.312	-120.	0.288	-407.
40.00	0.126	-228.	0.102	-306.
50.00	0.185	-315.	0.174	-336.
60.00	0.188	-330.	0.091	-399.
70.00	0.226	-401.	0.121	-339.
80.00	0.343	-138.	0.073	-344.
90.00	0.417	-189.	0.161	-343.
97.00	0.252	-195.	0.130	-352.

DATA POINT 9 — SECOND HARMONIC

AXIAL LOCATION PERCENT OF CHORD	SUCTION SURFACE AMPLITUDE	SUCTION SURFACE PHASE	PRESSURE SURFACE AMPLITUDE	PRESSURE SURFACE PHASE
2.94	0.722	-528.	2.181	-412.
10.00	0.155	-461.	0.898	-314.
20.00	0.152	-516.	0.021	-178.
30.00	0.108	-365.	0.210	-370.
40.00	0.179	-458.	0.079	-340.
50.00	0.093	-273.	0.051	-409.
60.00	0.158	-413.	0.019	-406.
70.00	0.073	-552.	0.030	-485.
80.00	0.113	-473.	0.050	-503.
90.00	0.058	-527.	0.080	-523.
97.00	0.141	-468.	0.096	-188.

DATA POINT 10 – FIRST HARMONIC

AXIAL LOCATION PERCENT OF CHORD	SUCTION SURFACE		PRESSURE SURFACE	
	AMPLITUDE	PHASE	AMPLITUDE	PHASE
2.94	0.893	-176.	1.951	-397.
10.00	0.075	-332.	0.580	-358.
20.00	0.513	-415.	0.549	-343.
30.00	0.248	-422.	0.489	-344.
40.00	0.165	-353.	0.372	-352.
50.00	0.299	-338.	0.312	-336.
60.00	0.426	-342.	0.363	-339.
70.00	0.306	-385.	0.269	-352.
80.00	0.195	-158.	0.132	-324.
90.00	0.261	-219.	0.285	-328.
97.00	0.132	-158.	0.157	-179.

DATA POINT 10 — SECOND HARMONIC

AXIAL LOCATION PERCENT OF CHORD	SUCTION SURFACE AMPLITUDE	SUCTION SURFACE PHASE	PRESSURE SURFACE AMPLITUDE	PRESSURE SURFACE PHASE
2.94	0.816	-525.	0.457	-362.
10.00	0.251	-494.	0.387	-332.
20.00	0.249	-505.	0.308	-356.
30.00	0.098	-386.	0.311	-373.
40.00	0.285	-433.	0.239	-363.
50.00	0.151	-372.	0.278	-363.
60.00	0.300	-412.	0.192	-361.
70.00	0.121	-386.	0.180	-362.
80.00	0.169	-450.	0.083	-368.
90.00	0.128	-451.	0.049	-346.
97.00	0.232	-478.	0.016	-214.

DATA POINT 11 – FIRST HARMONIC

AXIAL LOCATION PERCENT OF CHORD	SUCTION SURFACE AMPLITUDE	SUCTION SURFACE PHASE	PRESSURE SURFACE AMPLITUDE	PRESSURE SURFACE PHASE
2.94	0.526	-164.	1.122	-368.
10.00	0.080	-93.	0.760	-351.
20.00	0.482	-73.	0.649	-364.
30.00	0.296	-74.	0.415	-354.
40.00	0.191	-365.	0.468	-347.
50.00	0.394	-356.	0.378	-356.
60.00	0.393	-381.	0.341	-347.
70.00	0.150	-377.	0.336	-347.
80.00	0.172	-364.	0.250	-362.
90.00	0.107	-81.	0.258	-341.
97.00	0.177	-131.	0.184	-328.

DATA POINT 11 – SECOND HARMONIC

AXIAL LOCATION	SUCTION SURFACE		PRESSURE SURFACE	
PERCENT OF CHORD	AMPLITUDE	PHASE	AMPLITUDE	PHASE
2.94	0.787	-161.	0.641	-345.
10.00	0.261	-161.	0.412	-351.
20.00	0.242	-161.	0.302	-357.
30.00	0.093	-423.	0.302	-366.
40.00	0.170	-436.	0.307	-371.
50.00	0.256	-413.	0.330	-380.
60.00	0.267	-414.	0.302	-379.
70.00	0.217	-418.	0.256	-382.
80.00	0.215	-422.	0.200	-387.
90.00	0.115	-440.	0.153	-392.
97.00	0.147	-457.	0.131	-399.

DATA POINT 12 — FIRST HARMONIC

AXIAL LOCATION PERCENT OF CHORD	SUCTION SURFACE AMPLITUDE	SUCTION SURFACE PHASE	PRESSURE SURFACE AMPLITUDE	PRESSURE SURFACE PHASE
2.94	2.654	-189.	1.041	-356.
10.00	0.321	-379.	0.800	-345.
20.00	0.418	-80.	0.571	-351.
30.00	0.158	-399.	0.444	-336.
40.00	0.270	-347.	0.449	-337.
50.00	0.374	-348.	0.358	-335.
60.00	0.302	-356.	0.337	-331.
70.00	0.173	-346.	0.312	-333.
80.00	0.152	-354.	0.228	-336.
90.00	0.070	-47.	0.256	-334.
97.00	0.099	-102.	0.173	-330.

DATA POINT 12 — SECOND HARMONIC

AXIAL LOCATION PERCENT OF CHORD	SUCTION SURFACE AMPLITUDE	SUCTION SURFACE PHASE	PRESSURE SURFACE AMPLITUDE	PRESSURE SURFACE PHASE
2.94	1.416	-207.	0.611	-344.
10.00	0.505	-149.	0.394	-352.
20.00	0.163	-149.	0.302	-354.
30.00	0.088	-100.	0.289	-364.
40.00	0.172	-427.	0.292	-368.
50.00	0.231	-409.	0.288	-376.
60.00	0.264	-411.	0.286	-377.
70.00	0.253	-413.	0.246	-384.
80.00	0.224	-423.	0.202	-392.
90.00	0.137	-426.	0.183	-385.
97.00	0.105	-444.	0.083	-418.

DATA POINT 13 – FIRST HARMONIC

AXIAL LOCATION	SUCTION SURFACE		PRESSURE SURFACE	
PERCENT OF CHORD	AMPLITUDE	PHASE	AMPLITUDE	PHASE
2.94	1.542	-179.	6.767	-370.
10.00	0.677	-196.	1.241	-244.
20.00	0.162	-132.	1.232	-313.
30.00	0.301	-158.	0.397	-326.
40.00	0.294	-250.	0.394	-280.
50.00	0.366	-290.	0.476	-299.
60.00	0.579	-301.	0.385	-309.
70.00	0.607	-333.	0.308	-287.
80.00	0.179	-361.	0.352	-300.
90.00	0.476	-272.	0.238	-310.
97.00	0.821	-307.	0.220	-334.

DATA POINT 13 – SECOND HARMONIC

AXIAL LOCATION	SUCTION SURFACE		PRESSURE SURFACE	
PERCENT OF CHORD	AMPLITUDE	PHASE	AMPLITUDE	PHASE
2.94	0.808	-515.	2.119	-397.
10.00	0.173	-501.	0.738	-281.
20.00	0.229	-516.	0.199	-516.
30.00	0.070	-281.	0.133	-342.
40.00	0.161	-466.	0.055	-211.
50.00	0.200	-236.	0.025	-377.
60.00	0.227	-407.	0.019	-325.
70.00	0.113	-238.	0.019	-387.
80.00	0.150	-439.	0.027	-349.
90.00	0.096	-328.	0.017	-387.
97.00	0.179	-411.	0.019	-382.

DATA POINT 14 — FIRST HARMONIC

AXIAL LOCATION PERCENT OF CHORD	SUCTION SURFACE		PRESSURE SURFACE	
	AMPLITUDE	PHASE	AMPLITUDE	PHASE
2.94	1.452	-191.	1.892	-363.
10.00	0.500	-201.	1.084	-316.
20.00	0.086	-392.	1.105	-308.
30.00	0.128	-206.	0.867	-313.
40.00	0.306	-303.	0.586	-310.
50.00	0.444	-312.	0.659	-294.
60.00	0.969	-324.	0.745	-309.
70.00	0.808	-352.	0.423	-305.
80.00	0.376	-305.	0.395	-309.
90.00	0.952	-310.	0.276	-293.
97.00	1.156	-332.	0.175	-330.

DATA POINT 14 — SECOND HARMONIC

AXIAL LOCATION	SUCTION SURFACE		PRESSURE SURFACE	
PERCENT OF CHORD	AMPLITUDE	PHASE	AMPLITUDE	PHASE
2.94	0.758	-376.	0.324	-214.
10.00	0.144	-347.	0.321	-142.
20.00	0.193	-379.	0.106	-131.
30.00	0.135	-143.	0.165	-153.
40.00	0.112	-303.	0.096	-125.
50.00	0.230	-137.	0.066	-133.
60.00	0.155	-281.	0.091	-134.
70.00	0.173	-177.	0.075	-147.
80.00	0.057	-327.	0.062	-157.
90.00	0.159	-247.	0.060	-157.
97.00	0.131	-310.	0.061	-168.

DATA POINT 15 – FIRST HARMONIC

AXIAL LOCATION PERCENT OF CHORD	SUCTION SURFACE AMPLITUDE	SUCTION SURFACE PHASE	PRESSURE SURFACE AMPLITUDE	PRESSURE SURFACE PHASE
2.94	1.096	-240.	1.522	-347.
10.00	0.510	-236.	1.197	-331.
20.00	0.085	-335.	0.981	-333.
30.00	0.086	-241.	0.665	-325.
40.00	0.394	-301.	0.657	-321.
50.00	0.641	-322.	0.579	-323.
60.00	0.711	-340.	0.610	-315.
70.00	0.489	-328.	0.449	-313.
80.00	0.688	-331.	0.408	-315.
90.00	0.564	-351.	0.171	-317.
97.00	0.657	-344.	0.123	-315.

DATA POINT 15 – SECOND HARMONIC

AXIAL LOCATION	SUCTION SURFACE		PRESSURE SURFACE	
PERCENT OF CHORD	AMPLITUDE	PHASE	AMPLITUDE	PHASE
2.94	0.546	-520.	0.538	-354.
10.00	0.172	-528.	0.237	-355.
20.00	0.205	-186.	0.138	-342.
30.00	0.027	-316.	0.085	-343.
40.00	0.044	-199.	0.086	-346.
50.00	0.041	-368.	0.070	-348.
60.00	0.045	-349.	0.069	-344.
70.00	0.016	-465.	0.045	-379.
80.00	0.031	-439.	0.038	-394.
90.00	0.022	-458.	0.069	-406.
97.00	0.031	-484.	0.065	-397.

DATA POINT 16 – FIRST HARMONIC

AXIAL LOCATION	SUCTION SURFACE		PRESSURE SURFACE	
PERCENT OF CHORD	AMPLITUDE	PHASE	AMPLITUDE	PHASE
2.94	2.756	-213.	1.246	-326.
10.00	0.515	-265.	1.025	-314.
20.00	0.341	-224.	0.823	-306.
30.00	0.473	-255.	0.697	-296.
40.00	0.597	-282.	0.617	-293.
50.00	0.574	-301.	0.557	-295.
60.00	0.634	-307.	0.586	-294.
70.00	0.515	-307.	0.436	-290.
80.00	0.556	-312.	0.379	-294.
90.00	0.505	-322.	0.258	-283.
97.00	0.567	-325.	0.221	-291.

DATA POINT 16 – SECOND HARMONIC

AXIAL LOCATION PERCENT OF CHORD	SUCTION SURFACE AMPLITUDE	SUCTION SURFACE PHASE	PRESSURE SURFACE AMPLITUDE	PRESSURE SURFACE PHASE
2.94	1.374	-220.	0.397	-368.
10.00	0.500	-161.	0.161	-366.
20.00	0.127	-187.	0.061	-363.
30.00	0.077	-206.	0.055	-351.
40.00	0.078	-181.	0.026	-368.
50.00	0.040	-310.	0.057	-342.
60.00	0.023	-172.	0.040	-370.
70.00	0.014	-393.	0.046	-367.
80.00	0.010	-472.	0.037	-379.
90.00	0.010	-466.	0.071	-377.
97.00	0.033	-181.	0.068	-385.

$EOJ 10:55:44